Univerza v Ljubljani
Institut "Jožef Stefan", Ljubljana

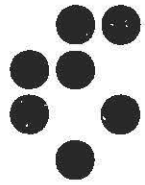

IJS DP - 6928
februar 1994

Production of $\omega\rho^0$, $\rho^0\phi$ and $\omega\phi$ in Two-Photon Interactions at the ARGUS Spectrometer

Ervin Križnič

JAMOVA 39 · 61111 LJUBLJANA, SLOVENIJA

UNIVERZA V LJUBLJANI
FAKULTETA ZA NARAVOSLOVJE IN TEHNOLOGIJO
ODDELEK ZA FIZIKO

Doctor thesis

Production of $\omega\rho^0$, $\rho^0\phi$ and $\omega\phi$ in Two-Photon Interactions at the ARGUS Spectrometer

Ervin Križnič

Ljubljana, 1993

UNIVERZA V LJUBLJANI
FAKULTETA ZA NARAVOSLOVJE IN TEHNOLOGIJO
ODDELEK ZA FIZIKO

Disertacija

Tvorba $\omega\rho^0$, $\rho^0\phi$ in $\omega\phi$ pri dvofotonskih interakcijah s spektrometrom ARGUS

Ervin Križnič

Ljubljana, 1993

Opisano delo je bilo narejeno v okviru raziskovalnega programa Odseka za eksperimentalno fiziko osnovnih delcev Instituta "Jožef Stefan" in Univerze v Ljubljani. Nalogo je financiralo Ministrstvo za znanost in tehnologijo, ki sem mu še posebej hvaležen, saj mi je s podelitvijo štipendije omogočilo delo v mednarodnem institutu DESY v Hamburgu. Meritve smo opravili s spektrometrom ARGUS na shranjevalnem obroču DORIS.

Mentorju prof. dr. Gabrijelu Kernelu se za njegov trud in zavzetost pri nastajanju tega dela najlepše zahvaljujem. Zahvaljujem se tudi doc. dr. Petru Križanu za številne nasvete in pozoren pregled rokopisa. Posebna zahvala gre vsem članom skupine ARGUS posebej še sodelavcem B. Boštjančiču, M. Plešku, T. Podobniku in T. Živku ter vsem sodelavcem iz odseka za eksperimentalno fiziko osnovnih delcev.

Izvleček

Tvorbo petih pionov pri dvofotonskih interakcijah smo proučevali na podatkih, zbranih s spektrometrom ARGUS. Z metodo maksimalne zanesljivosti smo določili prispevke reakcij $\gamma\gamma \to \omega\rho^0$, $\gamma\gamma \to \omega\pi^+\pi^-$, $\gamma\gamma \to \rho^0\pi^+\pi^0\pi^-$ in $\gamma\gamma \to \pi^+\pi^+\pi^0\pi^-\pi^-$. Posebej pomemben je presek za dvofotonsko produkcijo para vektorskih mezonov $\omega\rho^0$, ki smo ga izmerili z manjšo napako kot drugi eksperimenti. Določili smo tudi prispevke valov z različnim spinom ter parnostjo k reakciji $\gamma\gamma \to \omega\rho^0$. Analiza kotnih porazdelitev kaže na dominanco prispevka stanja s spinom in parnostjo $(J^P, J_z) = (2^+, 2)$ na območju dvofotonske invariantne mase med 1.5 in 2.3 GeV. Razen tvorbe parov vektorskih mezonov $\omega\rho^0$ smo študirali tudi reakciji $\gamma\gamma \to \rho^0\phi \to \pi^+\pi^-K^+K^-$ in $\gamma\gamma \to \omega\phi \to \pi^+\pi^0\pi^-K^+K^-$. Prvi smo določili presek za tvorbo parov $\rho^0\phi$ pri dvofotonskih interakcijah. Presek za to reakcijo je največji na intervalu dvofotonske energije med 1.5 in 2.5 GeV. Izmerili smo tudi štiri dogodke, ki kažejo na obstoj reakcije $\gamma\gamma \to \omega\phi$.

Abstract

The production of five pions in two-photon interactions was studied with the ARGUS detector. By using the maximum likelihood method the contributions of reactions $\gamma\gamma \to \omega\rho^0$, $\gamma\gamma \to \omega\pi^+\pi^-$, $\gamma\gamma \to \rho^0\pi^+\pi^0\pi^-$, and $\gamma\gamma \to \pi^+\pi^+\pi^0\pi^-\pi^-$ were determined. Of particular interest is the cross section for $\gamma\gamma \to \omega\rho^0$ which is measured with better precision than in previous measurements. The spin-parity composition of the $\omega\rho^0$ system was determined using the partial-wave analysis. A dominance of the wave $(J^P, J_z) = (2^+, 2)$ is found in the region of center-of-mass energies between 1.5 and 2.3 GeV. Beside $\omega\rho^0$ production also $\rho^0\phi$ and $\omega\phi$ channels were studied. The process $\gamma\gamma \to \rho^0\phi$ was observed for the first time. Its cross section is highest in the region of center-of-mass energies between 1.5 and 2.5 GeV. We also found an evidence for the reaction $\gamma\gamma \to \omega\phi$.

Contents

Introduction

Two-photon physics is a relatively new branch of experimental particle physics, closely related to high energy e^+e^- storage rings. Bunches of electrons and positrons surrounded by clouds of virtual photons circulate in a storage ring in the opposite directions. Interactions between photons of different clouds offer an opportunity to study two-photon reactions in a wide kinematical region. Two-photon interactions with leptons in the final state provide a test of quantum electro-dynamics up to the fourth order of fine structure constant α. But the interest has lately turned to reactions with hadrons in the final state.

Particularly interesting is the two-photon production of vector meson pairs, which enables a study of meson scattering on mesons. Due to equal quantum numbers, virtual photons can convert into neutral vector mesons which then mutually hadronically interact. Experimental studies of the gamma-gamma production of two vector mesons have revealed an interesting structure. It was found that the cross section for $\gamma\gamma \to \rho^0\rho^0$ exhibits a peak near the reaction threshold. The reaction was first measured by the TASSO collaboration [1] at PETRA storage ring in Hamburg. Later, it was found by JADE collaboration that the cross section for the production of an isospin related pair $\gamma\gamma \to \rho^+\rho^-$ is more than four times smaller. This ratio cannot be explained by production of a pure isospin state. Since two ρ^0 mesons can only combine to isospin I=0 or I=2, the ratio for production of isospin pure state can only assume the values 1/2 or 2, respectively. If these predictions are compared to the experimental results, it is clear that we are dealing with a coherent mixture of both I=0 and I=2 states. Measurement of a resonant origin of the reaction $\gamma\gamma \to \rho\rho$ would probably confirm an existence of exotic $qq\overline{qq}$ states, since bound states of pairs quark anti-quark cannot have an isospin 2. The origin of the reaction $\gamma\gamma \to \rho\rho$ can be found by partial wave analysis, which requires a large data sample. With the high statistics collected by the ARGUS detector, the analysis of $\gamma\gamma \to \rho^0\rho^0$ showed a clear dominance of the $(J^P, J_z) = (2^+, 2)$ wave [2], hinting the formation of a resonance. It is believed that analysis of other vector meson pairs may contribute to better understanding of $\rho\rho$ production.

Resonant four-quark structures are expected [3] also in production of vector mesons

$\omega\rho$ and $\rho\phi$. The cross section for $\omega\rho^0$ production has already been measured by several groups, first by ARGUS collaboration in 1987[4]. An enhanced cross section was found at 1.9 GeV. Near threshold, where resonant structure is expected by the four quark model [3], no enhancement has been observed. For better understanding of the reaction $\gamma\gamma \to \omega\rho^0$, it is important to make a partial wave analysis. Due to lack of experimental data, the partial wave decomposition of this reaction has not been performed. In this thesis we present the results of a partial wave analysis of the reaction $\gamma\gamma \to \omega\rho^0 \to \pi^+\pi^+\pi^0\pi^-\pi^-$ using the data sample collected by the ARGUS detector. The detector provides a good particle identification, precise measurement of their momenta and consequently a low contribution of the background reactions. This turns out to be very important, particularly because no cut on two and three-pion invariant masses can be used. In addition, many waves can contribute to the studied reaction even further intensifying difficulties. Particularly high statistics is needed in the case none of the waves dominates. This thesis includes also the study of reactions $\gamma\gamma \to \rho^0\phi$ and $\gamma\gamma \to \omega\phi$. The production rate for both reactions is small, and this is the first time that they were detected. Previously, only the upper limits for the cross sections were set by collaborations TPC/Two-Gamma, TASSO and ARGUS [5, 6].

The thesis is organized as follows. In the first chapter a brief review of the kinematics for the two-photon interactions is given. It includes also all the relevant formulas describing general features of all three studied reactions: $\gamma\gamma \to \omega\rho^0$, $\gamma\gamma \to \rho^0\phi$, and $\gamma\gamma \to \omega\phi$. The third chapter describes the detector with an emphasis on the drift chambers and the calorimeter, i.e. components that are extensively used in the analysis. This is followed by a description of the trigger system and methods of charged particle identification. The Monte Carlo simulation of the physical processes and particle tracking through the detector is described in chapter 3. Using the simulation we determine the experimental resolution of all quantities needed in partial-wave analysis. In chapter 4 we present a selection of the five pion final state and estimate the background contribution to the selected 5π events used in $\gamma\gamma \to \omega\rho^0$ analysis. A brief description of the maximum likelihood method and the acceptance calculation is given in chapter 5. The final results and determination of systematic errors can be found in chapter 6. Chapters 7 and 8 describe the analysis of reactions $\gamma\gamma \to \rho^0\phi \to \pi^+\pi^-K^+K^-$ and $\gamma\gamma \to \omega\phi \to \pi^+\pi^0\pi^-K^+K^-$. They are organized in a similar way as the presentation of the $\gamma\gamma \to \omega\rho^0 \to \pi^+\pi^+\pi^0\pi^-\pi^-$ analysis. A short summary of the results can be found in the last chapter. In entire work we use the convention $c = 1$ and $\hbar = 1$.

Chapter 1

The Physics of Two-Photon Interactions

1.1 General Discussion

In a two-photon process at an e^+e^- collider electron and positron interact by radiating space-like virtual photons that in turn produce a final state X. The kinematic variables of a two-photon reaction $e^+e^- \rightarrow e^+e^-X$ are shown in fig. 1.1 where all particles are

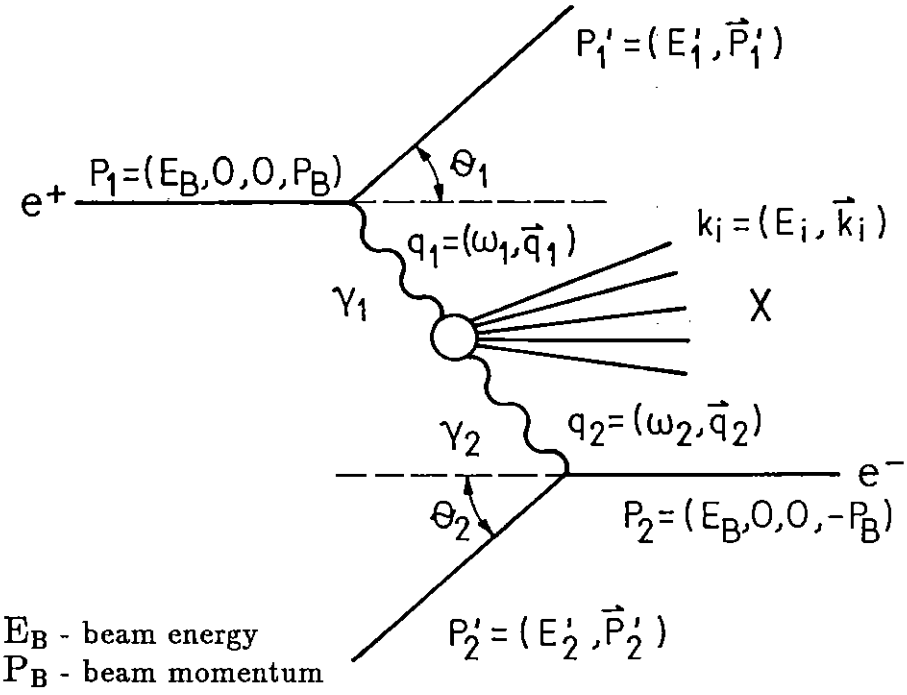

Figure 1.1: Kinematics of the two-photon process

described by four-vectors: incoming leptons by p_i, scattered ones by p_i' and photons by

$q_i = p_i - p_i'$. The z-axis in the laboratory frame points in direction of the incident positron. The x-axis has an arbitrary direction perpendicular to the beam line.

The transition matrix element for the process consists of electron and positron vertices represented by $i(\pm e)\gamma_\mu$, two photon propagators $-ig^{\mu\nu}/q_i^2$ and the matrix element $T_{\alpha\beta}$ describing the formation of the final state X by two photons. The amplitude can be written as [7]:

$$M = -e^2 \cdot \{\bar{u}(p_1', s_1')\gamma_\mu u(p_1, s_1)\}\frac{g^{\mu\alpha}}{q_1^2}T_{\alpha\beta}\frac{g^{\beta\nu}}{q_2^2}\{\bar{v}(p_2, s_2)\gamma_\nu v(p_2', s_2')\} \tag{1.1}$$

where by $u(p_i, s_i)$ and $v(p_i, s_i)$ we denote the spinor of leptons with four-momenta p_i and spin s_i. By introducing an unnormalized photon density flux matrix

$$\rho_i^{\mu\nu} \equiv -\frac{1}{q_i^2}\sum_{spins}\bar{u}(p_i', s_i')\gamma^\mu u(p_i, s_i)\bar{u}(p_i, s_i)\gamma^\nu u(p_i', s_i') \tag{1.2}$$

the expression for the cross section can be written as:

$$d\sigma = \frac{(4\pi\alpha)^2}{q_1^2 q_2^2}\rho_1^{\mu\mu'}\rho_2^{\nu\nu'}T^*_{\mu'\nu'}T_{\mu\nu}\frac{dLips}{4\{(p_1p_2)^2 - m_1^2m_2^2\}^{1/2}}\cdot\frac{d^3p_1'}{2E_1'(2\pi)^3}\cdot\frac{d^3p_2'}{2E_2'(2\pi)^3} \tag{1.3}$$

where $dLips$ is the Lorentz invariant phase space of the final state X

$$dLips = (2\pi)^4\ \delta^4(q_1 + q_2 - \sum_i k_i)\ \prod_i \frac{d^3k_i}{2E_i(2\pi)^3}. \tag{1.4}$$

Due to gauge invariance only three of the four Lorentz indices are independent. It is suitable to express the unnormalized photon density flux matrix $\rho_i^{\mu\nu}$ and the matrix element $T_{\alpha\beta}$ in the helicity basis of photons. The transformations of the quantities $T_{\mu\nu}$, $\rho_1^{\mu\mu'}$ and $\rho_2^{\nu\nu'}$ are of the following form:

$$T_{ab} = \varepsilon_{1a}^\mu\varepsilon_{2b}^\nu T_{\mu\nu}\ , \quad \rho_1^{aa'} = \varepsilon_{1a}^\mu\varepsilon_{1a'}^{\mu'}\rho_1^{\mu\mu'}\ , \quad \rho_2^{bb'} = \varepsilon_{2b}^\nu\varepsilon_{2b'}^{\nu'}\rho_2^{\nu\nu'}\ . \tag{1.5}$$

The indices a, b take the values $+, -$ and 0 corresponding to the photon polarization vectors ε_{i+}, ε_{i-} and ε_{i0}. Transversely polarized photons (T) have helicity $+1$ or -1, and longitudinally polarized photons (L) helicity 0. For later convenience we introduce the abbreviation

$$\mathcal{Z}^{aba'b'} = \rho_1^{aa'}\rho_2^{bb'}T^*_{a'b'}T_{ab}, \tag{1.6}$$

with no summation over double indices. The $\mathcal{Z}$ matrix is symmetrical against the substitution $ab \leftrightarrow a'b'$ due to time invariance. In the following we shall consider only the case where none of both scattered leptons is detected, the so called "no-tag" mode. In this case the azimuthal angle φ_i between lepton scattering planes and the x-axis in the

laboratory frame cannot be measured, so an implicit integration over both angles φ_1, φ_2 can be performed. One can see from the photon density matrix [7]

$$\rho_i^{aa'} = \begin{pmatrix} \rho_i^{++} & -i|\rho_i^{+0}|e^{i\varphi_i} & -|\rho_i^{+-}|e^{2i\varphi_i} \\ i|\rho_i^{+0}|e^{-i\varphi_i} & \rho_i^{00} & -i|\rho_i^{+0}|e^{i\varphi_i} \\ -|\rho_i^{+-}|e^{-2i\varphi_i} & i|\rho_i^{+0}|e^{-i\varphi_i} & \rho_i^{++} \end{pmatrix} \tag{1.7}$$

with

$$\begin{aligned} \rho_1^{++} &= \frac{1}{2}\left(\frac{(2p_1q_2 - q_1q_2)^2}{(q_1q_2)^2 - q_1^2q_2^2} + 1 + \frac{4m_e^2}{q_1^2}\right) \\ \rho_1^{00} &= \frac{(2p_1q_2 - q_1q_2)^2}{(q_1q_2)^2 - q_1^2q_2^2} - 1 \\ |\rho_1^{+-}| &= \rho_1^{++} - 1 \\ |\rho_1^{+0}| &= \sqrt{(\rho_1^{00} + 1)|\rho_1^{+-}|} \\ |\rho_2^{ab}| &= |\rho_1^{ab}(1 \leftrightarrow 2)| \end{aligned}$$

that only diagonal elements of this matrix do not vanish after integration over the azimuthal angle φ_i. It is useful to factorize the matrix element T_{ab}, in order to separate the two photon formation of intermediate state from its decay

$$T_{ab} \equiv M_{ab}(\gamma\gamma \to R) \cdot \delta_{a-b}^{J_z}\delta_{J_R}^{J_X} \cdot P_R \cdot D_{J_z}(R \to X) \; . \tag{1.8}$$

The M_{ab} is in this definition the helicity amplitude for the two photon coupling to the intermediate state R, and D_{J_z} is describing the decay of that state into the final state X. J_z stands for the spin projection of the state R on the helicity axis in the $\gamma\gamma$ center-of-mass system. The δ functions in the expression ensure angular momentum conservation. For a resonance formation the propagator P_R of the intermediate state R is of the Breit-Wigner form

$$P_R = \frac{1}{m_R^2 - W^2 - im_R\Gamma_R}, \tag{1.9}$$

while for continuum reactions it is expected to vary weakly with two-photon invariant mass. Now we can collect all $\mathcal{Z}$ matrix elements that do not vanish in no-tag condition. They are listed in table 1.1. Inserting only terms listed in table 1.1 into eq. 1.3 one can obtain Budnev formula [7], the basic equation for $\gamma\gamma$ physics,

$$\begin{aligned} d\sigma &= \frac{\alpha^2}{16\pi^4 q_1^2 q_2^2} \cdot \left[\frac{(q_1q_2)^2 - q_1^2q_2^2}{(p_1p_2)^2 - m_1^2m_2^2}\right]^{1/2} \cdot \\ &\left[4\rho_1^{++}\rho_2^{++}\sigma_{TT} + 2\rho_1^{++}\rho_2^{00}\sigma_{TL} + 2\rho_1^{00}\rho_2^{++}\sigma_{LT} + \rho_1^{00}\rho_2^{00}\sigma_{LL}\right]\frac{d^3p_1'}{E_1'} \cdot \frac{d^3p_2'}{E_2'} \end{aligned} \tag{1.10}$$

helicity	$ab, a'b'$	$\mathcal{Z}^{ab,a'b'}$
0	$++,++$	$\rho_1^{++}\rho_2^{++}M_{++}^*M_{++}P_R^*P_RD_0^*D_0$
0	$--,--$	$\rho_1^{++}\rho_2^{++}M_{--}^*M_{--}P_R^*P_RD_0^*D_0$
$+2$	$+-,+-$	$\rho_1^{++}\rho_2^{++}M_{+-}^*M_{+-}P_R^*P_RD_{+2}^*D_{+2}$
-2	$-+,-+$	$\rho_1^{++}\rho_2^{++}M_{-+}^*M_{-+}P_R^*P_RD_{-2}^*D_{-2}$
$+1$	$0-,0-$	$\rho_1^{00}\rho_2^{++}M_{0-}^*M_{0-}P_R^*P_RD_{+1}^*D_{+1}$
-1	$0+,0+$	$\rho_1^{00}\rho_2^{++}M_{0+}^*M_{0+}P_R^*P_RD_{-1}^*D_{-1}$
-1	$-0,-0$	$\rho_1^{++}\rho_2^{00}M_{-0}^*M_{-0}P_R^*P_RD_{-1}^*D_{-1}$
$+1$	$+0,+0$	$\rho_1^{++}\rho_2^{00}M_{+0}^*M_{+0}P_R^*P_RD_{+1}^*D_{+1}$
0	$00,00$	$\rho_1^{00}\rho_2^{00}M_{00}^*M_{00}P_R^*P_RD_0^*D_0$

Table 1.1: Nonzero terms in the differential cross section formula for no-tag two-photon interactions

without a further symmetry requirement. In the formula 1.10 all interference terms that cannot be measured in no-tag mode are omitted. To obtain eq. 1.10 from eq. 1.3 we have used the following expressions of cross sections [7]:

$$\begin{aligned}
\sigma_{TT} &= \frac{1}{8\sqrt{x}}\int(T_{++}^*T_{++}+T_{+-}^*T_{+-})dLips(X)\\
\sigma_{TL} &= \frac{1}{4\sqrt{x}}\int T_{+0}^*T_{+0}dLips(X)\\
\sigma_{LT} &= \frac{1}{4\sqrt{x}}\int T_{0+}^*T_{0+}dLips(X)\\
\sigma_{LL} &= \frac{1}{4\sqrt{x}}\int T_{00}^*T_{00}dLips(X)
\end{aligned}$$

where x is the Møller flux factor $x=(q_1q_2)^2-q_1^2q_2^2$. Due to parity conservation in the two-photon vertex

$$M_{-a-b}^*M_{-a-b}=M_{ab}^*M_{ab} \tag{1.11}$$

and the inability to distinguish two states with different sign of helicity by their decay in the integral form, we combine terms T_{ab} obtained by substitution $+\leftrightarrow-$ to the same cross section.

From eq. 1.10 we can define the luminosity function as a function that connects the cross section $\sigma_{e^+e^-\to e^+e^-X}$ with the two-photon cross section $\sigma_{\gamma_T\gamma_T\to X}$ where both photons are transversely polarized

$$dL=\frac{\alpha^2}{16\pi^4q_1^2q_2^2}\cdot\left[\frac{(q_1q_2)^2-q_1^2q_2^2}{(p_1p_2)^2-m_1^2m_2^2}\right]^{1/2}4\rho_1^{++}\rho_2^{++}\frac{d^3p_1'}{E_1'}\cdot\frac{d^3p_2'}{E_2'} \tag{1.12}$$

Eq. 1.3 takes for the no-tag mode the following form:

$$d\sigma_{e^+e^-\to e^+e^-X} = \frac{dL}{16\sqrt{x}\rho_1^{++}\rho_2^{++}} \sum \mathcal{Z}^{ab,a'b'} dLips(X) \tag{1.13}$$

where only the elements listed in table 1.1 are included in the sum $\sum \mathcal{Z}^{ab,a'b'}$.

The two-photon vertex, in general described with helicity amplitudes M_{ab}, is subject to several constraints [8, 9] imposed by charge conjugation invariance, gauge and Lorentz invariance, Bose statistics and conservation of parity and angular momentum. The conservation of charge conjugation implies that in a two-photon process, only states of positive charge conjugation can be produced. We have already reduced the number of independent matrix elements $T_{\alpha\beta}$ by invoking the gauge invariance, but there is another feature of helicity amplitudes that can be concluded from gauge invariance. It turns out that for all spin-parity J^P states the following relation is valid [10]:

$$M_{0,b}(q_1^2, q_2^2) \sim \sqrt{-q_1^2} \quad (as \quad q_1^2 \to 0) \tag{1.14}$$

$$M_{a,0}(q_1^2, q_2^2) \sim \sqrt{-q_2^2} \quad (as \quad q_2^2 \to 0) \tag{1.15}$$

Therefore, it is convenient to expand the amplitudes M_{ab} in terms of covariant gauge invariant tensors written in the helicity basis. The simplest functional forms of gauge invariant tensors, describing the coupling of a two-photon system to a state with well defined spin and parity J^P are called Born amplitudes. Depending on the value of J^P, up to five independent form factors (F_{TT0}, F_{TT2}, F_{LL}, F_{TL}, F'_{TL}), generally marked with F_{abJ_z}, are needed in addition to Born amplitudes to describe the two-photon formation of intermediate state M_{ab}. The explicit forms of the amplitudes M_{ab}/F_{abJ_z} for the lowest spin states are given in table 1.2. The form factors are functions of q_i^2 of both photons and the invariant mass of the two-photon system. Due to Bose symmetry the form factors are required to be symmetrical in q_1^2 and q_2^2. Since the q_i^2 dependence of helicity amplitudes M_{ab} as $q_i^2 \to 0$ is already described with Born amplitudes, form factors are expected to be constant as $q_i^2 \to 0$.

It turns out to be convenient to write the form factors F_{abJ_z} as a product of two terms

$$F_{abJ_z}(-q_1^2, -q_2^2) = F_{abJ_z}(0,0) \cdot f(-q_1^2, -q_2^2) \ , \tag{1.16}$$

where $f(-q_1^2, -q_2^2)$ describes the $-q_i^2$ dependence and $F_{abJ_z}(0,0)$ the form factor value for point like particles. Clearly, $f(-q_1^2, -q_2^2)$ is normalized to 1 as $-q_1^2$ and $-q_2^2$ go to zero. Since form factors are not known from first principles, models are applied to describe $-q_i^2$ dependence. In the vector meson dominance model (VMD) [11] photons are assumed to convert into virtual vector-mesons before they interact with each other. Therefore, form

helicity J^P	0 M_{++}/F_{TT0}	0 M_{00}/F_{LL}	+1 $M_{0-}/(F_{TL}-(q_2^2-q_1^2)F'_{TL})$	+2 M_{+-}/F_{TT2}
$J^P = J^{+(-1)^J}$				
0^+	1	$\frac{\sqrt{q_1^2 q_2^2}}{q_1 q_2}$	0	0
1^-	$2(q_2^2-q_1^2)\frac{\sqrt{x}}{W}$	$2(q_2^2-q_1^2)\frac{\sqrt{q_1^2 q_2^2}}{q_1 q_2}\frac{\sqrt{x}}{W}$	$\frac{\sqrt{-q_1^2}}{q_1 q_2}$	0
2^+	$\frac{8}{\sqrt{6}}\frac{x}{W^2}$	$\frac{8}{\sqrt{6}}\frac{\sqrt{q_1^2 q_2^2}}{q_1 q_2}\frac{x}{W^2}$	$-\sqrt{2}\frac{\sqrt{-q_1^2}}{q_1 q_2}\frac{x}{W}$	1
$J^P = J^{-(-1)^J}$				
0^-	$\sqrt{x}$	0	0	0
1^+	$-\frac{q_2^2-q_1^2}{W}$	0	$\frac{\sqrt{-q_1^2}}{q_1 q_2}\sqrt{x}$	0
2^-	$-\frac{4}{\sqrt{6}}\sqrt{x}$	0	$-\sqrt{2}\frac{\sqrt{-q_1^2}}{q_1 q_2}\frac{\sqrt{x}}{W}$	$2(q_2^2-q_1^2)\sqrt{x}$

Table 1.2: Helicity amplitudes for the two photon coupling to the state with J^P spin and parity.

factors f are approximated with product of two single photon form factors. A decrease of the single photon form factor with increasing $|-q_i^2|$, is described with a pole curve

$$f(-q_1^2,-q_2^2) = \frac{1}{(1-q_1^2/m_V^2)\,(1-q_2^2/m_V^2)}\ , \tag{1.17}$$

where the pole mass is equal to the mass of a vector meson m_V. Usually ρ meson pole is used ($m_V = m_\rho$). For description of the form factor q_i^2 dependence also the prediction of a leading order QCD calculation [12] or a finite size model [13] are frequently used.

We would like to study two-photon reactions where both photons are almost real. The helicity amplitudes M_{ab} with one or both photons longitudinaly polarized are in this case negligible compared to amplitudes of transversely polarized photons. To ensure low q_i^2 for both photons it is necessary to require small transverse momentum of the two-photon system as it is shown in fig. 1.2. The typical value for two-photon transverse momenta cut is 100 MeV.

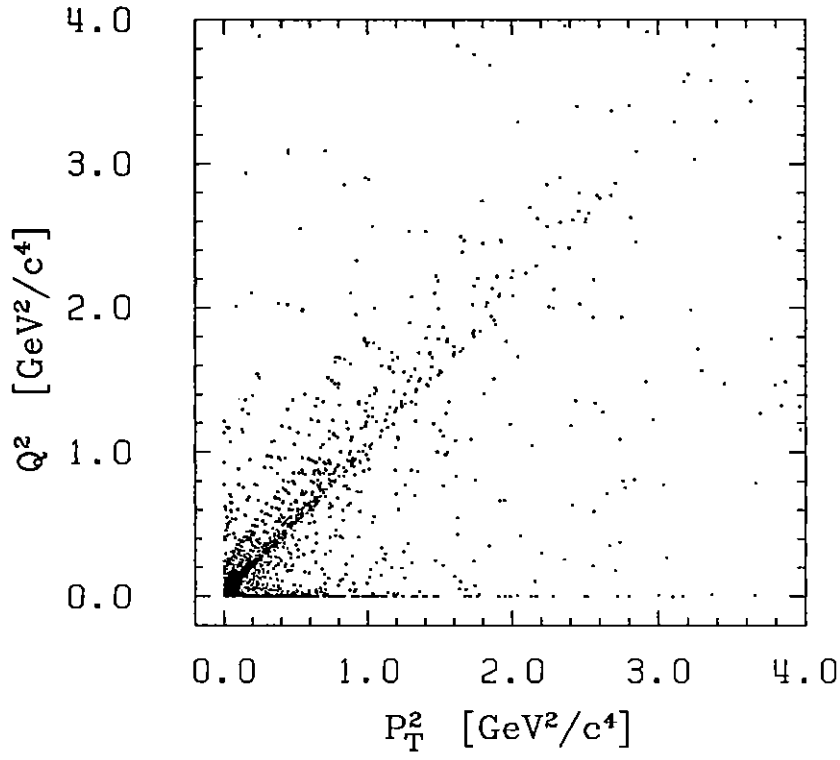

Figure 1.2: Distribution of transverse momentum of two-photon system versus $Q^2 = -q^2$ of the photons.

1.2 Selection Rules in Two-photon Reactions

In order to show which spin-parity states can interfere we have to find the rotation properties of a helicity amplitude M for two-photon coupling to the intermediate state with well defined J^P (eq. 1.8). For our purpose we will use the helicity formalism [14, 15]. Since helicity is invariant under rotations, the plane-wave state of a free photon $|k_i\theta_i\phi_i;\lambda_i\rangle$ with helicity λ_i and momentum k_i in an arbitrary direction (θ_i, ϕ_i) is obtained by rotation of a free photon wave function $|k_i\,\lambda_i\rangle$ with the same helicity and the momentum k_i pointing into the positive z-direction

$$|k_i\theta_i\phi_i;\lambda_i\rangle = R_{\phi_i,\theta_i,-\phi_i}\;|k_i\,\lambda_i\rangle. \tag{1.18}$$

With $R_{\phi_i,\theta_i,-\phi_i}$ we denote a finite rotation of the photon momentum by Euler angles $\phi_i, \theta_i, -\phi_i$. The two-photon state is constructed as a direct product of both photon plane-wave functions

$$R^{(1)}_{\phi_1,\theta_1,-\phi_1}\;|k_1\,\lambda_1\rangle \cdot R^{(2)}_{\phi_2,\theta_2,-\phi_2}\;|k_2\,\lambda_2\rangle\;.$$

In the two-photon center-of-mass system where the momenta of photons point in opposite directions, the two rotations $R^{(1)}$ and $R^{(2)}$ can be replaced by a single rotation R that

acts on both states. Denoting the first photon momentum in this system with magnitude k and polar angles θ and ϕ we arrive at

$$|k\theta\phi;\lambda_1\lambda_2\rangle = R_{\phi,\theta,-\phi}\ |k\,\lambda_1\rangle\ |-k\,\lambda_2\rangle, \tag{1.19}$$

where $|k\,\lambda_i\rangle$ is a helicity function for photons moving up the z axis. An extra minus sign in front of the magnitude k in the second photon helicity function is introduced due to the convention that the second photon moves down the z axis. Since the momentum k and the helicities λ_1 and λ_2 are invariant against rotation, it is possible to assign definite values to them, together with total angular momentum J and its projection J_z. We construct a wave function for two photons with well defined J, J_z, k and both helicities λ_1, λ_2 as a superposition [16] of plane-wave functions from eq. 1.19:

$$|k;JJ_z;\lambda_1\lambda_2\rangle = N_J \int_0^{\pi}\int_0^{2\pi} D^{J}_{J_z\lambda}{}^{*}(\phi,\theta,-\phi)\ |k\theta\phi;\lambda_1\lambda_2\rangle\ sin\theta\ d\theta\ d\phi \tag{1.20}$$

where $\lambda \equiv \lambda_1 - \lambda_2$ and N_J is a normalization factor. Using relation 1.20, one can write elements of the transformation matrix between plane-wave functions and functions with well defined total angular momentum J and its projection J_z as:

$$\langle k'\theta'\phi';\lambda_1'\lambda_2'|k;JJ_z;\lambda_1\lambda_2\rangle = N_J\ \delta(k'-k)\ \delta_{\lambda_1'\lambda_1}\ \delta_{\lambda_2'\lambda_2}\ D^{J}_{J_z\lambda}{}^{*}(\phi',\theta',-\phi') \tag{1.21}$$

The matrix elements are particularly simple in the $\gamma\gamma$ helicity system, with z axis along the first photon momentum, where both polar angles θ' and ϕ' are zero, and so the rotation matrices $D^{J}_{J_z\lambda}$ are equal to 1. As a consequence the elements of the matrix $\langle k'00;\lambda_1'\lambda_2'|k;JJ_z;\lambda_1\lambda_2\rangle$ are just products of δ functions.

The advantage of using wave-functions with well defined helicities for each particle (eq. 1.20) is obvious in describing the reaction $a + b \rightarrow c + d$. The S matrix for this reaction

$$\langle E'J'J_z';\lambda_c\lambda_d|\ S\ |EJJ_z;\lambda_a\lambda_b\rangle = \delta(E'-E)\ \delta_{J'J}\ \delta_{J_z'J_z}\ \langle\lambda_c\lambda_d|\ S^J(E)\ |\lambda_a\lambda_b\rangle \tag{1.22}$$

is reduced to submatrices $S^J(E)$, belonging to definite values of energy E and angular momentum J. In the equation are E, J, J_z together with the helicities λ_a, λ_b quantum numbers for the initial state, and similarly E', J', J_z', λ_c, λ_d quantum numbers for the final state. One can see that for parity conserving reactions

$$P^{-1}\ S\ P\ =\ S \tag{1.23}$$

final states differing only in sign of helicity are equally probable if the initial particles are unpolarized, as is the case in two-photon interactions at an e^+e^- collider with unpolarized

beams. Applying the relation 1.23 to the submatrix $S^J(E)$ in the $(J,\ J_z)$-representation and using the behaviour of states with well defined helicities under inversion

$$P\ |EJJ_z;\lambda_1\lambda_2\rangle = \eta_{12}\ |EJJ_z;-\lambda_1-\lambda_2\rangle, \tag{1.24}$$

where η is a phase factor, one finds

$$\langle -\lambda_c\ -\lambda_d|\ S^J(E)\ |-\lambda_a\ -\lambda_b\rangle = \eta_{cd}\eta_{ab}\langle\lambda_c\lambda_d|\ S^J(E)\ |\lambda_a\lambda_b\rangle \tag{1.25}$$

This means that the cross section is equal for both signs of helicity.

In the helicity basis the cross section $d\sigma_{e^+e^-\to e^+e^-X}$ is proportional to the sum (eqs. 1.3, 1.5)

$$d\sigma_{e^+e^-\to e^+e^-X} \propto \sum_{a,a',b,b'} \rho_1^{aa'}\rho_2^{bb'}T^*_{a'b'}T_{ab}. \tag{1.26}$$

Summation indices a, a', b, b' indicate photon helicities. As we have already mentioned (page 7) the off-diagonal elements of the unnormalized photon density flux matrix (eq. 1.7) vanish in the no-tag case due to integration over the scattered electron and positron azimuthal angles. This leads us to the incoherent summation of the T matrix elements for different photon helicities

$$d\sigma_{e^+e^-\to e^+e^-X} \propto \sum_{a,b} \rho_1^{aa}\rho_2^{bb}|T_{ab}|^2. \tag{1.27}$$

Since the two-photon helicity $\lambda = a - b$ coincides with J_z, only the interference between states with equal J_z projection can be studied in the no-tag case.

Helicity matrix elements M_{ab} for two-photon formation of states with total angular momentum J smaller then two-photon helicity difference $|a-b|$ are zero:

$$M_{\pm\mp}(J=0,1) = 0 \tag{1.28}$$

$$M_{0\pm}(J=0) = 0. \tag{1.29}$$

Some further reduction of independent matrix elements can be done also due to parity conservation. For helicity amplitudes M_{ab}, the following behaviour under helicity-flip can be shown [10]:

$$M_{ab} = M_{-a\ -b} \quad \text{for } J^P = 0^+, 1^-, 2^+, J^{+(-1)^J}, \ldots \quad \text{(natural states)} \tag{1.30}$$

$$M_{ab} = -M_{-a\ -b} \quad \text{for } J^P = 0^-, 1^+, 2^-, J^{-(-1)^J}, \ldots \quad \text{(unnatural states)} \tag{1.31}$$

This leads to zero matrix element for formation of unnatural spin-parity states with two longitudinaly polarized photons

$$M_{00}(J^P = 0^-, 1^+, 2^-, \ldots) = 0. \tag{1.32}$$

Different behaviour of natural and unnatural spin-parity states under helicity-flips prevents an interference between states with different naturality η. For description of an interaction between two real photons only four terms have to be considered in a no-tag reaction:

$$d\sigma_{e^+e^-\to e^+e^-X} \propto \rho_1^{++}\rho_2^{++}(T^*_{++}T_{++} + T^*_{--}T_{--} + T^*_{+-}T_{+-} + T^*_{-+}T_{-+}). \quad (1.33)$$

Each T matrix element can be split into terms describing production of states with positive and negative naturalities

$$T_{ab} = T_{ab}^{\eta=+} + T_{ab}^{\eta=-}. \quad (1.34)$$

Applying the relations 1.30, 1.31 on combined terms $T^*_{++}T_{++} + T^*_{--}T_{--}$ and $T^*_{+-}T_{+-} + T^*_{-+}T_{-+}$ one can see that products of T matrix elements with different naturalities cancel. So the relation 1.33 transforms to

$$d\sigma_{e^+e^-\to e^+e^-X} \propto \rho_1^{++}\rho_2^{++}(T_{++}^{\eta=+*}T_{++}^{\eta=+} + T_{++}^{\eta=-*}T_{++}^{\eta=-} + T_{+-}^{\eta=+*}T_{+-}^{\eta=+} + T_{+-}^{\eta=-*}T_{+-}^{\eta=-}) \quad (1.35)$$

It means that in no-tag interactions of two real photons, there is no interference between states of different naturalities.

For real photons, some further restrictions on helicity matrix elements M_{ab} can be derived from the principle of invariance under space rotation and inversion [8]. There are four helicity functions for two real photons in their center-of-mass system, propagating in the opposite directions along the z-axis

$$\begin{aligned} \Psi^{++} &= |k\ +1\rangle\ |-k\ +1\rangle \\ \Psi^{--} &= |k\ -1\rangle\ |-k\ -1\rangle \\ \Psi^{+-} &= |k\ +1\rangle\ |-k\ -1\rangle \\ \Psi^{-+} &= |k\ -1\rangle\ |-k\ +1\rangle. \end{aligned} \quad (1.36)$$

A single photon helicity function $|k\lambda\rangle$ transforms under a rotation R_ϕ around the z-axis by an angle ϕ, a rotation R_x around the x-axis for 180^o and a parity transformation P in the following ways:

$$\begin{aligned} R_\phi|k\lambda\rangle &= e^{i\lambda\phi}|k\lambda\rangle \\ R_x|k\lambda\rangle &= |-k\lambda\rangle \\ P\,|k\lambda\rangle &= |-k-\lambda\rangle \end{aligned} \quad (1.37)$$

Using these relations, two-photon eigenstates of R_ϕ and P can be constructed from helicity functions 1.36

$$\Psi^{++} + \Psi^{--} = |k+1\rangle\ |-k+1\rangle + |k-1\rangle\ |-k-1\rangle$$

	$\Psi^{++}+\Psi^{--}$	$\Psi^{++}-\Psi^{--}$	Ψ^{+-}	Ψ^{-+}
R_ϕ	1	1	$e^{2i\phi}$	$e^{-2i\phi}$
R_x	1	1		
P	1	-1	1	1

Table 1.3: Eigenvalues of the rotations R_ϕ, R_x and the inversion P for four two-photon helicity states.

$$\begin{aligned} \Psi^{++}-\Psi^{--} &= |k+1\rangle\,|-k+1\rangle - |k-1\rangle\,|-k-1\rangle \\ \Psi^{+-} &= |k+1\rangle\,|-k-1\rangle \\ \Psi^{-+} &= |k-1\rangle\,|-k+1\rangle. \end{aligned} \tag{1.38}$$

The behaviour of these states under both rotations R_ϕ, R_x and inversion P is listed in table 1.3. Only the function $\Psi^{++}-\Psi^{--}$ can be used to describe a formation of a state with negative parity while other three functions $\Psi^{++}+\Psi^{--}$, Ψ^{+-} and Ψ^{-+} describe a formation of a state with positive parity. From table 1.3 it is possible to see that functions $\Psi^{++}+\Psi^{--}$ and $\Psi^{++}-\Psi^{--}$ are both simultaneous eigenstates of R_ϕ and R_x with eigenvalue one. On the contrary, eigenvalues of intermediate states with an odd total angular momentum J are not equal to one for both rotations R_ϕ and R_x, simultaneously. The rotation properties of these states ($J=1,3,5,\ldots$) are described with the spherical harmonics Y_{J0} and therefore the sign is changed under the rotation R_x for $J=1,3,5,\ldots$. So the formation of an intermediate states with an odd total angular momentum can only be described with functions Ψ^{+-} and Ψ^{-+}. Considering also that the helicity of two photons should not exceed the total angular momentum J of the intermediate state (eqs. 1.28, 1.29), only a small number of helicity amplitudes remains nonzero:

$$M_{\pm\pm}(J^P=0^\pm,2^\pm,4^\pm,\ldots) \neq 0 \quad \text{with} \quad J_z=0 \tag{1.39}$$

$$M_{\pm\mp}(J^P=2^+,3^+,4^+,\ldots) \neq 0 \quad \text{with} \quad J_z=\pm 2. \tag{1.40}$$

All other matrix elements vanish.

1.3 Decay of states with well defined J^P into $\omega\rho^0$

The rotation properties for a decay of a state with well defined spin-parity J^P into two vector mesons, ω and ρ^0, are described by a wave function $\Psi^{L\,j}_{JP\;J_z}$. The function is written as a sum of products between both meson spin functions $|j_\omega, m_\omega\rangle$, $|j_\rho, m_\rho\rangle$ and a spherical function Y^M_L describing an orbital angular momentum in the $\omega\rho^0$ system

$$\Psi^{L\,j}_{JP\;J_z} = \sum_{\substack{m,M \\ m+M=J_z}} \sum_{\substack{m_\omega, m_\rho \\ m_\omega+m_\rho=m}} C^{J\;J_z}_{j\;m,\;L\;M}\, C^{j\;m}_{j_\omega\;m_\omega,\;j_\rho\;m_\rho}\, Y^M_L(\theta,\phi)\cdot|j_\omega, m_\omega\rangle\cdot|j_\rho, m_\rho\rangle \quad . \tag{1.41}$$

The wave function $\Psi^{L\,j}_{JP\;J_z}$ is constructed by first combining the spins of the vector mesons and subsequently adding the orbital angular momentum to obtain the total spin J. In the equation Clebsch-Gordon coefficients are marked with C. Angles θ and ϕ in eq. 1.41 are polar and azimuthal angles of the ω meson in the $\gamma\gamma$ helicity system. The system lies in the $\gamma\gamma$ center-of-mass, having the z axis along one of the photons.

The ρ^0 meson is a spin one particle with negative parity. At its dominant decay into two spinless pions its total angular momentum coincides with the orbital angular momentum of the two pions in the ρ^0 rest frame. Therefore, the ρ^0 spin function $|j_\rho, m_\rho\rangle$ is represented by the spherical function $Y_1^{m_\rho}(\theta_\rho, \phi_\rho)$

$$|j_\rho, m_\rho\rangle = Y_1^{m_\rho}(\theta_\rho, \phi_\rho) \; . \tag{1.42}$$

The angles θ_ρ and ϕ_ρ define the direction of π^+ in the ρ^0 center-of-mass system where coordinate axes are parallel to the axes in the $\gamma\gamma$ helicity system.

The ω meson is also a spin one particle with negative parity and so represented by a vector. For its dominant decay into three pions the wave function is written as a product of a spatial function with intrinsic functions of all three pions. Since pions are spinless particles with negative intrinsic parity, the spatial function corresponds to an axial vector with $J^P = 1^+$. There is only one independent axial vector that can be formed from the pion momenta in the ω rest system, namely a cross product of two pion momenta. Therefore, the ω spin function is written as

$$|j_\omega\rangle = N \cdot \frac{(\vec{p}_{\pi+} \times \vec{p}_{\pi-})}{|\vec{p}_{\pi+} \times \vec{p}_{\pi-}|} = N \cdot \vec{n} \tag{1.43}$$

where $\vec{n}$ is the unit vector normal to the decay plane in the ω rest frame. The constant N is obtained from normalization of the spin function. By using the helicity basis vectors

$$\vec{e}_+ = \begin{pmatrix} 1 \\ i \\ 0 \end{pmatrix}, \quad \vec{e}_- = \begin{pmatrix} 1 \\ -i \\ 0 \end{pmatrix}, \quad \vec{e}_0 = \begin{pmatrix} 0 \\ 0 \\ 1 \end{pmatrix} \tag{1.44}$$

we arrive at the helicity representation of the spin function

$$|j_\omega, m_\omega\rangle = N\ \vec{n}\cdot\vec{e}_{m_\omega} = Y_{j_\omega}^{m_\omega}(\theta_n, \phi_n) \tag{1.45}$$

where θ_n, ϕ_n denote the angles of the vector $\vec{n}$.

Both vector mesons ω and ρ are short lived particles with a finite width of mass distribution. To describe their mass distributions, we factorize the decay matrix element $D_{J_z}(R \to X)$

$$\begin{aligned} D_{J_z}(R \to \pi^+\pi^-\pi^+\pi^0\pi^-) \ &= \ M(\rho^0 \to \pi^+\pi^-)\left[m_\rho^2 - s_{2\pi} - im_\rho\Gamma_\rho\right]^{-1} \\ & M(\omega \to \pi^+\pi^0\pi^-)\left[m_\omega^2 - s_{3\pi} - im_\omega\Gamma_\omega\right]^{-1} M(R \to \rho^0\omega) \end{aligned} \tag{1.46}$$

into the matrix element describing production of ω and ρ^0 $M(R \to \rho^0\omega)$, elements for their decays $M(\rho^0 \to \pi^+\pi^-)$, $M(\omega \to \pi^+\pi^0\pi^-)$ and relativistic propagators of both vector mesons [17, 18]. In the equation above $s_{2\pi}$ and $s_{3\pi}$ denote squares of $\pi^+\pi^-$ and $\pi^+\pi^0\pi^-$ invariant mass, respectively.

The decay matrix element $M(\rho^0 \to \pi^+\pi^-)$ linearly depends on the ρ^0 meson polarization vector ε. As the matrix element has to be Lorentz invariant, ε occurs in a scalar product with pion four-momenta. Due to gauge invariance $(p_{\pi^+} + p_{\pi^-})\cdot\varepsilon = 0$, only one coupling constant $G_{\rho\pi\pi}$ is needed to describe the matrix element $M(\rho^0 \to \pi^+\pi^-)$

$$M(\rho^0 \to \pi^+\pi^-) = G_{\rho\pi\pi}\ \varepsilon_\mu\ (p_{\pi^+} - p_{\pi^-})^\mu = -2\ G_{\rho\pi\pi}\ \vec{\varepsilon}\cdot\vec{p}_{\pi^+}, \tag{1.47}$$

where the last expression is valid only in the ρ^0 meson center-of-mass system. For the polarization $\vec{\varepsilon}$ describing a ρ^0 meson with well defined spin projection m_ρ, the above relation leads us to the same angular distribution as it is described with the ρ^0 spin function $|j_\rho, m_\rho\rangle$

$$M(\rho^0 \to \pi^+\pi^-) = 2\ G_{\rho\pi\pi}\ p_{\pi^+}\ |j_\rho, m_\rho\rangle\ . \tag{1.48}$$

Applying the Fermi golden rule, we arrive at the partial width for the ρ^0 decay into two pions

$$m_\rho\Gamma_\rho(\rho^0 \to 2\pi) = \frac{1}{6\pi}\ G_{\rho\pi\pi}^2\ \frac{p_{\pi^+}^3}{\sqrt{s_{2\pi}}}\ . \tag{1.49}$$

This enables us to express the decay matrix element $M(\rho^0 \to \pi^+\pi^-)$ with the partial width $\Gamma_\rho(\rho^0 \to 2\pi)$

$$M(\rho^0 \to \pi^+\pi^-) = 2\sqrt{6\pi}\frac{\sqrt[4]{s_{2\pi}}}{\sqrt{p_{\pi^+}}}\ \sqrt{m_\rho\Gamma_\rho(\rho^0 \to 2\pi)}\ |j_\rho, m_\rho\rangle \tag{1.50}$$

Combining the decay matrix element $M(\rho^0 \to \pi^+\pi^-)$ with the ρ^0 propagator, we arrive at the relativistic Breit-Wigner amplitude

$$\mathcal{A}^{\rho}_{BW} = \frac{\sqrt{m_\rho \Gamma_\rho(\rho^0 \to 2\pi)}}{\pi(m_\rho^2 - s_{2\pi} - i m_\rho \Gamma_\rho)} \cdot \frac{\sqrt[4]{s_{2\pi}}}{\sqrt{p_{\pi^+}}} \tag{1.51}$$

where the angular distribution $|j_\rho, m_\rho\rangle$ and some numerical factors are omitted. Since the ρ^0 meson is a broad resonance with nominal mass $m_\rho = 768$ MeV and width $\Gamma_\rho = 149$ MeV [19], the $\pi^+\pi^-$ invariant mass distribution deviates from the one obtained from the relativistic Breit-Wigner amplitude $\mathcal{A}^{\rho}_{BW}$. The disagreement can be removed by introducing the width dependence on the two-pion invariant mass [20, 18]

$$\Gamma_\rho(s) = \Gamma_\rho(m_\rho^2) \left(\frac{s - 4\, m_\pi^2}{m_\rho^2 - 4\, m_\pi^2} \right)^{3/2} \frac{m_\rho}{\sqrt{s}} \tag{1.52}$$

The decay matrix element for the ω decay into three pions $M(\omega \to 3\pi)$ is obtained in a similar way as the one for the ρ^0 decay. The negative C-parity of the ω requires an odd relative orbital angular momentum for the $\pi^+\pi^-$ pair, while parity and angular momentum conservations require the same for orbital angular momentum between π^0 and the $\pi^+\pi^-$ pair. So, the decay matrix element is described by multiplying the antisymmetric tensor $\epsilon_{\alpha\beta\gamma\delta}$ with the polarization vector of the ω meson and the momenta of all three pions [18]

$$M(\omega \to \pi^+\pi^0\pi^-) = G_{\omega 3\pi}\ \epsilon_{\alpha\beta\gamma\delta} p^{\alpha}_{\pi^+} p^{\beta}_{\pi^0} p^{\gamma}_{\pi^-} \varepsilon^{\delta}\ =\ G_{\omega 3\pi} \lambda\ \vec{\varepsilon} \cdot \vec{n}. \tag{1.53}$$

The last expression is valid only in the ω meson center-of-mass system, where λ equals to

$$\lambda = |E_{\pi^+}(\vec{p}_{\pi^0} \times \vec{p}_{\pi^-})\ +\ E_{\pi^0}(\vec{p}_{\pi^-} \times \vec{p}_{\pi^+})\ +\ E_{\pi^-}(\vec{p}_{\pi^+} \times \vec{p}_{\pi^0})| \tag{1.54}$$

and $\vec{n}$ is a unit vector normal to the three-pion decay plane. In the product $\vec{\varepsilon} \cdot \vec{n}$ one can recognize spin functions $|j_\omega, m_\omega\rangle$ from eq. 1.45. It turns out that the assumption of a constant $G_{\omega 3\pi}$ is in good agreement with the measured Dalitz plot for the ω decay into three pions [21]. That leads us to a relativistic Breit-Wigner amplitude

$$\mathcal{A}^{\omega}_{BW} = \frac{G_{\omega 3\pi}\ \lambda}{\pi(m_\omega^2 - s_{3\pi} - i m_\omega \Gamma_\omega)}\ , \tag{1.55}$$

obtained by combining the matrix element $M(\omega \to \pi^+\pi^0\pi^-)$ and the ω propagator, also here the angular distribution is omitted. Due to the narrowness of the ω resonance, the width Γ_ω can be taken as constant.

Finally, we can express the decay matrix element D_{J_z} introduced in the eq. 1.8. Because the pions with the same charge are identical bosons with spin zero, the matrix

element is symmetrical against the interchange of two like-sign pions. Taking into account this symmetry property we obtain by adding up all the pion permutations P_i, the following expression for the decay matrix element D

$$\begin{aligned} D^{J^P,J_z}_{\omega\rho} &= \left(\mathcal{A}^{\omega}_{BW}\mathcal{A}^{\rho}_{BW}\Psi^{L\ j}_{J^P\ J_z}\right)_{(\pi_1^+\pi_2^-\pi^0\pi_3^+\pi_4^-)} + \left(\mathcal{A}^{\omega}_{BW}\mathcal{A}^{\rho}_{BW}\Psi^{L\ j}_{J^P\ J_z}\right)_{(\pi_3^+\pi_2^-\pi^0\pi_1^+\pi_4^-)} \\ &+\left(\mathcal{A}^{\omega}_{BW}\mathcal{A}^{\rho}_{BW}\Psi^{L\ j}_{J^P\ J_z}\right)_{(\pi_1^+\pi_4^-\pi^0\pi_3^+\pi_2^-)} + \left(\mathcal{A}^{\omega}_{BW}\mathcal{A}^{\rho}_{BW}\Psi^{L\ j}_{J^P\ J_z}\right)_{(\pi_3^+\pi_4^-\pi^0\pi_1^+\pi_2^-)} \\ &= \sum_{i=1}^{4}\left(\mathcal{A}^{\omega}_{BW}\mathcal{A}^{\rho}_{BW}\Psi^{L\ j}_{J^P\ J_z}\right)_{P_i(\pi_1^+\pi_2^-\pi^0\pi_3^+\pi_4^-)} . \end{aligned} \tag{1.56}$$

It is assumed that the matrix element $M(R \to \rho^0\omega)$ describing the production of vector mesons ω and ρ^0, does not depend on the two and three-pions invariant masses.

1.4 Decay of the two-photon state into a $\pi^+\pi^+\pi^0\pi^-\pi^-$ final state

In addition to the $\omega\rho^0$ production, five pion final states are accessible in two-photon interactions also through other channels. In our analysis we include incoherent contributions of $\omega\pi^+\pi^-$, $\rho^0\pi^+\pi^-\pi^0$ and $\pi^+\pi^+\pi^0\pi^-\pi^-$ uniformly distributed in phase space. This assumption is unphysical for the $\omega\pi^+\pi^-$ channel, where requirement of odd two-pion orbital angular momentum, due to C-parity conservation, forbids isotropic angular distributions [3]. However, it will be shown later (chapter 6) that contributions of $\omega\pi^+\pi^-$, $\rho^0\pi^+\pi^-\pi^0$ and $\pi^+\pi^+\pi^0\pi^-\pi^-$ channels are well separated from $\omega\rho^0$ due to different distributions of $\pi^+\pi^-$ and $\pi^+\pi^-\pi^0$ invariant mass. Adding up all the pion permutations, the decay matrix elements for all three channels are

$$D_{\omega\pi^+\pi^-} = \sum_{i=1}^{4}(\mathcal{A}^{\omega}_{BW})_{P_i(\pi_1^+\pi_2^-\pi^0\pi_3^+\pi_4^-)} \tag{1.57}$$

$$D_{\rho\pi^+\pi^-\pi^0} = \sum_{i=1}^{4}(\mathcal{A}^{\rho}_{BW})_{P_i(\pi_1^+\pi_2^-\pi^0\pi_3^+\pi_4^-)} \tag{1.58}$$

$$D_{\pi^+\pi^+\pi^0\pi^-\pi^-} = 1. \tag{1.59}$$

The notation corresponds to the one in eq. 1.56.

1.5 Decay of a two-photon state into vector mesons $\rho^0\phi$ and $\omega\phi$

Beside the partial wave analysis of the five-pion final state, also a study of the two-photon production of vector meson pairs $\rho^0\phi$ and $\omega\phi$ will be presented. Both reactions are analysed by using the dominant decay mode of each vector meson, so the final states for reactions $\gamma\gamma \to \rho^0\phi$ and $\gamma\gamma \to \omega\phi$ are $\pi^+\pi^-K^+K^-$ and $\pi^+\pi^-\pi^0K^+K^-$, respectively. Due to very few events observed, for neither of the two reaction the partial wave analysis could be performed. Therefore, a uniform, phase space distribution of $\rho^0\phi$ and $\omega\phi$ is used. Since particles in the final state are not identical, the decay matrix elements are not symmetrized:

$$D_{\rho\phi} = \mathcal{A}^{\rho}_{BW}\,\mathcal{A}^{\phi}_{BW} \tag{1.60}$$

$$D_{\omega\phi} = \mathcal{A}^{\omega}_{BW}\,\mathcal{A}^{\phi}_{BW}, \tag{1.61}$$

where the Breit-Wigner amplitude $\mathcal{A}^{\phi}_{BW}$ for ϕ is of the same form as for the ρ meson, except for the width that we take as constant.

Chapter 2

The ARGUS Detector

The ARGUS detector [22] is a solenoidal magnetic spectrometer (fig. 2.1), assembled in the south interaction region of DORIS e^+e^- storage ring [23]. The detector provides momentum measurements of charged particles, their identification and measurements of neutral particle direction and energy. It covers over 90 % of the full solid angle. In a magnetic field of 0.8 T [24] inside solenoidal magnet coils are installed a vertex drift chamber [25], a main drift chamber [26], time-of-flight counters [27] and an electromagnetic calorimeter [28, 29]. Further outwards follow an iron flux return yoke and three layers of proportional tubes [30] serving for muon identification. Most hadrons are absorbed in the electromagnetic calorimeter, magnet coils or in the flux return yoke before they reach the proportional tubes, the so called muon chambers. Around the beam tube are placed compensation coils shielding mini-beta quadrupoles from the detector's longitudinal magnetic field. The two mini-beta quadrupoles focus the beams on the interaction point. A luminosity of up to $2 \cdot 10^{31} \mathrm{cm}^{-2}\mathrm{s}^{-1}$ is achieved.

2.1 Main Detector Components

The vertex drift chamber is a 1m long cylindrical chamber, with inner and outer radii of 50 and 140mm, respectively. All wires, i.e. 594 sense and 1412 field wires, are parallel to the chamber axis, hence the coordinate in the beam direction is not measured. They are arranged in a close-packed hexagonal cell pattern. The spatial resolution of the vertex drift chamber is about 90 μm.

The main drift chamber represents the central track detector of ARGUS. Its length equals to 2m, inner radious to 15 cm and outer radious to 85cm. The chamber contains 5940 sense wires and 24588 potential wires arranged in 36 concentric layers of 18.0 mm $\times$ 18.8 mm large drift cells. The spatial resolution of around 190 μm reflects in a good

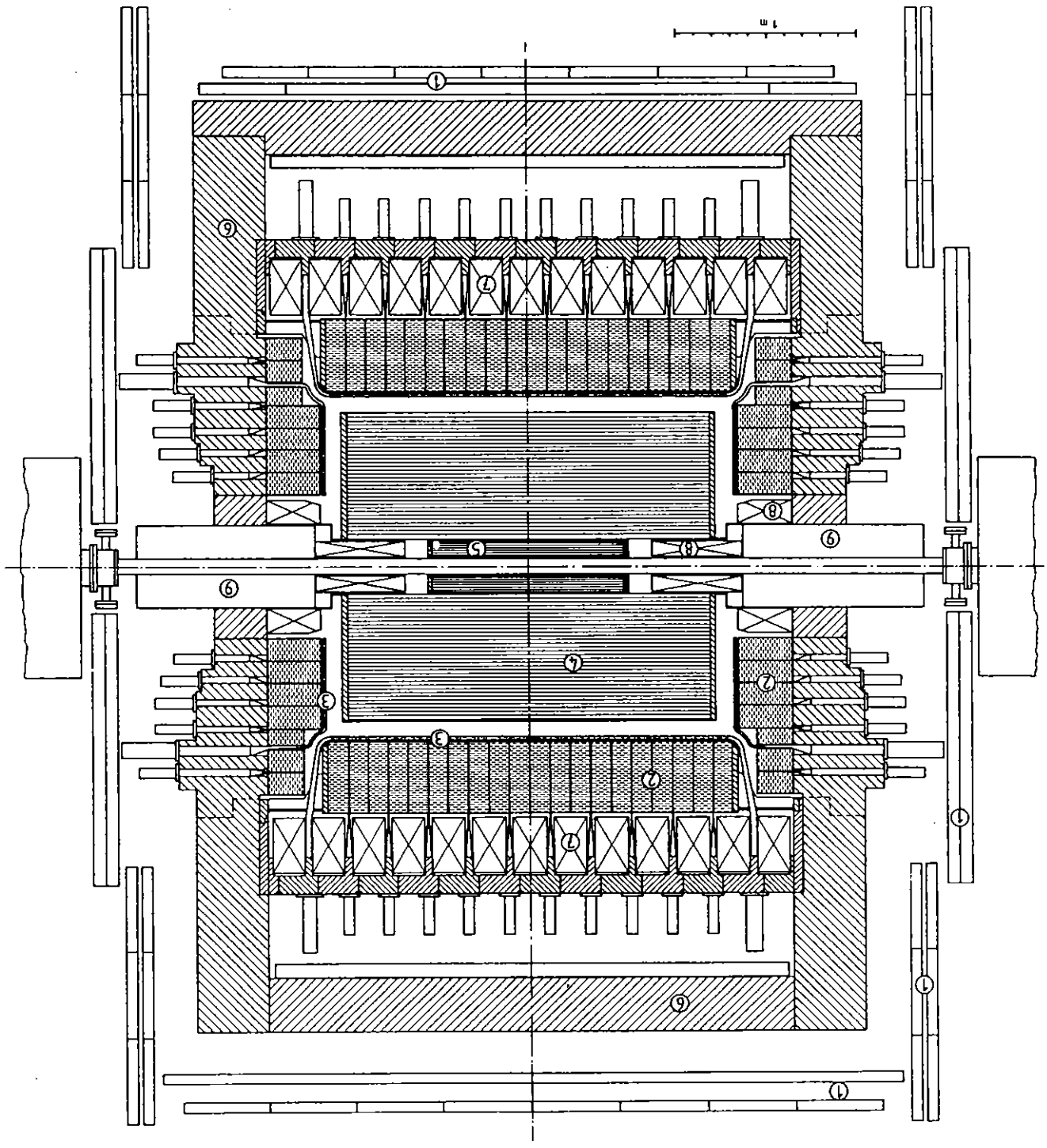

1 Muon Chambers	2 Electromagnetic Calorimeter	3 Time-of-flight Counters
4 Main Drift Chamber	5 Vertex Drift Chamber	6 Iron Yoke
7 Magnet Coils	8 Compensation Coils	9 Mini-beta Quadrupols

Figure 2.1: The ARGUS detector

resolution of transverse momentum $\sigma(p_T)/p_T = \sqrt{0.01^2 + (0.009\ p_T[GeV/c])^2}$. Tilted sense wires in every second layer allow a determination of the track coordinates along the beam direction. The chamber is filled with the gas mixture of 97% propane, 3% methylal and 0.2% H_2O. This results in a good resolution in the measurement of specific ionization, $\sigma(dE/dx)/(dE/dx) \approx 5\%$ for charged hadrons.

The time-of-flight counters, made of 20mm thick NE110 scintillator, are tightly packed between the main drift chamber and the calorimeter modules. Each of the 64 barrel counters is read out by two photomultipliers while, due to the geometric restrictions, the 2×48 endcap counters are read out from one end only. The time resolution of the time-of-flight system for hadrons is 220 ps (r.m.s.).

The electromagnetic calorimeter consists of 1760 modules arranged into two hemispheres with 10 rings of 64 modules in the barrel region and 5 concentric rings containing 64, 56, 48, 40 and 32 modules in the endcap region. The modules are of the lead-scintillator sandwich type, with alternating layers of 5 mm scintillator and 1 mm lead in the barrel modules, while lead layers in the endcap region are 1.5 mm thick. The overall depth of each module corresponds to 12.5 radiation lengths, and its width to 1.0 (0.9) Moliere radius for the barrel (endcap) modules. In the calorimeter, only electron and photon energy can precisely be measured. The energy resolution achieved is $\sigma_E/E = \sqrt{0.072^2 + 0.065^2/E[GeV]}$ in the barrel part of the detector and $\sigma_E/E = \sqrt{0.075^2 + 0.076^2/E[GeV]}$ in the endcap parts. The photon production angle derived from center-of-energy of the shower is measured with precision of $\sigma = 13$ mrad and $\sigma = 10$ mrad in the barrel and endcap regions, respectively.

The muon chambers consist of 1744 proportional tubes arranged in three layers, one inside the iron yoke and two outside. Only muons with momentum greater than 1.1 GeV/c can penetrate the iron yoke and produce signals in the outer layers. The momentum cutoff for the inner chambers is only 0.7 GeV/c. The muon chambers operate with a gas mixture of 92% argon and 8% propane.

2.2 The Trigger System

The first level trigger relies entirely on fast scintillator counters, the time-of-flight counters and the electromagnetic calorimeter. It is followed by a slower second level trigger system called Little Track Finder (LTF). The LTF microprocessor searches for charged tracks in the main drift chamber, covering a pattern of hit wires with predefined track masks [31]. If a number of found tracks exceeds the required threshold, the event is selected and read out. The on-line computer PDP 11/45 receives the event data from a CAMAC system

and transfers them on an event-by-event basis to the VAX 11/780, which stores the data on a disc unit. After extracting monitoring information, the VAX 11/780 sends the data to the IBM main computer.

The event is accepted if one of the following trigger conditions is fulfilled:
ETOT: The Total Energy Trigger requires that the sum of the energies deposited in either calorimeter hemisphere exceeds 0.7 GeV. This is the only trigger applying the endcap calorimeter modules.
HESH: The High Energy Shower trigger requires the deposited energy in a single HESH group of modules to exceed 1 GeV. Each of 16 HESH groups contains barrel modules of the same hemisphere covering about 70° in the azimuth. In addition the LTF processor has to find at least one charged track.
CPPT: The Charged Particle Pre-Trigger is designed to trigger on events with several charged particles. At least one charged track has to be found in each hemisphere. On the pretrigger level a track is defined as a coincidence between signals coming from time-of-flight counters and calorimeter modules of the same CPPT group. Each CPPT group consists of 6 time-of-flight counters in the barrel region and 6 × 10 calorimeter modules lying behind them in the same hemisphere. Also the LTF processor has to find at least two charged tracks in the main drift chamber.
CMT: The Coincidence Matrix Trigger uses the same groups as CPPT trigger to recognize charged track. Instead of crossing different hemispheres, tracks are required to produce signals in two groups separated by more than 90° in the azimuthal angle. Also in this case the LTF processor is required to recognize two charged tracks.
COSMIC: The Cosmic Ray Trigger is a test trigger. It searches for cosmic muons requiring a coincidence between two opposite groups of four barrel time-of-flight counters.
RANDOM: The Random Trigger is the second test trigger. It gives a random gate to read out electronics at a predefined average rate of, normally 0.1 Hz. During data acquisition it is usually switched on in order to record events needed for off-line estimation of noise in the detector.

The first four triggers have to be in coincidence with the bunch-crossing signal.

2.3 Identification of Charged Particles

Charged particle identification is based on two independent methods. Electrons, muons, pions, kaons and protons can be identified by measuring their specific energy loss dE/dx due to ionization in the drift chamber gas. Measurements of the time-of-flight (TOF)

together with the information on momentum from the drift chamber, allows the reconstruction of particle's mass. For both methods we compare the measured values with values calculated for each particle hypothesis. The calculations base on measured particle momenta. For measured energy loss dE/dx the difference $\chi_i^2(dE/dx)$ is calculated as

$$\chi_i^2(dE/dx) = \frac{(dE/dx - dE/dx_i^{th})^2}{\sigma_{dE/dx}^2 + \sigma_{th}^2} \quad (i = e,\ \mu,\ \pi,\ K,\ p) \tag{2.1}$$

where dE/dx_i^{th} is the specific energy loss calculated for the i-th particle hypothesis. σ_{th}^2 is the uncertainty of the calculated dE/dx value introduced by the momentum uncertainty while $\sigma_{dE/dx}^2$ is the uncertainty of the specific ionization measurements. Analogously, the χ_i^2(TOF) is calculated by comparing the measured particle velocity β with predicted ones β_i^{th}

$$\chi_i^2(\mathrm{TOF}) = \frac{(1/\beta - 1/\beta_i^{th})^2}{\sigma_{\mathrm{TOF}}^2 + \sigma_{th}^2} \ . \tag{2.2}$$

Here σ_{TOF} and σ_{th} are the uncertainties of measured and expected velocities, respectively. The $\chi_i^2(dE/dx)$ and the χ_i^2(TOF) are added up to give a single charged particle identification χ^2

$$\chi_i^2 = \chi_i^2(dE/dx) + \chi_i^2(\mathrm{TOF}) \ . \tag{2.3}$$

If one of both measurements, dE/dx or TOF, is not performed well, only the other is used for particle identification. In case of no signal in the muon chambers, the χ^2 for muons is increased proportionally to the probability that a track treated as a muon, reaches the muon chambers. From dE/dx and TOF measurements we calculate the probability L_i^o for particular mass hypotheses m_i

$$L_i^o = exp(-\chi_i^2/2) \ . \tag{2.4}$$

In addition to dE/dx and TOF measurements, there are two further independent methods for lepton identification. Electrons with momenta greater than 400 MeV/c can be separated from other charged particles using the information from the calorimeter. In contrast to other charged particles, electrons deposit in the calorimeter almost all energy. It is spread only among modules that surround the impact point. This property is used to calculate the probability P_e that the particle is an electron. The calculation is described in details in reference [32]. Since electrons with momenta above 400 MeV/c can be unambiguously identified only by the information from the calorimeter, the likelihood function for such particles L_e equals to P_e

$$L_e \ = \ P_e \qquad (p > 400\mathrm{MeV/c}). \tag{2.5}$$

Also other four functions L_i have to be redefined

$$L_i = \frac{1-P_e}{\sum_{k\neq e} L_k^o} \cdot L_i^o \qquad (i = \mu,\ \pi,\ K,\ p) \tag{2.6}$$

where L_i^o denotes likelihood functions obtained from dE/dx and TOF measurements (eq. 2.4).

Muons deposit in the calorimeter only a small fraction of their energy. It is concentrated in even narrower clusters as they are observed for electrons. The three layers of muon chambers are important for muon identification. Positions of hits in these chambers are compared with the impact point of extrapolated track from the drift chamber. All this information including the energy loss dE/dx in the drift chamber is applied in the calculation of muon probability P_μ [33]. In case of signal in the muon chambers $P_\mu > 0$, the likelihood functions L_i are introduced as

$$\begin{aligned} L_\mu &= P_\mu \qquad (P_\mu > 0) \\ L_i &= \frac{1-P_\mu}{\sum_{k\neq\mu} L_k^o} \cdot L_i^o \qquad (i = e,\ \pi,\ K,\ p) \end{aligned} \tag{2.7}$$

while a relative normalization between different identification methods is even more complicated if both probabilities, P_e and P_μ, are used for particle identification

$$\begin{aligned} L_i &= \frac{1-(1-P_e)(1-P_\mu)}{P_e+P_\mu} \cdot P_i \qquad (i = e,\ \mu) \\ L_j &= \frac{(1-P_e)(1-P_\mu)}{\sum_{k\neq e,\mu} L_k^o} \cdot L_j^o \quad (j = \pi,\ K,\ p)\ . \end{aligned} \tag{2.8}$$

From the likelihood functions L_i we construct normalized probabilities λ_i for particular mass hypotheses m_i

$$\lambda_i = \frac{w^i L_i}{\sum_{k=e,\mu,\pi,K,p} w^k L_k} \tag{2.9}$$

where the w^i are a priori known average particle abundances. The relative rates for particle production typically used at ARGUS are $w^e : w^\mu : w^\pi : w^K : w^p = 1 : 1 : 5 : 1 : 1$. A track is considered to be consistent with a certain mass hypothesis m_i, if the probability λ_i for the same hypothesis exceeds 1 %.

Chapter 3

Monte Carlo Simulation

To determine the cross section of any process, it is crucial to know the detector acceptance and its dependence on the measured quantities. As the acceptance for the detectors used in high energy physics cannot be calculated analytically, a numerical calculation, based on the Monte Carlo method, is applied. The Monte Carlo method is used to describe two-photon interactions using eq. 1.3, behaviour of particles traversing various detector components, the triggering system, and finally also the reconstruction and selection of events. This will be the subject of the following sections.

3.1 Event Generation

We are interested in reactions $e^+e^- \to e^+e^-\gamma\gamma \to e^+e^-X$ (fig. 1.1), in which the two photons are almost real. Therefore, the no-tag luminosity formula of eq. 1.12 will be used. Using the explicit form of the phase-space factor for the scattered electron and positron [7], we arrive at

$$\frac{dL}{d(-q_1^2)d(-q_2^2)d\omega_1 d\omega_2 d\phi} = \frac{\alpha^2}{8\pi^3 q_1^2 q_2^2} \cdot \frac{[(q_1q_2)^2 - q_1^2q_2^2]^{1/2}}{[(p_1p_2)^2 - m_1^2m_2^2]^{3/2}} \cdot s \cdot \rho_1^{++}\rho_2^{++} \qquad (3.1)$$

where s is the square of the e^+e^- center of mass energy. Since the incoming electrons and positrons are unpolarized, only five variables are independent. As a set of independent variables we choose the invariant mass of both photons $-q_1^2$ and $-q_2^2$, their energies ω_1, ω_2 and the angle between the e^+ and e^- scattering planes ϕ.

Due to strong dependence of the luminosity function on $-q_i^2$ and energy ω_i (see fig. 3.1), a standard hit or miss Monte Carlo method is highly inefficient. To improve the Monte Carlo efficiency, a new set of variables is introduced, so that the luminosity function would be as flat as possible with respect to the new variables. As we see from the $-q_i^2$

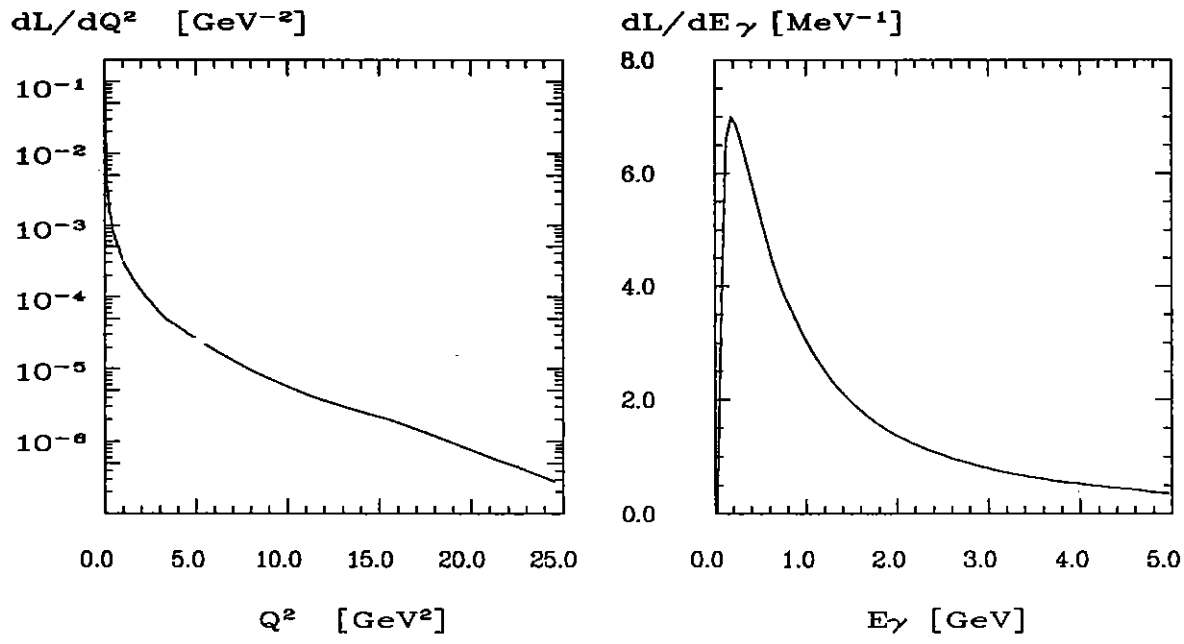

Figure 3.1: Luminosity function as a function of photon invariant mass $Q^2 = -q_i^2$ (left) and photon energy ω_i (right)

and ω_i distributions of the luminosity function in fig. 3.1, they can be well approximated with a distribution

$$\frac{dN}{dx} = \frac{n}{x^r} \tag{3.2}$$

where x stands for $-q_i^2$ or ω_i. The optimum value for r is obtained by fitting distributions in fig. 3.1, and n is a normalization factor. Due to the simple form of the distribution 3.2 one can find a new variable y so that the relation

$$\frac{dN}{dy} = 1 \tag{3.3}$$

is fulfilled. The variable y lies between 0 and 1. Since differential dN is equal in both eqs. 3.2 and 3.3, the variable y is obtained by integrating both sides of the relation

$$dy = \frac{n}{x^r} dx \ . \tag{3.4}$$

For $r \neq 1$ we arrive at the expression

$$y = \frac{x^{1-r} - x_{min}^{1-r}}{x_{max}^{1-r} - x_{min}^{1-r}} \ , \tag{3.5}$$

where x_{min} and x_{max} are boundary values of the old variable x. By inverting the upper relation and introducing the boundary values for ω_i and $-q_i^2$, the old set of variables is

expressed with the new one (u_i, v_i i=1,2) as

$$-q_i^2 = \left[(-q_{min}^2)^{1-r_q} + ((-q_{max}^2)^{1-r_q} - (-q_{min}^2)^{1-r_q}) \cdot u_i \right]^{\frac{1}{1-r_q}} \tag{3.6}$$

$$\omega_i = \left[\omega_{min}^{1-r_\omega} + (\omega_{max}^{1-r_\omega} - \omega_{min}^{1-r_\omega}) \cdot v_i \right]^{\frac{1}{1-r_\omega}} . \tag{3.7}$$

The optimal values for r_q and r_ω are 1.005 and 0.98, respectively. There is no need to replace the variable ϕ since the luminosity function depends only slightly on this variable. The differential luminosity function is written with the new variables as a product

$$\frac{dL}{du_1 du_2 dv_1 dv_2 d\phi} = \frac{dL}{d(-q_1^2)d(-q_2^2)d\omega_1 d\omega_2 d\phi} \cdot \mathcal{J} \tag{3.8}$$

where the Jacobian determinant $\mathcal{J}$ is given for this substitution as

$$\mathcal{J} = \frac{\partial(-q_1^2)}{\partial u_1} \frac{\partial(-q_2^2)}{\partial u_2} \frac{\partial \omega_1}{\partial v_1} \frac{\partial \omega_2}{\partial v_2} =$$

$$\left[\frac{(-q_{max}^2)^{1-r_q} - (-q_{min}^2)^{1-r_q}}{1-r_q} \right]^2 \left[\frac{\omega_{max}^{1-r_\omega} - \omega_{min}^{1-r_\omega}}{1-r_\omega} \right]^2 \cdot (-q_1^2)^{r_q} (-q_2^2)^{r_q} \, \omega_1^{r_\omega} \omega_2^{r_\omega} \tag{3.9}$$

The maximal energy of each photon ω_{max} depends on the beam energy E_B

$$\omega_{max} = E_B - m_e \tag{3.10}$$

while the minimum energy ω_{min} is related to a two-photon invariant mass $W_{\gamma\gamma}$ calculated from the four momenta of both photons q_1 and q_2

$$W_{\gamma\gamma}^2 = (q_1 + q_2)^2. \tag{3.11}$$

The invariant mass $W_{\gamma\gamma}$ in two-photon interactions is distributed between the threshold energy $W_{\gamma\gamma\ min}$ for production of a final state X and the kinematical limit at

$$W_{\gamma\gamma\ max} = 2(E_B - m_e). \tag{3.12}$$

Using the relation 3.11 one can obtain from the threshold energy $W_{\gamma\gamma\ min}$ the minimum photon energy

$$\omega_{min} = \frac{W_{\gamma\gamma\ min}^2}{4(E_B - m_e)} . \tag{3.13}$$

The invariant mass of each photon $-q_i^2$ is greater than

$$-q_{min}^2 = m_e^2 \frac{W_{\gamma\gamma\ min}^4}{s(s - W_{\gamma\gamma\ min}^2)} \tag{3.14}$$

and smaller than

$$-q^2_{max} = (2E_B)^2 \ . \tag{3.15}$$

In the single photon plane defined with u_i and v_i, there are also unphysical regions where the photon momentum is greater than the momentum of impact electron or positron. To reject these cases it is sufficient to require cosine of the scattered electron and positron to lie between -1 and 1.

For the calculation of the two-photon cross section $\sigma_{\gamma\gamma\to X}$ we have to calculate the differential luminosity function $dL/dW_{\gamma\gamma}$ as a function of the two-photon invariant mass $W_{\gamma\gamma}$. It is obtained by numerical integration of eq. 3.8. All variables u_1, u_2, v_1, v_2, ϕ are uniformly generated as it is required for event generation. Number of trails N_i with $W_{\gamma\gamma}$ inside the i-th $W_{\gamma\gamma}$ interval is obtained by the hit or miss method by comparing the values of the luminosity function for generated variables with its maximal value f_{max}. An integral of the luminosity function over the i-th $W_{\gamma\gamma}$ interval is a product of the ratio N_i/N between accepted N_i and all generated events N with its maximal function value f_{max} and a generation volume V

$$\int_{-\frac{\Delta W_{\gamma\gamma}}{2}}^{+\frac{\Delta W_{\gamma\gamma}}{2}} \frac{dL}{dW_{\gamma\gamma}}(W^i_{\gamma\gamma} + W)dW = V \cdot f_{max} \ \frac{N_i}{N} \ , \tag{3.16}$$

where $W^i_{\gamma\gamma}$ and $\Delta W_{\gamma\gamma}$ denote the center value and the width of the i-th interval, respectively. For independent variables, the volume V equals to a product of all variable intervals. In our case $V = 2\pi$. Dividing the above relation by the interval width $\Delta W_{\gamma\gamma}$, we approximate the differential two-photon luminosity function

$$\frac{dL}{dW_{\gamma\gamma}}(W^i_{\gamma\gamma}) = V \cdot f_{max} \ \frac{N_i}{N} \ \frac{1}{\Delta W_{\gamma\gamma}} \ . \tag{3.17}$$

The function $dL/dW_{\gamma\gamma}$ is shown in fig. 3.2. In a similar way we find also a projection of the luminosity function on two-photon transverse momentum p_T (fig. 3.3). Sharp peaking of this projection at low values of transverse momentum is essential for the analysis of interactions between two almost real photons.

Once the kinematical variables describing the scattered leptons and the momentum of the two-photon center-of-mass system are calculated, the event generation continues with a simulation of two-photon reaction. To describe this part of the interaction $e^+e^- \to e^+e^-X$ we use the expressions, needed for the two-photon cross sections $\sigma_{\gamma\gamma\to X}$, from chapter 1. Matrix elements M_{ab} listed in table 1.2 and form factors (eq. 1.17) predicted by the VMD model are used to describe two-photon formation of a state with well defined J^P. To describe the formation of intermediate states where no exact J^P is required, we use a dependence on photon q^2_i predicted by the VMD form factors. The matrix elements

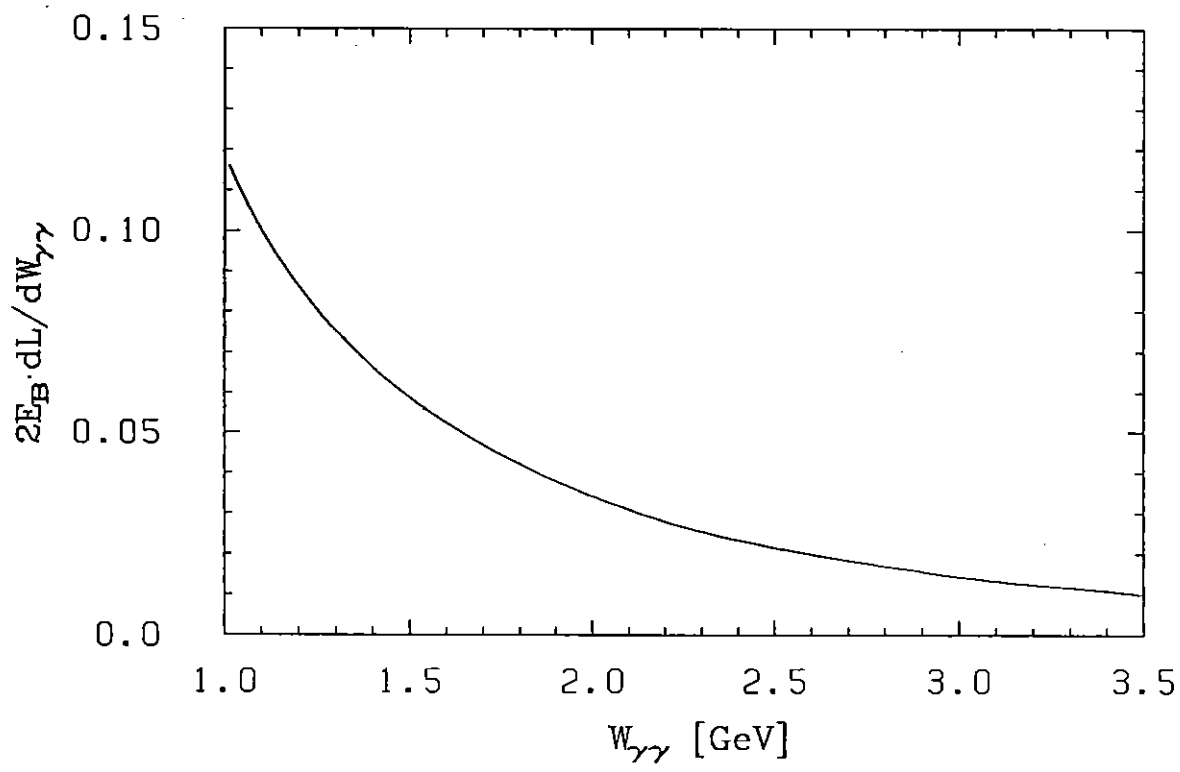

Figure 3.2: The differential two-photon luminosity function obtained by numerical integration. The beam energy is $E_B = 5.2$ GeV.

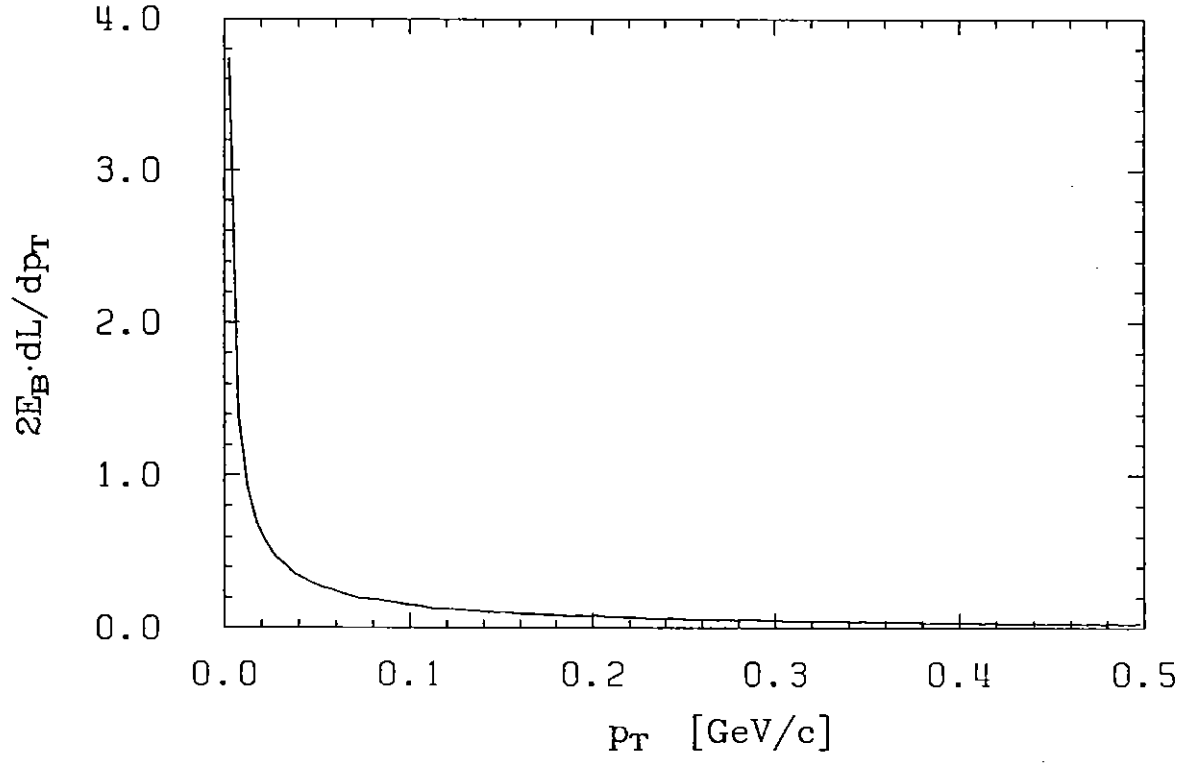

Figure 3.3: Projection of two-photon luminosity function on the transverse momentum p_T of the two-photon system.

M_{ab} are neither calculated from the first principles nor experimentally determined, so one should find out how much the acceptance calculation really depends on the matrix elements M_{ab} applied. To find this out, the acceptance has been determined also for a constant matrix element M_{ab}. In comparison with acceptance calculated with M_{ab} as suggested in chapter 1, the difference is found to be negligible (chapter 6).

The decay of the intermediate state is generated according to the phase space of final state particles weighted by the square of the decay matrix elements D explained in chapter 1. The exact expressions for the square of the $\omega\rho^0$ decay matrix elements are given in appendix A. For the simulation of the decay the "hit or miss" method is applied.

3.2 Detector and Trigger Simulation

Particles produced by the event generator are traced through the detector components shown in fig. 2.1. For detector simulation, the program SIMARG [34] is used as a frame. It is based on the program GEANT [35] that constitutes a framework for handling detector geometry and particle tracking. The energy loss along tracks of charged particles is generated according to a truncated Landau distribution [36] in all detector components except in the drift chambers where the spectrum measured in the chamber prototype, is used instead. The electromagnetic interactions are described by using the EGS program package [37] while hadronic interactions with the detector material are generated by routins from the program GHEISHA [38]. The simulation of drift times in the chambers is made according to measured drift time-space relations. New particles, obtained as a result of an interaction in the detector or a particle decay, are treated in the same way as the original ones. Finally, the deposited energies and measured times in detector components are converted to a digital form and stored using the same format as at the data acquisition.

The SIMARG output serves as the input for event reconstruction. The same program is used for the reconstruction of Monte Carlo events as it is used for measured events. Passing the simulated events through the same preselection criteria and analysis cuts as experimental data enables us to calculate the detector acceptance and resolution of physically interesting measured quantities.

In the case of two-photon interactions, where events have typically low multiplicity, it is in addition to detector acceptance crucial to determine the efficiency of the trigger. To study the efficiency we choose two-prong reactions that are the most sensitive to trigger conditions [39]. From this sample Bhabha tracks are excluded. The trigger simulation is divided into several periods of stable triggering conditions. The stability of triggering

system can be estimated from acceptance uncorrected cross section of two-prong reactions presented as a function of run number. For each trigger period we determine thresholds, trigger logic and efficiencies of trigger components. These quantities are obtained from the experimental data and taken as an input for a trigger simulation. The simulated trigger efficiencies have been compared with trigger efficiencies deduced directly from the measured data in the following way. In the transition $\Upsilon(2S) \rightarrow \Upsilon(1S)\pi^+\pi^-$ followed by $\Upsilon(1S) \rightarrow e^+e^-$ the trigger conditions are almost always fulfiled, due to the high energy of both leptons (ETOT trigger section 2.2). The ratio between events where pions alone had also set a trigger and all events with ETOT set has been compared with trigger efficiency for Monte Carlo events of the same $\Upsilon(2S)$ transition followed by $\Upsilon(1S)$ decays to noninteracting particles. The two trigger efficiencies agree within statistical error. For the two-photon collisions with $2\pi^+2\pi^-\pi^0$ in the final state, the systematic error of the trigger simulation is estimated to amount to 5% [22].

3.3 Experimental Resolution

For the partial wave analysis, it is essential to determine the experimental resolution of all quantities used as an argument of the decay matrix element. In the case of the five pion final state these are invariant masses of $\pi^+\pi^-$ and $\pi^+\pi^-\pi^0$ combinations as well as all polar angles used in the wave function $\Psi^{L\ j}_{J^P\ J_z}$ (eq. 1.41). The generated and measured values of these parameters are collected in vectors ζ and ζ', respectively. The difference between both vectors $\Delta\zeta$ is expected to be distributed normally

$$\rho(\Delta\zeta) = \frac{1}{(2\pi)^{K/2}}(detV)^{-1/2} \cdot exp\left[-\frac{1}{2}((\Delta\zeta - \overline{\Delta\zeta})^T V^{-1}(\Delta\zeta - \overline{\Delta\zeta})\right], \qquad (3.18)$$

where V is the covariance matrix and $\overline{\Delta\zeta}$ the bias of ζ'. K is the number of variables. Due to one-to-one correspondence between quantities that correspond to different pion permutations (eq. 1.56), we have to find only a covariance matrix for the quantities of one of the pion permutations. In this case, the number of variables K amounts to 8. The elements of the covariance matrix V are determined from simulation, where both values, generated and reconstructed, are known for all variables

$$V_{ij} = \frac{1}{N}\sum_{n=1}^{N}(\zeta'_i - \zeta_i)_n\ (\zeta'_j - \zeta_j)_n \quad - \quad \overline{\Delta\zeta_i} \cdot \overline{\Delta\zeta_j}. \qquad (3.19)$$

The summation is performed over all accepted simulated events. We have assumed the covariance matrix V to be constant inside the two-photon invariant mass intervals used

in our further analysis. Resolutions, i.e. square roots of the diagonal elements of V are listed in table 3.1.

Resolution σ							
$m_{\pi^+\pi^-}$ $[GeV]$	$m_{\pi^+\pi^-\pi^0}$ $[GeV]$	λ $[GeV^{-3}]$	$cos(\theta)$	$cos(\theta_n)$	$cos(\theta_\rho)$	$\phi - \phi_n$	$\phi - \phi_\rho$
0.010	0.024	0.0020	0.026	0.038	0.020	0.078	0.044

Table 3.1: Experimental resolution of quantities used in partial wave analysis of five pions final state for $W_{\gamma\gamma}$ interval between 1.4 and 1.8 GeV.

Chapter 4

Event Selection

4.1 Data selection for the $\pi^+\pi^-\pi^o\pi^+\pi^-$ final state

The data sample used for this analysis represents an integrated luminosity of 472.7 pb^{-1} at an average e^+e^- center-of-mass energy of 10.2 GeV. Since in interactions of two almost real photons both scattered leptons mostly escape detection, we require exactly four charge tracks pointing to the main vertex. The charged tracks have to be consistent with the pion mass hypothesis, i.e. their probabilities for being pions λ_π (eq. 2.9) should exceed 1%. We further reduce the probability of misintepretation of pions as electrons or muons by taking advantage of probabilities P_e and P_μ introduced in section 2.3. Both quantities are required to be less than 10 %.

The neutral pion is obtained as a two-photon combination, where photons are taken as showers in the calorimeter unconnected with any charged track from the drift chamber. For this we use only showers not recognized as calorimeter noise. To construct neutral pions we use also converted photons, obtained as e^+e^- pairs with invariant masses less than 30 MeV and opening angles between both leptons $cos\theta > 0.98$. Due to different energy resolution for converted photons and photons obtained from calorimeter showers, also requirements on the neutral pion invariant mass depend on the pion construction. The pair with both photons detected as unconnected showers is considered as neutral pion if the two-photon invariant mass lies between 70 MeV and 200 MeV. The maximum difference between pion nominal mass and invariant mass of pairs with one converted photon is 50 MeV and it is only 40 MeV for pairs with both photons converted.

Beside the selected four charged pions no other charged track is allowed to originate from a common vertex at the interaction point. Also neutral particles identified with a secondary vertex as K^0_s, Λ or converted photons which are not used for neutral pion selection, are not allowed in the events. But it is possible to find additional unconnected

showers due to noise or particle interactions in the calorimeter, although no real photon is expected beside the ones from the neutral pion.

Noise in the calorimeter can be classified in three categories: hot showers, low energy noise and high energy noise.

Hot showers are modules of the calorimeter, which in a certain period almost constantly respond as being hit. These periods are determined from unbiased measured data. A repetition of five hits in the same module, separated by not more than 10 events represent the minimal condition for a module to be considered as "hot". This criterion is found to be very safe. An average separation between two successive hits is less than four. In order to reduce the number of periods we combine them in a single one, if they are separated by less than 500 events.

The low energy noise is studied with randomly triggered events, where no showers in the calorimeter are expected due to real photons or charged particles. This data sample is used to obtain an upper limit of noise energy in each module. Values are determined so that the number of noise hits with energy above the chosen values are equal in all modules. The energy limits are calculated for several running periods. The length of each period depends on the number of randomly triggered events recorded during data taking. The allowed number of noise hits with energy above the obtained upper limits is $2 \cdot 10^{-5}$ hits per module per event.

In order to recognize the high energy noise in the calorimeter it is crucial that noisy modules are separated from each other and from other hit modules. It was found from studies on measured data with well identified photons that, for example, less than 5 % of all photons with energy between 350 and 360 MeV hit just one module. This fraction is even lower for photons with higher energy. Therefore, five pion events are selected despite additional unconnected showers with energy above 350 MeV and cluster size of one module. Such showers are, in contrary to hot showers and low energy noise, used for neutral pion construction.

Additional unconnected showers can also be produced by interactions of final state particles in the calorimeter. Such showers are called fake photons. In the neighbourhood of a charged particle shower further showers can appear due to "shower splitting". In the case of leptons this is mainly caused by dead modules at the particle impact point X_p or insufficient energy deposition in some modules. For hadrons, shower splitting can also appear due to charge exchange interactions, where neutrons and neutral pions are produced. So, unconnected showers due to shower splitting, are spread wider around hadron than around lepton impact points (fig. 4.1). This leads also to different criteria for fake photons connected to hadrons and fake photons connected to leptons. The cosine

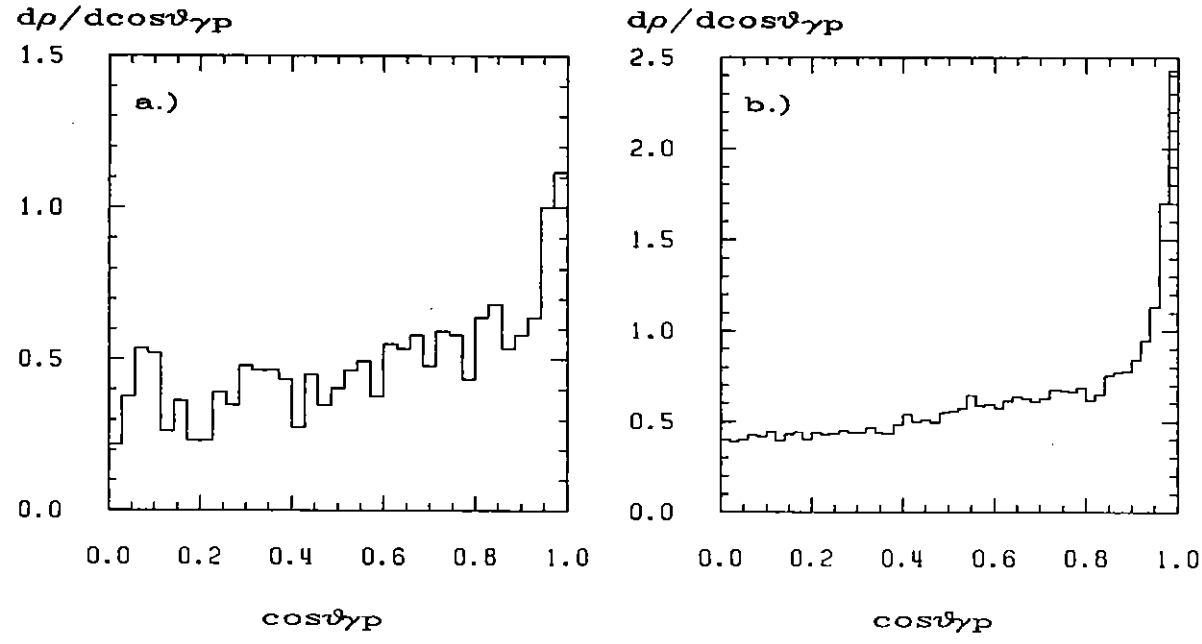

Figure 4.1: Distribution ($d\rho/dcos\theta_{\gamma p}$) of photons according to cosine of opening angle between photon momenta and impact point position of a) - electrons and b) - pions in the calorimeter. The distributions are obtained by Monte Carlo simulation.

of opening angle $cos\theta_{\gamma p}$ between unconnected shower and charge particle impact point X_p is therefore required to be greater than 0.9 for fake photons in the case of leptons and greater than 0.8 for hadrons. Due to a very broad region in the case of hadrons, we additionally require also that total energy E_{sh} deposited in this part of the calorimeter should not exceed the hadron energy E_p for more than 250 MeV

$$E_{sh} = (E_p)_{sh} + \sum_{cos\theta_{\gamma p}>0.8} E_\gamma < E_p + 250MeV , \qquad (4.1)$$

where $(E_p)_{sh}$ is the energy of the shower corresponding to charged hadron. The shift of 250 MeV is obtained from Monte Carlo studies of hadron behaviour in the calorimeter (fig. 4.2). By this criterion less than 0.1 % of simulated pions are lost.

Additional photons can appear in events also when neutral pions produced at interactions of charge hadrons in the calorimeter scatter back into the drift chamber. In order to recognize such photons we try to reconstruct neutral pions from photon pairs considering the charged hadron impact points as an origin of photon pairs. A two-photon invariant mass is required to lie between 90 and 180 MeV. The interval is narrower than the one used for the selected neutral pion because background coming from two-photon

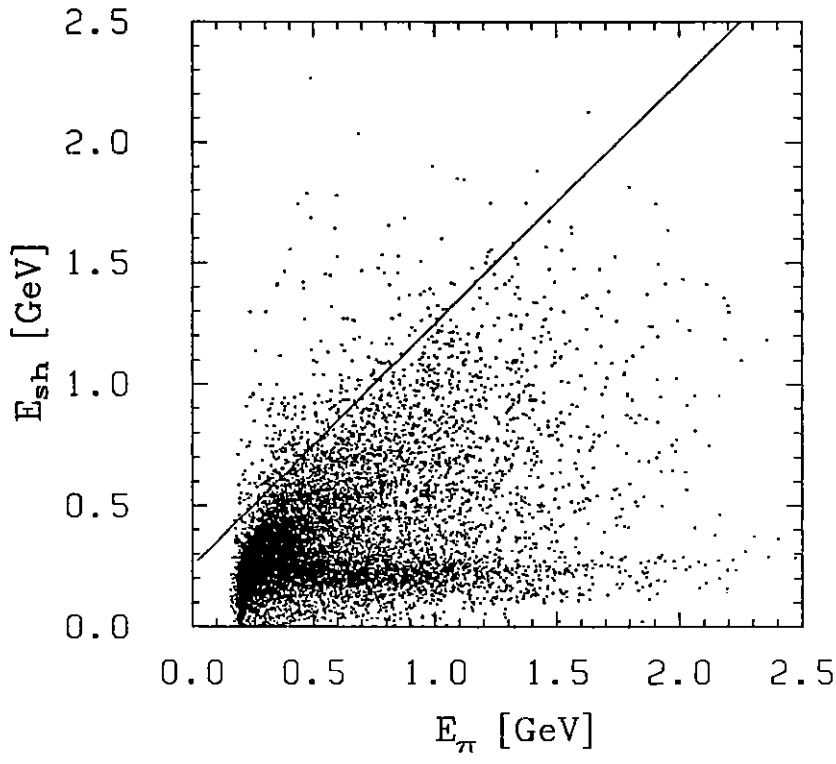

Figure 4.2: The correlation between pion energy E_π and deposited energy E_{sh} in the part of the calorimeter with cosine of opening angle around pion impact point greater than 0.8. The unconnected showers within this area are treated as fake photons only if the energy E_{sh} lies below the shown line. The correlation is obtained from simulation of the five pion final state in two-photon interactions.

interactions with more neutral pions in the final state should be kept low. The neutral pion energy E_{π^0} has to be smaller than undetected energy E_u at hadron impact point

$$E_{\pi^0} < E_u \equiv E_p - (E_p)_{sh} - \sum_{cos\theta_{\gamma p}>0.8} E_\gamma + 250MeV \tag{4.2}$$

even further reducing the background.

In interactions of hadrons in the calorimeter also neutrons can be scattered back into the detector volume. Unfortunately, neutron showers are hard to separate from photon showers and even harder from overlapped showers of photons coming from the same neutral pion. In order to identify neutrons, a lateral function f_{lat} [40]

$$f_{lat} = \frac{E_{lat}}{E_1 + E_2 + E_{lat}} \tag{4.3}$$

has to be introduced. E_1 and E_2 are the highest two energy deposited in the single module

of the studied shower, while E_{lat} labels the second moment

$$E_{lat} = \sum_{i=3}^{n} \frac{E_i \, r_i^2}{< \Delta r >^2} \quad , \tag{4.4}$$

where r_i is a distance of i-th module from the shower center-of-energy and $< \Delta r >$ is the average distance between two modules. In average, neutrons have higher lateral function than photons while their energy inside showers is distributed usually more uniformly than the energy of photons. In photon showers, most of the energy is deposited in modules along the photon line, so that the lateral function depends on polar angle of the photon momentum. Using measured data with well identified photons, an envelope $f_{lat}(max)$, determined by requiring that 95 % of all photons have a lower value of lateral function, is found as a function of polar angle [41] (table 4.1). Values $f_{lat}(max)$ from table 4.1

ring number	1	2	3	4	5	6	7	8
$f_{lat}(max)[\%]$	21	21	21	23	29	35	40	44

9	10	11	12	13	14	15
40	25	55	58	54	43	38

Table 4.1: The envelope value $f_{lat}(max)$, given as a function of calorimeter ring number N_R. In both hemispheres ring numbers increase from a detector equator $N_R = 1$ towards the beam tube $N_R = 15$.

are used as a lower boundary for lateral functions of unconnected showers recognized as neutrons. In addition, a total shower energy E_n of a neutron candidate should not exceed the maximal undetected energy E_u in the event

$$E_n < \max_{i=1,4} \{ (E_u)_i \} - 200 \; MeV \tag{4.5}$$

where i runs over all charged pions. An energy shift of $-200 \; MeV$ is obtained from a simulation with neutrons in the final state applying the same method as for the shift at charged pions (fig. 4.2). Only in some energy regions it is possible to separate neutrons from overlapped showers of photons coming from the same neutral pion. The majority of neutral pions with energy between 1.5 GeV and 2.5 GeV produce showers with lateral function above the values listed in table 4.1 [41]. Since there is no other way to distinguish these showers from showers of neutrons, the neutron candidates from the above energy region are not treated as fake photons.

In the analysis we use three kinematic criteria. The first criterion is the already mentioned cut on two-photon transverse momentum p_T (section 1.1). We require the total transverse momentum of all five selected pions to be smaller than $p_T < 60$MeV. The

second criterion is derived from momentum conservation of all particles involved in the studied reaction, including undetected leptons. Since incoming electron and positron have opposite momenta (fig. 1.1), particles produced at studied interaction $e^+e^- \rightarrow e^+e^-5\pi$ have a vanishing total momentum and energy equal to e^+e^- center-of-mass energy $E_{e^+e^-} = 2 \cdot E_B$, so that the four-vector of the system amounts to $p_{e^+e^-} = (\vec{0}, E_{e^+e^-})$. In the no-tag analysis only particles of two-photon final state are observed, while electron and positron scatter along the beam tube and escape detection. Therefore, a polar angle $\theta_{e^\pm}$ between scattered lepton and the beam axis lies within an interval of cosine $|cos\theta_{e^\pm}| \geq 0.92$, where charged particles cannot be detected. To recognize selected five pions as two-photon final state particles, their four-momentum $p_{5\pi} = (\vec{p}_{5\pi}, E_{5\pi})$ is required to sum up into the four-vector $(\vec{0}, E_{e^+e^-})$ with four-momentum of at least one lepton pair, where both leptons are scattered within the above interval of polar angle[1]. In order to reduce the background coming from two-photon reactions $\gamma\gamma \rightarrow \pi^+\pi^-\pi^+\pi^-$ with low total transverse momentum we require the transverse momentum of all selected charged particles to exceed 20 MeV/c.

After applying these selection criteria a sample of 2717 events remains, out of which 2547 lie in the studied region of invariant mass between 1.0 and 3.5 GeV/c^2 (fig. 4.3).

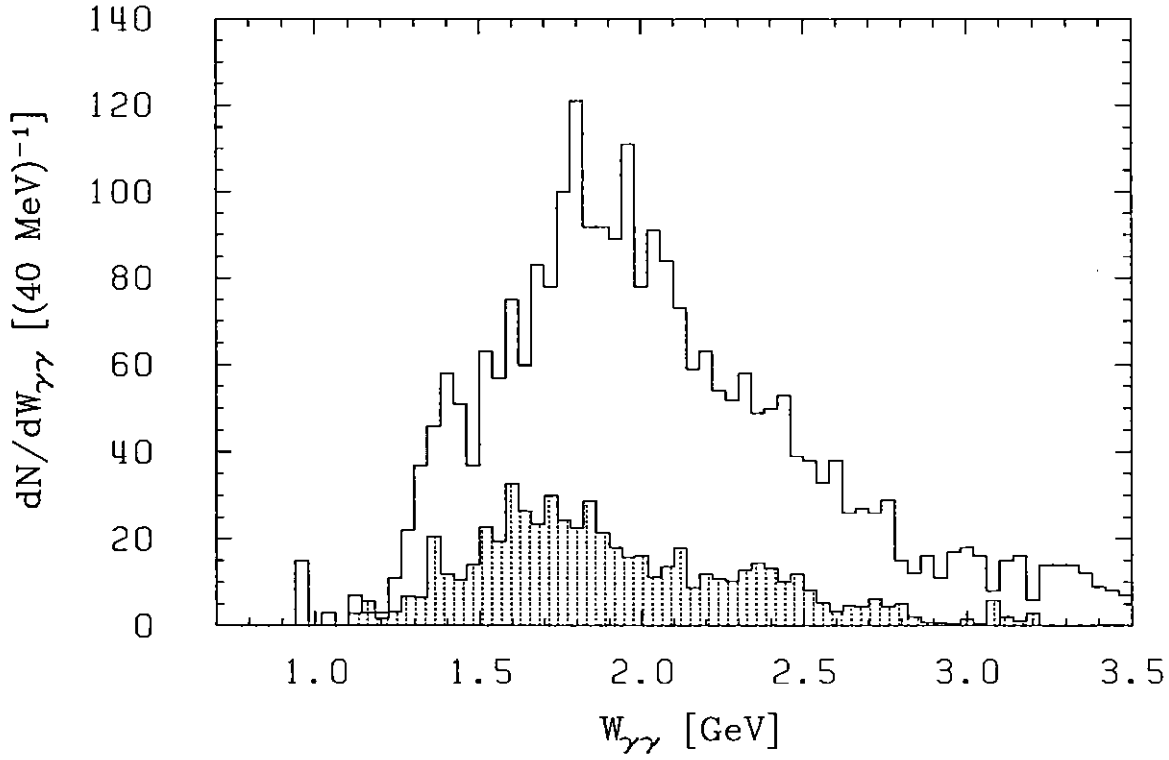

Figure 4.3: Invariant mass distribution of accepted $\pi^+\pi^-\pi^0\pi^+\pi^-$ events. Dotted histogram shows estimated background for this data sample.

[1]This criterion is particularly useful for studies of interactions of two virtual photons.

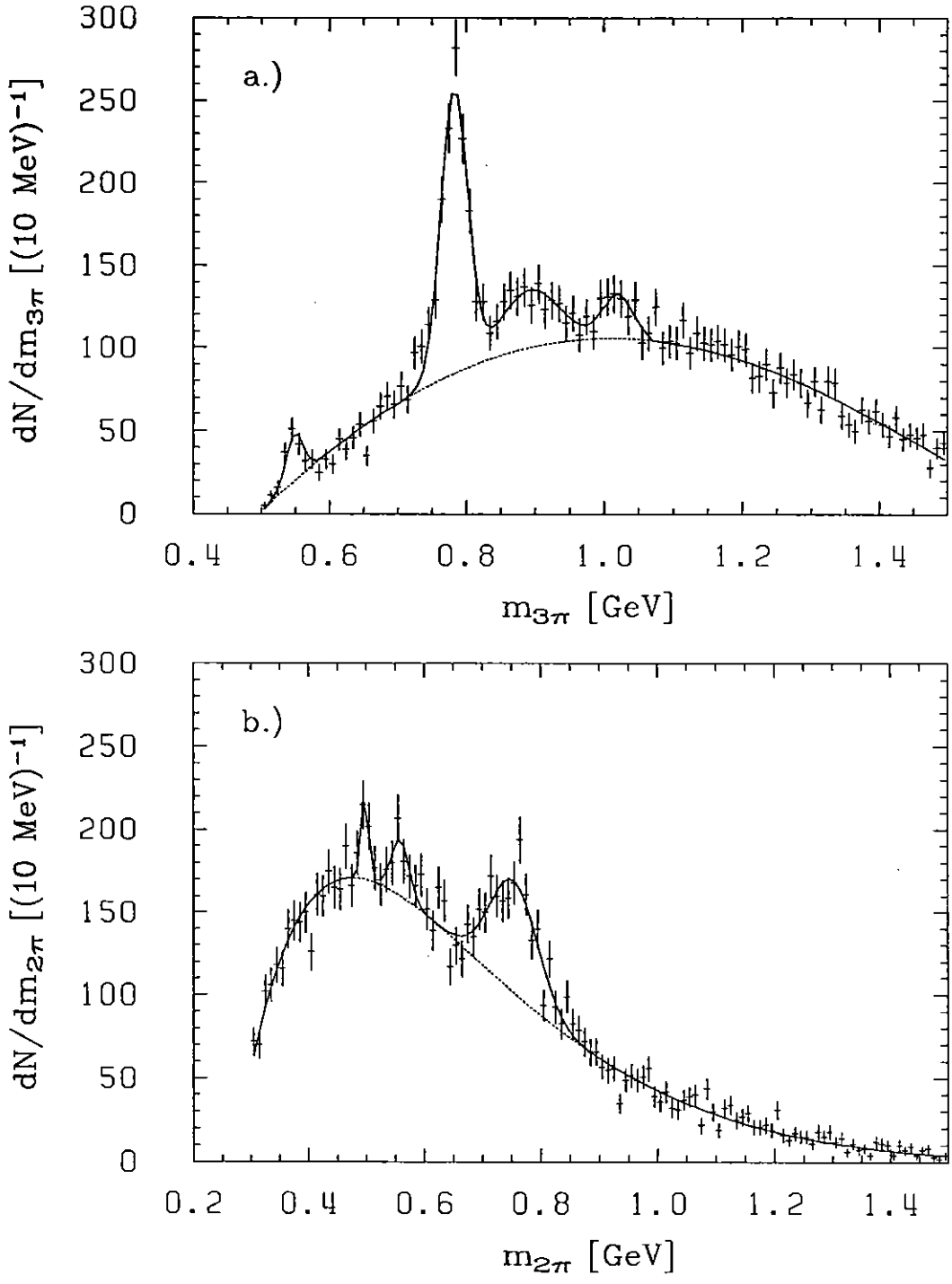

Figure 4.4: a.) $\pi^+\pi^-\pi^0$ and b.) $\pi^+\pi^-$ invariant mass distribution of accepted $\pi^+\pi^-\pi^0\pi^+\pi^-$ events with invariant mass between 1.0 and 3.5 GeV/c^2.

For the subsample of 2547 events distributions of $\pi^+\pi^-\pi^0$ and $\pi^+\pi^-$ invariant masses are shown in fig. 4.4. Due to permutations of like-sign pions, each event contributes at least four entries to each histogram presenting the above distributions. In spite of that, clear signals can be seen at ω and ρ^0 masses in distributions of $\pi^+\pi^-\pi^0$ and $\pi^+\pi^-$ invariant masses, respectively.

4.2 Background Estimation for the $\pi^+\pi^-\pi^0\pi^+\pi^-$ selected sample

The main source of background are other two-photon interactions with incompletely reconstructed events or missidentified particles. In order to estimate their contribution to selected $\pi^+\pi^-\pi^0\pi^+\pi^-$ events, we developed a program that simulates the major part of known two-photon interactions. The e^+e^- scattering process is simulated with respect to the luminosity function as it is described in section 3.1. Particles produced in the two-photon reactions are generated isotropically in two-photon center-of-mass system while the frequency of particular reaction $\gamma\gamma \to X_i$ depends on its cross section $\sigma_{\gamma\gamma\to X_i}(W_{\gamma\gamma})$. Values of the cross sections are taken from already published measurements. The event generator is followed by the detector simulation, event reconstruction, and trigger simulation (section 3.2). Since noise in the calorimeter is not included in the detector simulation, it is added from measured data triggered by the COSMIC test trigger. In these events fake photons can appear only at the muon impact points due to shower splitting. Removing showers with cosine of the opening angle between their center-of-energy and muon impact points greater than $cos_{\gamma\mu} > 0.9$, we are left with showers resulting from calorimeter noise. So selected noisy showers are added to the simulated events on an event by event basis. Scaling the number of simulated events to the luminosity of the measured data sample used for the $\pi^+\pi^-\pi^0\pi^+\pi^-$ analysis, we estimate the background from other two-photon reactions to be 601 events in the $\gamma\gamma$ invariant mass region between 1.0 and 3.5 GeV.

Background from τ decays is estimated in the same way using Monte Carlo simulated $e^+e^- \to \tau^+\tau^-$ events [42]. Scaling the number of τ events to the above luminosity, only 3 events fulfill the same selection criteria as they are used in $\pi^+\pi^-\pi^0\pi^+\pi^-$ analysis. Background due to incompletely reconstructed events $e^+e^- \to$ hadrons is in a similar way estimated to be 16 events.

Also beam gas reactions can fulfill the $\pi^+\pi^-\pi^0\pi^+\pi^-$ selection criteria. Their contribution to the selected events is estimated using the selected events themselves. Detected beam gas reactions are in the vicinity of the interaction point distributed along the beam fairly uniformly, while particles produced at two-photon reactions mainly originate from

background reaction	number of events $1.0 \leq W_{\gamma\gamma} \leq 3.5\text{GeV/c}^2$
$\gamma\gamma \to \omega\pi^+\pi^0\pi^-$	217
$\gamma\gamma \to \pi^+\pi^+\pi^0\pi^0\pi^-\pi^-$	181
$\gamma\gamma \to X_{\text{others}}$	203
$\gamma\gamma \to X_{\text{all}}$	601
$e^+e^- \to \tau^+\tau^-$	3
$e^+e^- \to$ hadrons	16
beam gas	18

Table 4.2: Background contributions in the $\pi^+\pi^-\pi^0\pi^+\pi^-$ sample.

the interaction point. So, the measured distribution of the common vertex position along the z-axis is fitted by a sum of the Gaussian function describing the studied reaction, and a constant. From the fitted value of the constant we have estimated the background due to the beam gas reactions, to be less than 18 events. All contributions of background to the selected data are collected in table 4.2 while the distribution of background with respect to $\gamma\gamma$ invariant mass is shown in fig. 4.3.

Chapter 5

The Analysis of the $\pi^+\pi^+\pi^0\pi^-\pi^-$ Final State

5.1 Maximum Likelihood Method

The maximum likelihood method is applied in the analysis of the five pion final state, because it is the most efficient method to determine the unknown parameters from experiments involving only a small number of events. The data are used in the form of complete events. So, there is no need to project experimental data on a binned multidimensional histogram. It also turns out that for the analysis with maximum likelihood method only acceptances averaged over all kinematic quantities are needed.

In order to perform the maximum likelihood method on the five pion final state, we have to calculate the probability distribution of measured events as a function of momenta of all particles produced in a two-photon interaction. Combining the expression of the cross section $\sigma_{ee\to ee5\pi}$ for two-photon production of five pions, detector efficiency and integrated e^+e^- luminosity L_{ee}, we arrive at the distribution of measured events

$$\frac{dN}{dW_{\gamma\gamma}d\zeta} = L_{ee}\,\frac{d\sigma_{ee\to ee5\pi}}{d\zeta}\,\eta(\zeta) = L_{ee}\,\frac{dL\gamma\gamma}{dW_{\gamma\gamma}}\,\frac{d\sigma_{\gamma\gamma\to 5\pi}}{d\zeta}\,\eta(\zeta)\,. \tag{5.1}$$

The distribution is normalized to a total number of observed events N. Vector ζ includes all kinematic variables used to describe the decay matrix element D from eq. 1.56 for a fixed $W_{\gamma\gamma}$. Certainly, acceptance $\eta(\zeta)$, the cross section $d\sigma_{\gamma\gamma\to 5\pi}/d\zeta$ and the luminosity function $dL_{\gamma\gamma}/dW_{\gamma\gamma}$ depend also on two-photon invariant mass $W_{\gamma\gamma}$ as well as on unmeasured independent quantities ξ related to scattered electron and positron. Since the maximum likelihood method is applied in each $W_{\gamma\gamma}$ bin separately, we determine these three quantities by averaging over all variables except ζ inside each $W_{\gamma\gamma}$ bin. For fixed $W_{\gamma\gamma}$, the differential cross section $d\sigma_{\gamma\gamma\to 5\pi}/d\zeta$ is expressed as a sum over all decay channels

k, r with decay matrix elements D_k and D_r and unknown parameters A_k

$$\frac{d\sigma_{\gamma\gamma\to 5\pi}}{d\zeta} = \sum_{k,r} A_k\, D_k^*(\zeta)\, P_{k,r}\, A_r\, D_r(\zeta) \ . \tag{5.2}$$

The summation includes also interference terms with $k \neq r$, where phase shifts $e^{i\delta_{kr}}$ are stored as off-diagonal elements of Hermitian matrix P. The selection rules in two-photon production of $\omega\rho$ allow only interferences between channels $(J^P, J_z, S) = (2^-, 0, 1)$, $(2^-, 0, 2)$, $(0^-, 0, 1)$ and between channels $(J^P, J_z) = (2^+, 0)$ and $(0^+, 0)$. The only non-zero off-diagonal elements are between channels of these two groups. Diagonal elements of matrix P are equal to one.

It is worth noting that instead of trying to subtract contributions of $\omega 2\pi$, $\rho 3\pi$ and isotropic 5π production from selected data, we rather include them in the summation (eq. 5.2) as incoherent contributions.

Using the averaged decay matrix elements

$$|D_k|^2 = \int D_k^*(\zeta)\, D_k(\zeta)\, d\zeta \ , \tag{5.3}$$

the relation 5.2 transforms to

$$\frac{d\sigma_{\gamma\gamma\to 5\pi}}{d\zeta} = \sum_{k,r} \tilde{A}_k\, \hat{D}_k^*(\zeta)\, P_{k,r}\, \tilde{A}_r\, \hat{D}_r(\zeta) \ , \tag{5.4}$$

with redefined unknown parameters $\tilde{A}_k = A_k \cdot |D_k|$ and normalized decay matrix elements $\hat{D}_k(\zeta) = D_k(\zeta)/|D_k|$. Due to orthonormality of decay matrix elements $\hat{D}_k$, the integration of the relation above leads to

$$\sigma_{\gamma\gamma\to 5\pi} = \sum_k \tilde{A}_k \cdot \tilde{A}_k \ , \tag{5.5}$$

where $\tilde{A}_k^2$ is the cross section of channel k. This suggests an introduction of unknown parameters as ratios between square roots of cross sections

$$\lambda_k = \frac{\tilde{A}_k}{\sqrt{\sigma_{\gamma\gamma\to 5\pi}}} \ , \tag{5.6}$$

with the condition

$$\sum_k \lambda_k^2 = 1 \ . \tag{5.7}$$

With this new notation the distribution from eq. 5.1 becomes equal to

$$\frac{d^2N}{dW_{\gamma\gamma}d\zeta} = L_{ee}\, \frac{dL\gamma\gamma}{dW_{\gamma\gamma}}\, \sigma_{\gamma\gamma\to 5\pi}\eta(\zeta) \cdot \left[\sum_k \lambda_k^2\, \hat{D}_k^*(\zeta)\, \hat{D}_k(\zeta) + \sum_{\substack{k,r \\ k>r}} \lambda_k\lambda_r\, cos(\delta_{kr}) \left(\hat{D}_k^*(\zeta)\, \hat{D}_r(\zeta) + \hat{D}_r^*(\zeta)\, \hat{D}_k(\zeta)\right)\right] \ , \tag{5.8}$$

where interference terms are separately written. The normalization of distribution $\frac{d^2N}{dW_{\gamma\gamma}d\zeta}$ is obtained from the integration

$$\frac{dN}{dW_{\gamma\gamma}} = \int \frac{d^2N}{dW_{\gamma\gamma}d\zeta}d\zeta = L_{ee}\frac{dL\gamma\gamma}{dW_{\gamma\gamma}}\sigma_{\gamma\gamma\to 5\pi}\left[\sum_k \lambda_k^2\eta_k + 2\sum_{\substack{k,r\\k>r}}\lambda_k\lambda_r\, cos(\delta_{kr})\,\eta_{kr}\right], \quad (5.9)$$

where

$$\eta_k = \frac{\int \eta(\xi,\zeta)\,\frac{d^2L}{dW_{\gamma\gamma}d\xi}\,\hat{D}_k^*(\zeta)\hat{D}_k(\zeta)\,d\xi d\zeta}{\int \frac{d^2L}{dW_{\gamma\gamma}d\xi}d\xi} \quad (5.10)$$

is the average detector acceptance for channel k, given as a function of $W_{\gamma\gamma}$. Similarly can also

$$\eta_{kr} = \frac{1}{\frac{dL}{dW_{\gamma\gamma}}}\cdot\int \eta(\xi,\zeta)\,\frac{d^2L}{dW_{\gamma\gamma}d\xi}\,\frac{(\hat{D}_k^*(\zeta)\hat{D}_r(\zeta)+\hat{D}_r^*(\zeta)\hat{D}_k(\zeta))}{2}\,d\xi d\zeta \quad (5.11)$$

be interpreted as an average acceptance for the interference term of channels k and r. In relations 5.10 and 5.11 the dependence of acceptance and of the luminosity function on unmeasured quantities ξ is explicitly written. $dN/dW_{\gamma\gamma}$ is the number of all observed events in a given $W_{\gamma\gamma}$ bin. Due to experimental resolution of the detector, the exact values of kinematic variables ζ needed for calculation of the distribution 5.8, have to be replaced by measured values ζ'. In order to use values ζ', also products of decay matrix elements $\hat{D}_k^*(\zeta)\hat{D}_r(\zeta)$ have to be substituted by a convolution

$$\overline{\hat{D}}_{kr}(\zeta') = \frac{1}{N_T}\sum_{i=1}^{N_T}\left|\hat{D}_k^*(\zeta'-\Delta\zeta_i)\hat{D}_r(\zeta'-\Delta\zeta_i)\right|, \quad (5.12)$$

where $\Delta\zeta_i$ are normally distributed according to relation 3.18, and N_T is the number of tries.

Now we can write the likelihood function L from the probability density function

$$g(\zeta',\vec{\lambda},\vec{\delta}) = \frac{1}{N}\frac{dN}{d\zeta} = \eta(\zeta')\cdot\frac{\sum_k \lambda_k^2\,\overline{\hat{D}}_{kk}(\zeta') + \sum_{k\neq r}\lambda_k\lambda_r cos(\delta_{kr})\,\overline{\hat{D}}_{kr}(\zeta')}{\sum_k\lambda_k^2\eta_k + 2\sum_{k>r}\lambda_k\lambda_r\, cos(\delta_{kr})\,\eta_{kr}} \quad (5.13)$$

as a product of $g(\zeta_i',\vec{\lambda},\vec{\delta})$ for all our selected events i [43]

$$L(\vec{\lambda},\vec{\delta}) = \prod_{i=1}^{N} g(\zeta_i',\vec{\lambda},\vec{\delta}). \quad (5.14)$$

Usually, it is convenient to consider the logarithm of the likelihood function

$$\mathcal{L}'(\vec{\lambda},\vec{\delta}) = lnL(\vec{\lambda},\vec{\delta}) = \sum_{i=1}^{N} ln\; g(\zeta_i',\vec{\lambda},\vec{\delta}). \quad (5.15)$$

As it is seen from relation 5.13, the likelihood function $\mathcal{L}'$ is invariant under simultaneous multiplication of all parameters λ_k. This reduces the efficiency of MINUIT program [44] used to find the function maximum, so we redefine the likelihood function to

$$\begin{aligned}\mathcal{L}(\vec{\lambda},\vec{\delta}) &= \sum_{i=1}^{N} ln\Big[\sum_k \lambda_k^2\, \overline{\hat{D}}_{kk}(\zeta') + \sum_{k\neq r}\lambda_k\lambda_r cos(\delta_{kr})\, \overline{\hat{D}}_{kr}(\zeta')\Big] \\ &- N\Big[\sum_k \lambda_k^2\eta_k + 2\sum_{k>r}\lambda_k\lambda_r\, cos(\delta_{kr})\,\eta_{kr}\Big] \end{aligned} \tag{5.16}$$

which conserves the ratios between parameters λ_k. The second summation in the above relation represents a constraint that number of fitted events coincide with number of measured events. The factor N in front of the sum is analytically calculated Lagrange multiplier [45, 43]. The most probable values of $\vec{\lambda}$ and $\vec{\delta}$ are obtained by maximizing the function $\mathcal{L}$. Since the acceptance $\eta(\zeta')$ depends only on kinematic quantities ζ', it is equal for all decay channels k. So, the position of maximum can be found although the precise value of acceptance $\eta(\zeta')$ as a function of kinematic variables ζ' is not known, only the value of the likelihood function itself depends on $\eta(\zeta')$.

Due to small number of measured events, several local maxima can appear in the likelihood function. This can certainly mislead the program, searching for an absolute maximum. To minimize this effect, $W_{\gamma\gamma}$ bins are chosen wide enough to contain a reasonable number of events. Once the fractions λ_k and phase shifts δ_{kr} are obtained, the cross section $\sigma_{\gamma\gamma\to 5\pi}$ is calculated from relation 5.9

$$\sigma_{\gamma\gamma\to 5\pi} = \frac{\frac{dN}{dW_{\gamma\gamma}}}{L_{ee}\,\frac{dL_{\gamma\gamma}}{dW_{\gamma\gamma}}}\cdot\left[\sum_k \lambda_k^2\eta_k + 2\sum_{\substack{k,r\\ k>r}}\lambda_k\lambda_r\, cos(\delta_{kr})\,\eta_{kr}\right]^{-1}, \tag{5.17}$$

while cross sections for particular decay channels are given as

$$\sigma_k = \sigma_{\gamma\gamma\to 5\pi}\cdot\lambda_k^2\,. \tag{5.18}$$

For all $\omega\rho^0$ channels the cross sections have to include also branching ratios $\mathrm{Br}(\omega\to 3\pi)$ and $\mathrm{Br}(\rho\to 2\pi)$ for the $\omega\to\pi^+\pi^-\pi^0$ and $\rho^0\to\pi^+\pi^-$ decays

$$\sigma_k(\gamma\gamma\to\omega\rho^0) = \frac{\sigma_{\gamma\gamma\to 5\pi}\cdot\lambda_k^2}{\mathrm{Br}(\omega\to 3\pi)\cdot\mathrm{Br}(\rho\to 2\pi)}\,, \tag{5.19}$$

while cross sections of reactions $\gamma\gamma\to\omega\pi^+\pi^-$ and $\gamma\gamma\to\rho^0\pi^+\pi^-\pi^0$ are determined by using relations

$$\sigma(\gamma\gamma\to\omega\pi^+\pi^-) = \frac{\sigma_{\gamma\gamma\to 5\pi}\cdot\lambda_{\omega 2\pi}^2}{\mathrm{Br}(\omega\to 3\pi)}\,, \qquad \sigma(\gamma\gamma\to\rho^0\pi^+\pi^-\pi^0) = \frac{\sigma_{\gamma\gamma\to 5\pi}\cdot\lambda_{\rho 3\pi}^2}{\mathrm{Br}(\rho\to 2\pi)}\,. \tag{5.20}$$

5.2 The Acceptance Calculation

The acceptance η is mainly studied by Monte Carlo simulation described in section 3.2. With simulated events it is possible to determine the detector and trigger efficiencies and the efficiencies of most selection criteria. The exceptions are studies of fake photons, which require also description of noise in the calorimeter. Since this is not included in the simulation, we add the calorimeter noise from measured data triggered by the COSMIC test trigger. The procedure is exactly the same as the one described in the case of background studies (section 4.2).

A proper description of fake photons in the simulation has been checked by analyzing measured data of cascade decay [46]

$$\begin{aligned} \Upsilon(2S) &\rightarrow \Upsilon(1S)\ \pi^+\,\pi^- \\ &\Upsilon(1S) \rightarrow e^+\,e^- \text{ or } \mu^+\,\mu^- , \end{aligned} \tag{5.21}$$

where no real photons are expected in the event. It is found that photon contribution predicted by hadronic interactions inside the calorimeter used in Monte Carlo simulation properly describe the measured photon contribution in $\Upsilon(2S)$ cascade decay.

Fortunately, only an acceptance averaged over kinematic quantities ζ is needed in our analysis (section 5.1). The average acceptance η_k depends on the decay channel k. To determine η_k we have used generated events of channel k with added calorimeter noise. Performing the complete event selection on the generated events, the acceptance is obtained as a ratio between accepted N_A and generated N_G events in each $W_{\gamma\gamma}$ bin. The acceptances η_k for various spin-parities of $\omega\rho$ production are collected in fig. 5.1, while acceptances for isotropic $\omega\rho$, $\omega\pi^+\pi^-$, $\rho\pi^+\pi^-\pi^0$ and $\pi^+\pi^+\pi^0\pi^-\pi^-$ channels are shown in fig. 5.2. To lower the statistical error on acceptances, we use in the analysis results of the fit shown in both figures as solid line curves.

An acceptance averaged over kinematical quantities ζ is introduced also for the interference between two decay channels k and r (eq. 5.11). This acceptance η_{kr} is calculated using Monte Carlo events where the decay of two-photon intermediate state is generated according to interference term

$$D_k^*\,D_r \;+\; D_r^*\,D_k \;. \tag{5.22}$$

The sample of events is divided into two parts with different signs of interference term. For each part we calculate a ratio between number of events passing the whole events selection N_A^i and all generated events N_G^i. Index i denote the sign of interference term.

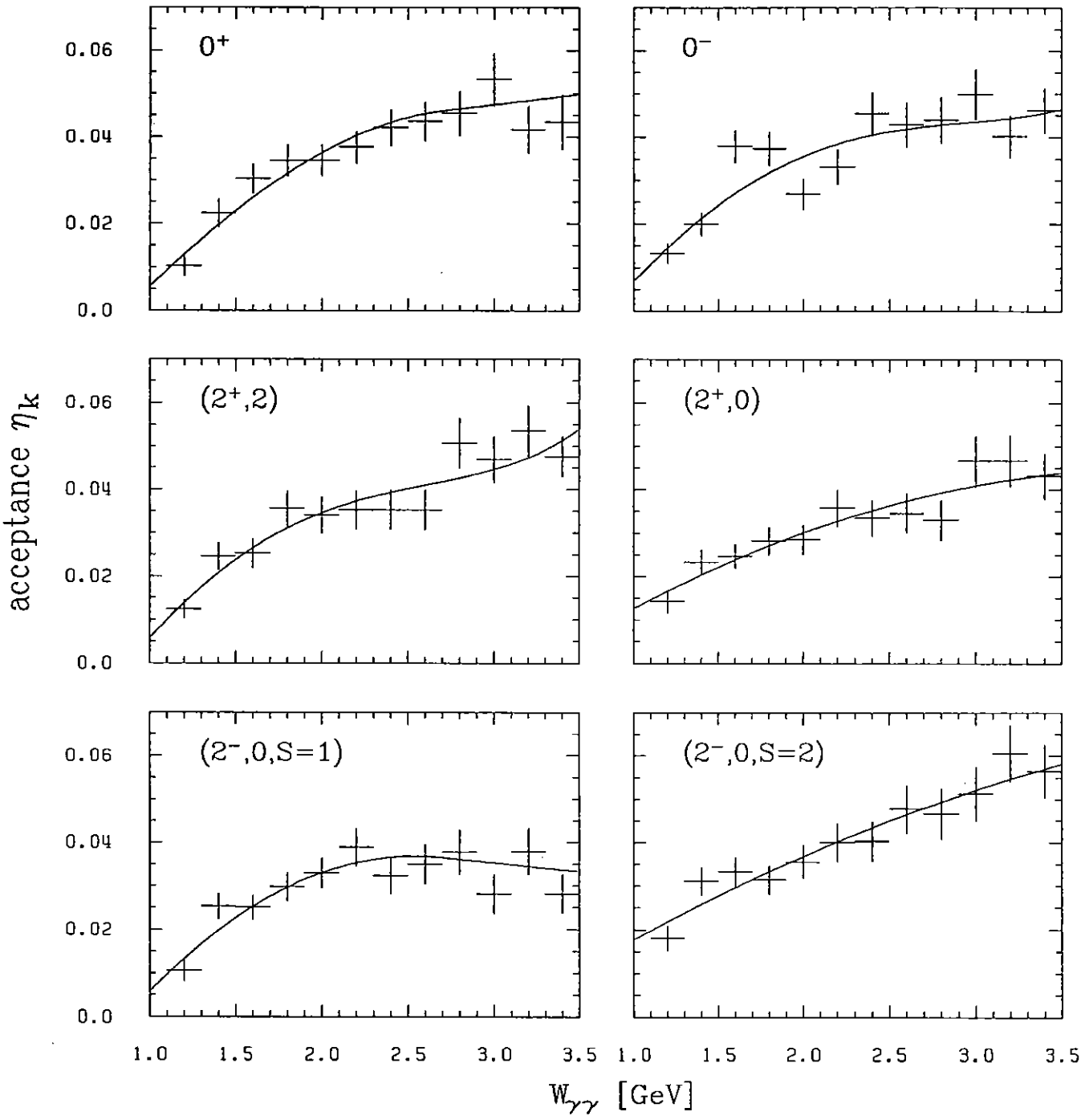

Figure 5.1: Acceptances η_k for all spin-parity (J^P, J_z) states of $\omega\rho$ (crosses) and fitted curves (solid lines).

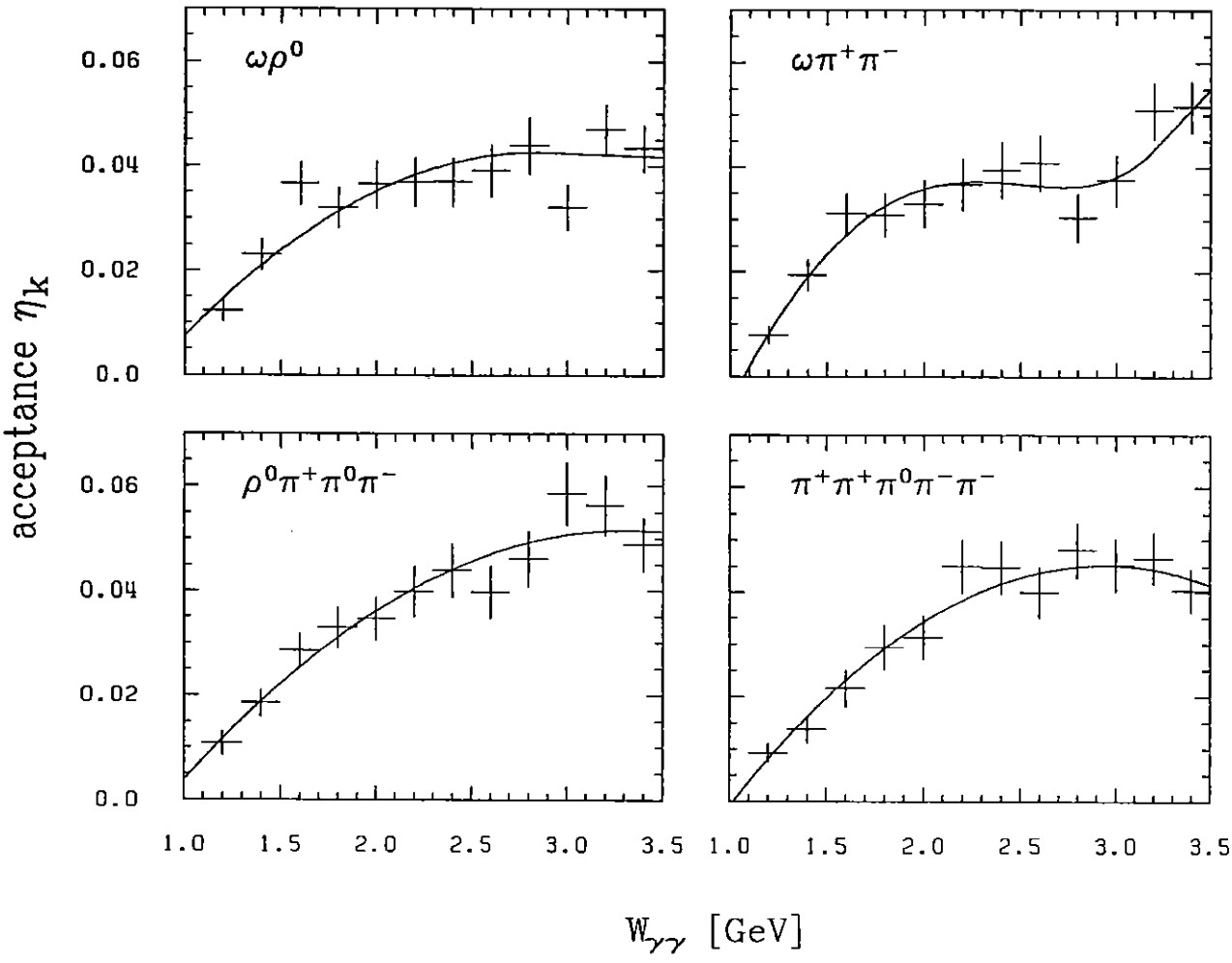

Figure 5.2: Acceptances for isotropic channels $\omega\rho$, $\omega\pi^+\pi^-$, $\rho\pi^+\pi^-\pi^0$, and $\pi^+\pi^+\pi^0\pi^-\pi^-$ (crosses) and fitted curves (solid lines).

The average acceptance η_{kr} is than obtained as a difference

$$\eta_{kr} = \frac{N_A^+}{N_G^+} - \frac{N_A^-}{N_G^-} \tag{5.23}$$

In fig. 5.3 are shown ratio of average acceptances $\eta_{kr}/\sqrt{\eta_k\eta_r}$ for all possible interferences in study of $\omega\rho^0$ production in two-photon interactions.

There are two sources of systematic errors on the acceptances. The systematic error coming from the detector simulation is estimated to be 6% [34]. As already discussed (section 3.2) the systematic error on trigger simulation amounts to 5% [22]. We estimate the overall error on acceptances η_k and η_{kr}, shown in figs. 5.1, 5.2, and 5.3 as error bars, by adding in quadrature the statistical error, the systematic error coming from the detector simulation, and the systematical error from trigger simulation.

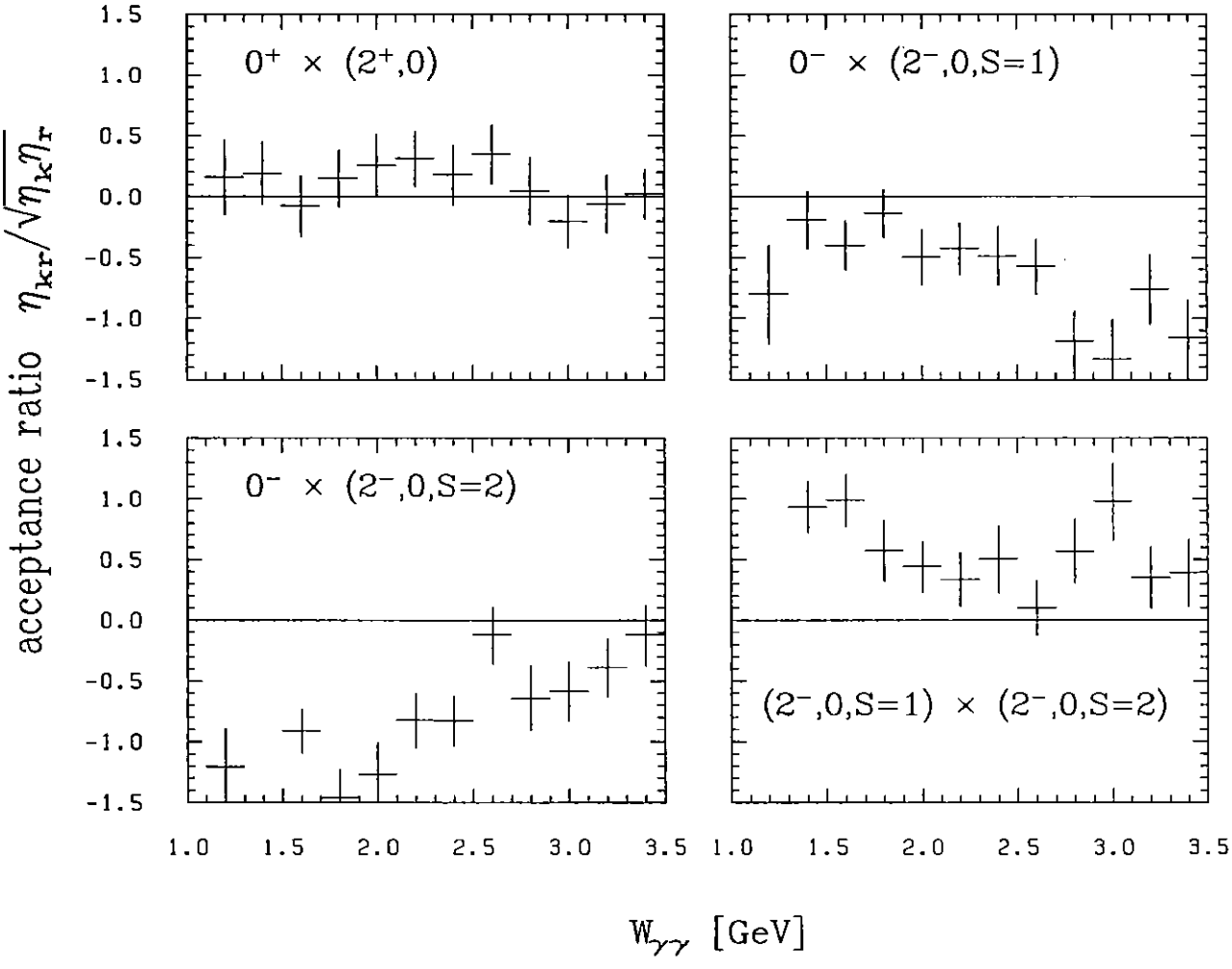

Figure 5.3: Ratio of acceptances $\eta_{kr}/\sqrt{\eta_k\eta_r}$ for all possible interferences between $\omega\rho^0$ channels:
$(J^P, J_z) = (0^+, 0)$ and $(2^+, 0)$
$(J^P, J_z, S) = (0^-, 0, 1)$ and $(2^-, 0, 1)$
$(J^P, J_z, S) = (0^-, 0, 1)$ and $(2^-, 0, 2)$
$(J^P, J_z, S) = (2^-, 0, 1)$ and $(2^-, 0, 2)$

Chapter 6

Results of the $\pi^+\pi^+\pi^0\pi^-\pi^-$ Analysis

The selected sample of five pions has been analyzed in two ways. In the first analysis we determine the cross sections of the two-photon reactions $\gamma\gamma \to \omega\rho^0$, $\gamma\gamma \to \omega\pi^+\pi^-$, $\gamma\gamma \to \rho^0\pi^+\pi^0\pi^-$, and $\gamma\gamma \to \pi^+\pi^+\pi^0\pi^-\pi^-$. In all reactions five pions are assumed to be isotropically distributed in two-photon center-of-mass system. Therefore, the reactions can be distinguished only by invariant-mass distributions. In the second analysis we try to determine also a spin-parity structure of the reaction $\gamma\gamma \to \omega\rho^0$. The $\omega\rho^0$ production includes six contributions of different spin-parities. To determine all cross sections including cross sections of reactions $\gamma\gamma \to \omega\pi^+\pi^-$, $\gamma\gamma \to \rho^0\pi^+\pi^0\pi^-$, and $\gamma\gamma \to \pi^+\pi^+\pi^0\pi^-\pi^-$ we apply a nine parameter fit.

6.1 Results of a Fit to Invariant-Mass Distributions

In order to determine the cross sections of reactions $\gamma\gamma \to \omega\rho^0$ $\gamma\gamma \to \omega\pi^+\pi^-$, $\gamma\gamma \to \rho^0\pi^+\pi^0\pi^-$, and $\gamma\gamma \to \pi^+\pi^+\pi^0\pi^-\pi^-$ a four parameter fit is applied. In reaction $\gamma\gamma \to \pi^+\pi^+\pi^0\pi^-\pi^-$ the final state particles are uniformly distributed in phase space. The fit procedure is performed in 12 bins, covering the $W_{\gamma\gamma}$ interval between 1.1 and 3.5 GeV. A distribution of the selected events within this interval is shown in fig. 6.1. The observed $\pi^+\pi^+\pi^0\pi^-\pi^-$ final state is assumed to be an incoherent sum of the upper four reactions. In the reaction $\gamma\gamma \to \omega\rho^0$ a production of final state hadrons is described by a decay matrix element

$$D^{iso}_{\omega\rho} = \sum_{i=1}^{4} \left(\mathcal{A}^{\omega}_{BW} \mathcal{A}^{\rho}_{BW} \right)_{P_i(\pi_1^+\pi_2^-\pi^0\pi_3^+\pi_4^-)} \tag{6.1}$$

where $\mathcal{A}^{\omega}_{BW}$ and $\mathcal{A}^{\rho}_{BW}$ are Breit-Wigner amplitudes for ω and ρ^0 mesons, respectively. The decay matrix elements used for description of reactions $\gamma\gamma \to \omega\pi^+\pi^-$, $\gamma\gamma \to \rho^0\pi^+\pi^0\pi^-$, and $\gamma\gamma \to \pi^+\pi^+\pi^0\pi^-\pi^-$ have already been introduced in chapter 1 eqs. 1.57, 1.58, 1.59,

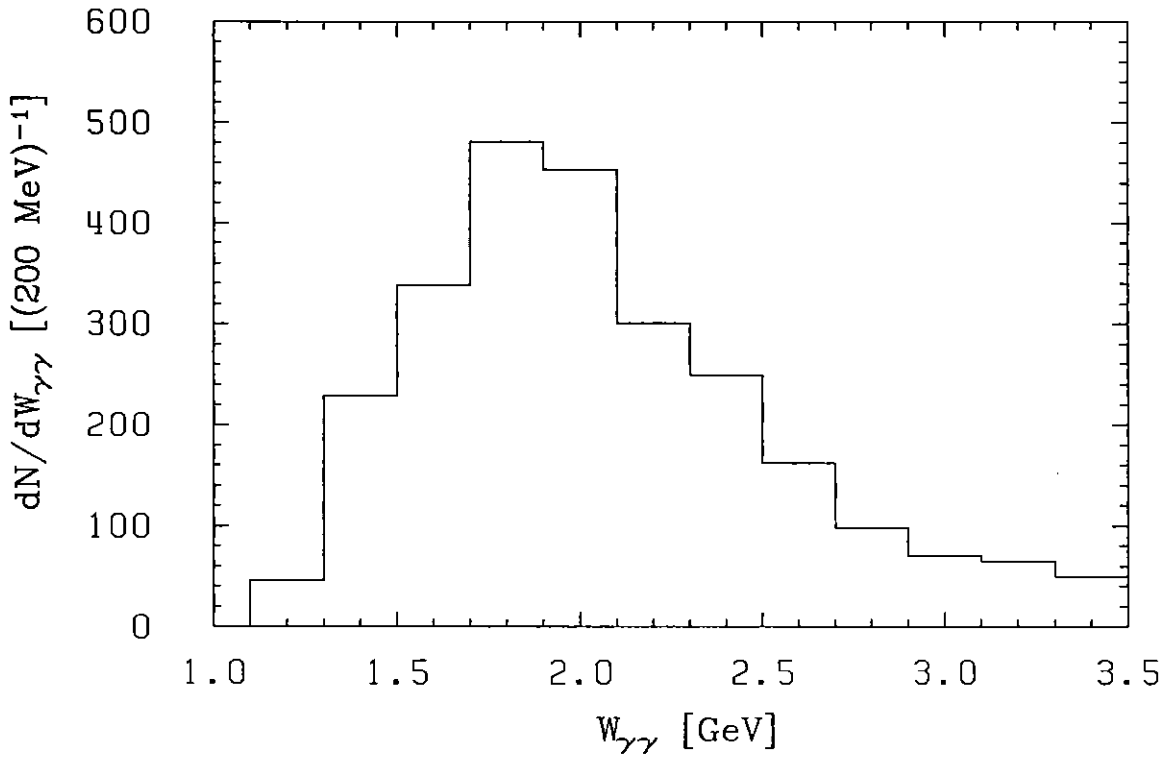

Figure 6.1: Invariant mass distribution of selected $\pi^+\pi^+\pi^0\pi^-\pi^-$ events.

respectively. Using the maximum likelihood method we determine the relative contributions λ_k^2 of all four reactions simultaneously. Since the fitted parameters are contributions λ_k^2 and not the amplitudes λ_k, the obtained contributions and therefore also the cross sections can in principle be negative. The cross sections are calculated according to relations 5.17, 5.18, 5.19 and 5.20. They are shown in fig. 6.2.

Background contributions to the studied reactions have been determined by using the sample of Monte Carlo simulated background events (section 4.2) that have passed the five pion selection criteria. These events have been added to the data sample. A background contribution to the studied reactions is then obtained as a shift in the cross sections due to added background sample (fig. 6.3). The main part of background events migrates in to the channel $\gamma\gamma \to \pi^+\pi^+\pi^0\pi^-\pi^-$. By subtracting these cross sections from the correspondent cross sections shown in fig. 6.2 we obtain cross sections for all four reactions (fig. 6.4). All results are listed in table 6.1. The fit procedure includes all four reactions at $W_{\gamma\gamma}$ greater than 1.3 GeV (figs. 6.2 and 6.3). Below 1.3 GeV the $\pi^+\pi^-$ invariant mass is, due to limited phase space, similarly distributed in reactions $\gamma\gamma \to \omega\pi^+\pi^-$ and $\gamma\gamma \to \omega\rho^0$. This makes it impossible to distinguish between both reactions. A similar difficulty appears also for reactions $\gamma\gamma \to \rho^0\pi^+\pi^0\pi^-$ and $\gamma\gamma \to \pi^+\pi^+\pi^0\pi^-\pi^-$.

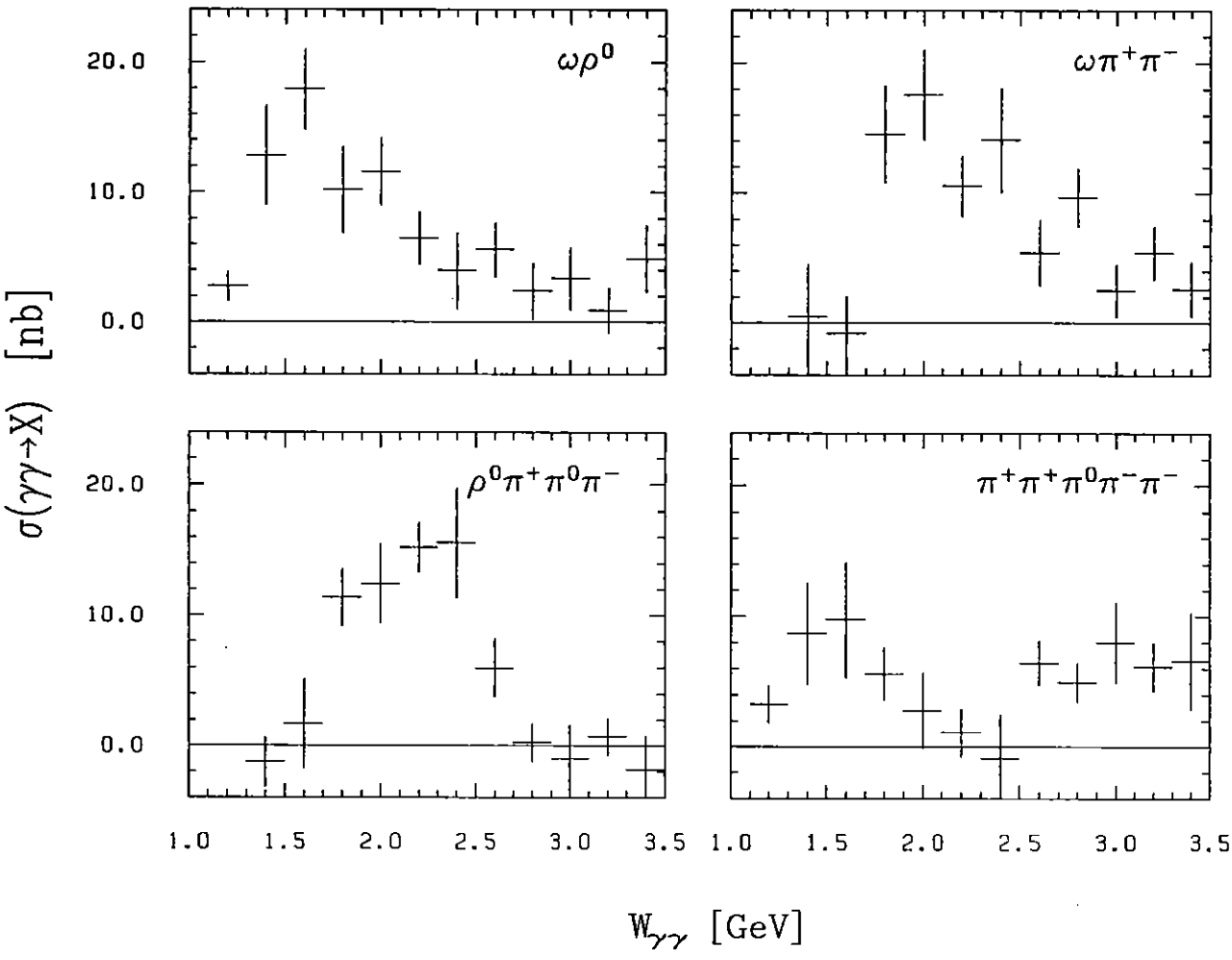

Figure 6.2: Cross sections for reactions $\gamma\gamma \to \omega\rho^0$, $\gamma\gamma \to \omega\pi^+\pi^-$, $\gamma\gamma \to \rho^0\pi^+\pi^0\pi^-$, and $\gamma\gamma \to \pi^+\pi^+\pi^0\pi^-\pi^-$ obtained by a 4 parameter fit. Below 1.3 GeV the production of $\omega\pi^+\pi^-$ and $\rho^0\pi^+\pi^0\pi^-$ is excluded from the fit. Plotted errors are statistical only.

Therefore, only contributions of reactions $\gamma\gamma \to \omega\rho^0$ and $\gamma\gamma \to \pi^+\pi^+\pi^0\pi^-\pi^-$ are included in the fit procedure for $W_{\gamma\gamma}$ energy below 1.3 GeV.

The statistical error includes the error on fitted parameters, acceptance and luminosity function. The major part comes from the first contribution because all others can be sufficiently reduced by increasing the Monte Carlo sample.

The major contributions to the systematic error are related to the Monte Carlo generation of physical processes and the description of the particle detection. One source of the systematic error comes from the incomplete description of two-photon reactions,

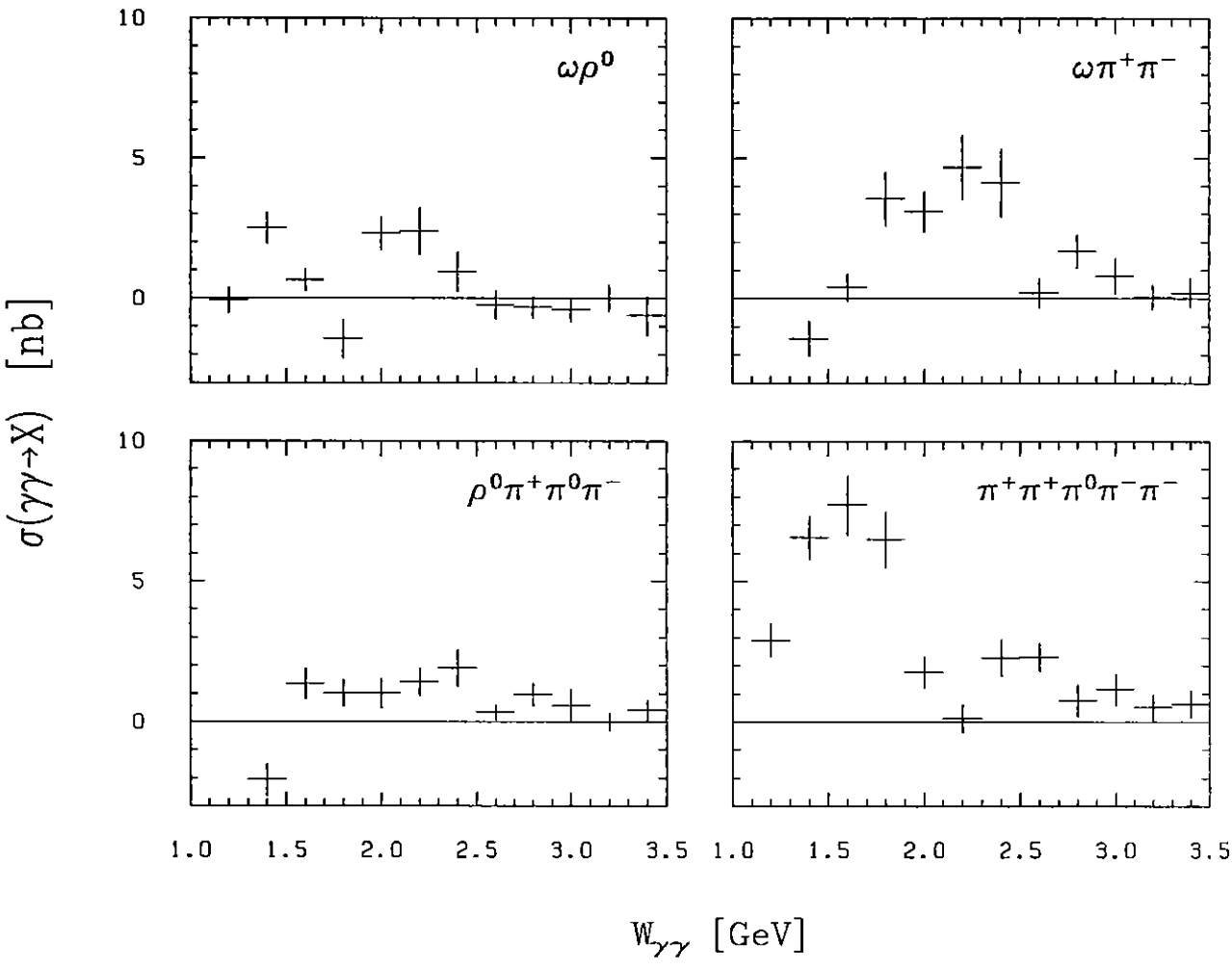

Figure 6.3: Background contribution to reactions $\gamma\gamma \to \omega\rho^0$, $\gamma\gamma \to \omega\pi^+\pi^-$, $\gamma\gamma \to \rho^0\pi^+\pi^0\pi^-$, and $\gamma\gamma \to \pi^+\pi^+\pi^0\pi^-\pi^-$ obtained by the 4 parameter fit. Contributions are given as a cross sections for suitable reaction. Below 1.3 GeV the production of $\omega\pi^+\pi^-$ and $\rho^0\pi^+\pi^0\pi^-$ is excluded from the fit. Plotted errors are statistical only.

hidden in the form factors (eq. 1.16). The error is estimated by calculating the cross sections for two cases:

- form factors are ρ meson poles (eq. 1.17) predicted by the VMD model [11],
- form factors are equal 1.

Assuming these values as extreme cases between which the measured cross section is uniformly distributed, we estimate the systematic error as the standard deviation to be

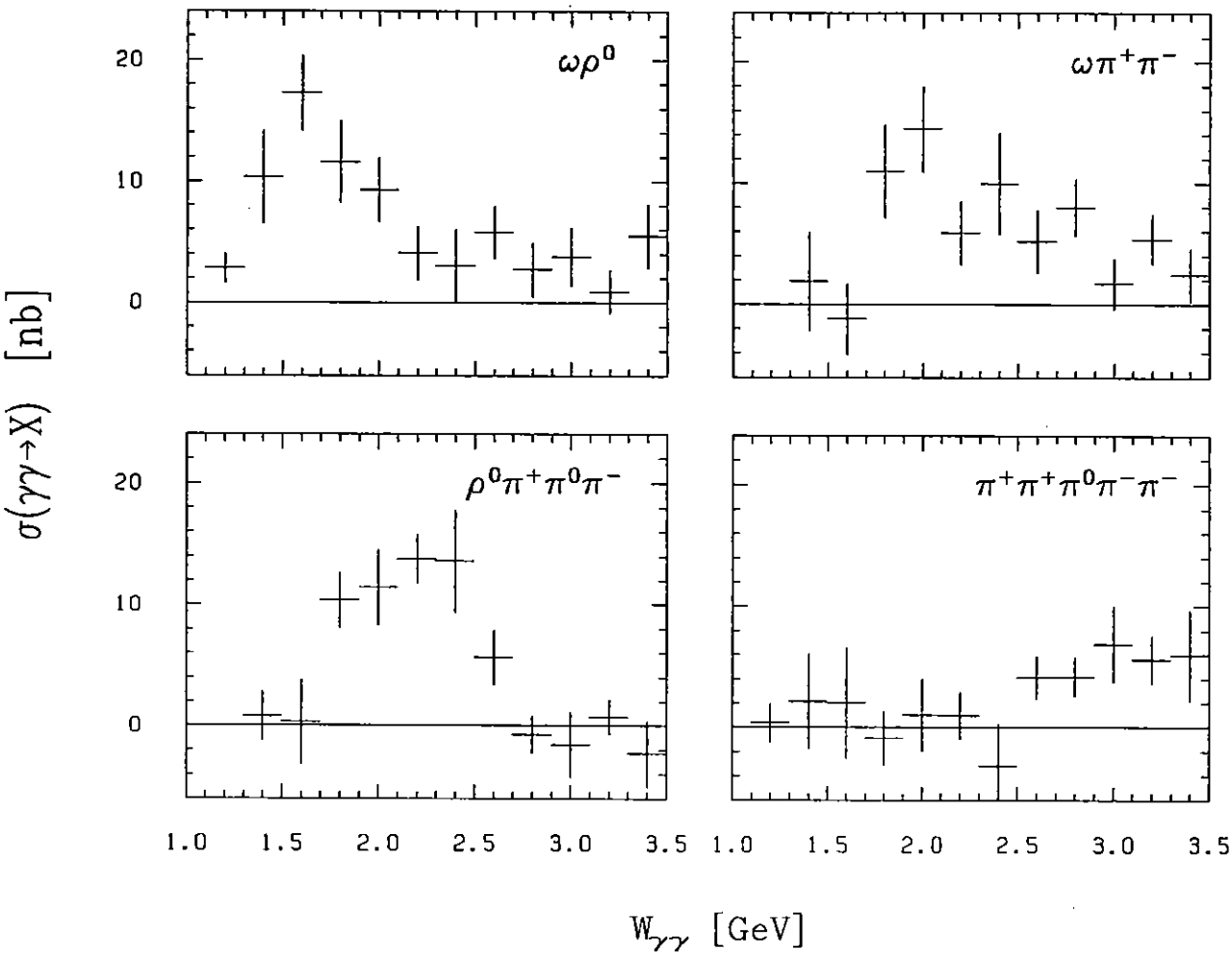

Figure 6.4: Cross sections for reactions $\gamma\gamma \to \omega\rho^0$, $\gamma\gamma \to \omega\pi^+\pi^-$, $\gamma\gamma \to \rho^0\pi^+\pi^0\pi^-$, and $\gamma\gamma \to \pi^+\pi^+\pi^0\pi^-\pi^-$ after background subtraction. Plotted errors are statistical only.

1.3%.

There are two contributions to the systematic error connected with the acceptance calculation. The systematic errors on detector simulation and trigger simulation are 6% and 5% (section 5.2), respectively. Both errors influence only the calculation of the cross sections while the determination of the relative contributions λ_k^2 should be insensible to the systematic multiplication of all acceptances. The simultaneous variation of all acceptances changes only the absolute value of the likelihood function but leaves the position of the maximum unchanged. In the four parameter fit we have assumed an isotropic production of five pions in the final state. However, if the final states are

$W_{\gamma\gamma}$ (GeV)	$\sigma_{\gamma\gamma\to\omega\rho^0}$	$\sigma_{\gamma\gamma\to\omega\pi^+\pi^-}$	$\sigma_{\gamma\gamma\to\rho^0\pi^+\pi^0\pi^-}$	$\sigma_{\gamma\gamma\to\pi^+\pi^+\pi^0\pi^-\pi^-}$
1.1 - 1.3	$2.8 \pm 1.2 \pm 0.6$			$0.4 \pm 1.6 \pm 0.8$
1.3 - 1.5	$10.3 \pm 3.9 \pm 1.6$	$1.9 \pm 4.1 \pm 0.7$	$0.8 \pm 2.0 \pm 0.6$	$2.2 \pm 3.9 \pm 1.9$
1.5 - 1.7	$17.3 \pm 3.1 \pm 1.7$	$-1.2 \pm 2.9 \pm 0.2$	$0.3 \pm 3.5 \pm 0.4$	$2.0 \pm 4.6 \pm 2.2$
1.7 - 1.9	$11.6 \pm 3.4 \pm 1.3$	$11.0 \pm 3.9 \pm 1.9$	$10.4 \pm 2.3 \pm 1.0$	$-0.9 \pm 2.2 \pm 1.8$
1.9 - 2.1	$9.3 \pm 2.7 \pm 1.4$	$14.5 \pm 3.6 \pm 2.0$	$11.4 \pm 3.1 \pm 1.2$	$1.0 \pm 3.0 \pm 0.5$
2.1 - 2.3	$4.1 \pm 2.2 \pm 1.1$	$5.9 \pm 2.6 \pm 2.2$	$13.8 \pm 2.0 \pm 1.5$	$1.0 \pm 2.0 \pm 0.1$
2.3 - 2.5	$3.0 \pm 3.1 \pm 0.5$	$10.0 \pm 4.2 \pm 2.1$	$13.6 \pm 4.2 \pm 1.5$	$-3.2 \pm 3.5 \pm 0.7$
2.5 - 2.7	$5.8 \pm 2.2 \pm 0.6$	$5.2 \pm 2.6 \pm 0.6$	$5.6 \pm 2.3 \pm 0.6$	$4.1 \pm 1.8 \pm 0.8$
2.7 - 2.9	$2.7 \pm 2.2 \pm 0.4$	$8.0 \pm 2.4 \pm 1.3$	$-0.7 \pm 1.5 \pm 0.3$	$4.2 \pm 1.6 \pm 0.6$
2.9 - 3.1	$3.8 \pm 2.4 \pm 0.6$	$1.7 \pm 2.1 \pm 0.4$	$-1.6 \pm 2.7 \pm 0.3$	$6.9 \pm 3.2 \pm 1.0$
3.1 - 3.3	$0.9 \pm 1.8 \pm 0.1$	$5.4 \pm 2.1 \pm 0.9$	$0.7 \pm 1.5 \pm 0.1$	$5.6 \pm 2.0 \pm 0.9$
3.3 - 3.5	$5.5 \pm 2.7 \pm 1.0$	$2.4 \pm 2.2 \pm 0.4$	$-2.3 \pm 2.7 \pm 0.4$	$5.9 \pm 3.7 \pm 1.0$

Table 6.1: Cross sections (in nanobarns) of reactions $\gamma\gamma \to \omega\rho^0$, $\gamma\gamma \to \omega\pi^+\pi^-$, $\gamma\gamma \to \rho^0\pi^+\pi^0\pi^-$, and $\gamma\gamma \to \pi^+\pi^+\pi^0\pi^-\pi^-$ obtained by fit described in text. Statistical (first) and systematic (second) errors are presented.

produced with a definite spin-parity, the acceptances would change. The systematic error on the acceptance determination due to unknown spin-parity structure, is calculated for each $W_{\gamma\gamma}$ bin separately. It is taken as a standard deviation of a uniform distribution between extreme acceptances of all possible spin-parities for the studied reaction. For the reaction $\gamma\gamma \to \omega\rho^0$ the average systematic error over all $W_{\gamma\gamma}$ bins is 9.6%.

The systematic errors due to background contributions are determined for each of the four studied reactions separately. They are proportional to the cross sections from fig. 6.3. Systematic errors on these cross sections are obtained from errors on measured cross section of reaction that dominate the background contribution to the studied reaction. Background to reactions $\gamma\gamma \to \omega\rho^0$ and $\gamma\gamma \to \omega\pi^+\pi^-$ is dominated by two-photon production of $\omega\pi^+\pi^-\pi^0$. A major contribution to other two reactions comes from reaction $\gamma\gamma \to \pi^+\pi^+\pi^0\pi^0\pi^-\pi^-$. For cross section of both background reactions we use the ARGUS results [47].

The ARGUS integrated luminosity L_{ee} is determined with a precision of 1.8% [22] while the branching ratio $\mathrm{Br}(\omega \to 3\pi)$ for $\omega \to \pi^+\pi^0\pi^-$ decay is uncertain by 0.6% [19].

6.2 Results of a Partial-Wave Analysis

From the previous analysis where only invariant-mass distributions were used, the number of measured events corresponding to the reaction $\gamma\gamma \to \omega\rho^0$ is shown in fig. 6.5. Due to the small number of events, we determine the partial wave structure of reaction $\gamma\gamma \to \omega\rho$

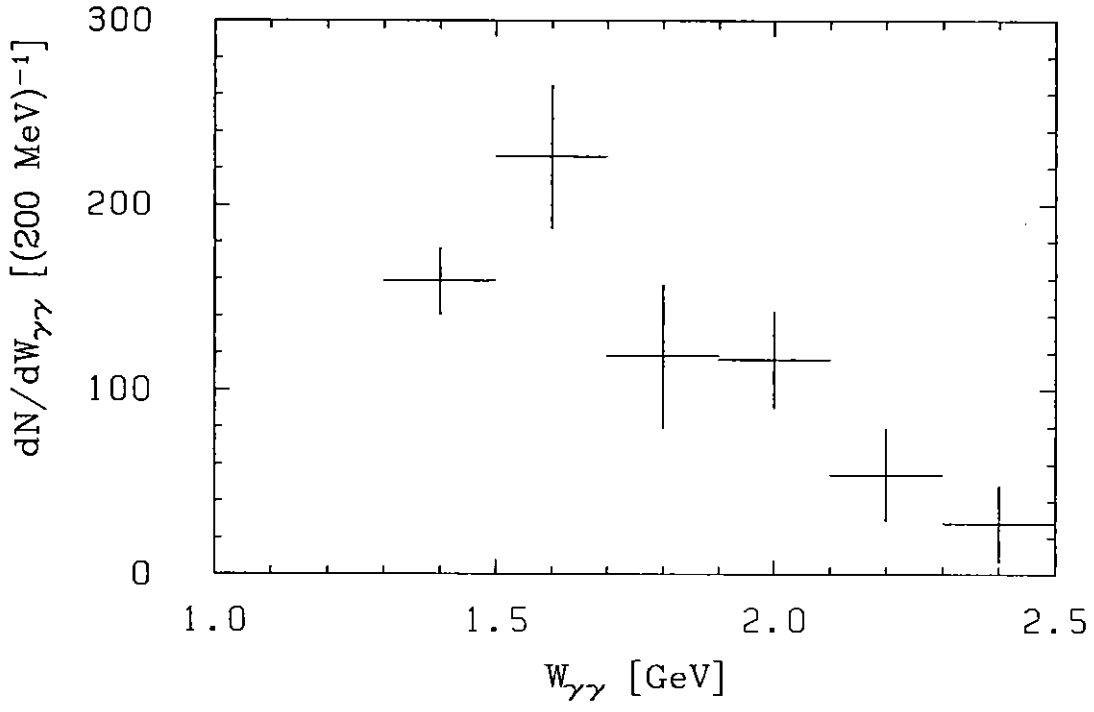

Figure 6.5: Number of measured events corresponding to $\gamma\gamma \to \omega\rho^0$ obtained from four parameter fit.

only in six bins between 1.3 and 2.5 GeV. A fit to the data includes 9 parameters λ_k^2 that represent relative contributions of:

$\gamma\gamma \to \omega\rho^0$:

$(J^P, J_z) = (0^+, 0)$ $\quad$ $(J^P, J_z) = (0^-, 0)$

$(J^P, J_z) = (2^+, 0)$ $\quad$ $(J^P, J_z) = (2^+, 0)$

$(J^P, J_z, S) = (2^-, 0, 1)$ $\quad$ $(J^P, J_z, S) = (2^-, 0, 2)$

$\gamma\gamma \to \omega\pi^+\pi^-$

$\gamma\gamma \to \rho^0\pi^+\pi^0\pi^-$

$\gamma\gamma \to \pi^+\pi^+\pi^0\pi^-\pi^-$

The results of the fit are presented in figs. 6.6 and 6.7. Cross sections shown in fig. 6.7 are already subtracted for the background contribution that is obtained by four parameter fit (fig. 6.3). In both figures only statistical errors are shown. A complete result including systematic errors is collected in table 6.2. The cross sections in fig. 6.7 agree with the

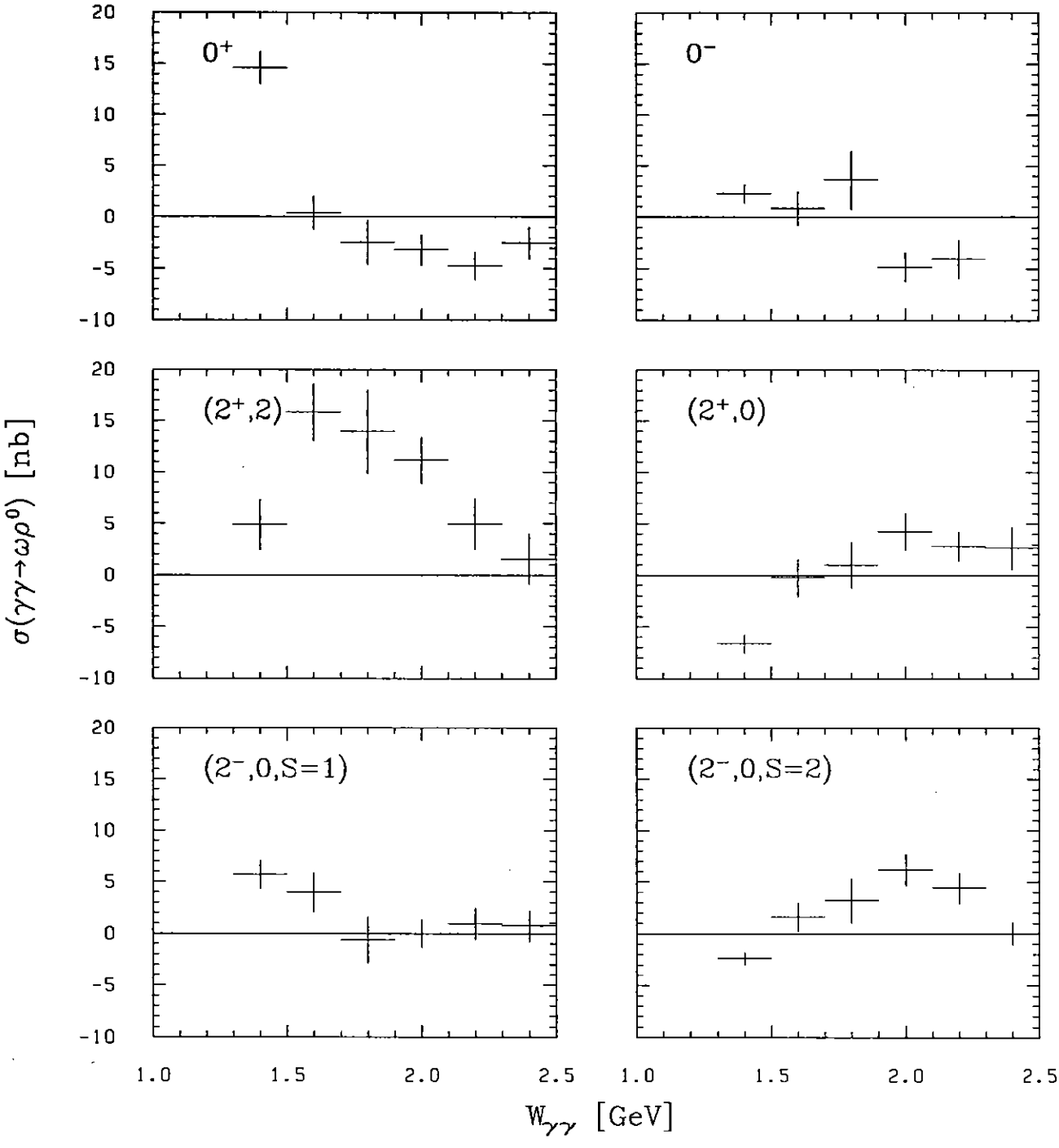

Figure 6.6: Cross sections for different J^P states of $\omega\rho^0$. All cross sections are obtained by a 9 parameter fit. Plotted errors are statistical only.

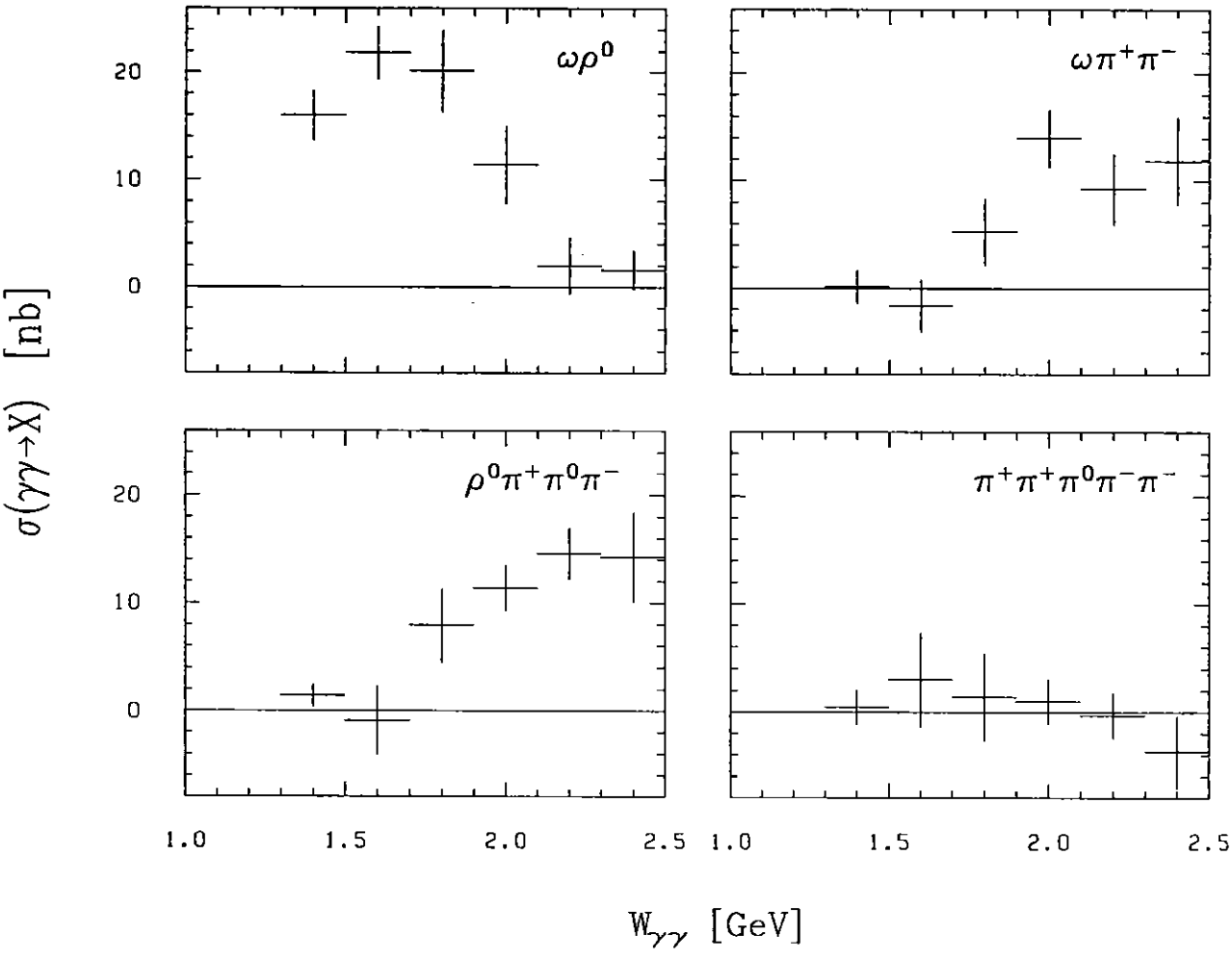

Figure 6.7: Cross sections for $\omega\rho^0$, $\omega\pi^+\pi^-$, $\rho^0\pi^+\pi^0\pi^-$ and $\pi^+\pi^+\pi^0\pi^-\pi^-$. Cross section for $\omega\rho^0$ is obtained by summing up cross sections of all spin-parity contributions 6.6. All cross sections are the result of a 9 parameter fit. Shown error bars are of statistical origin.

results of the four parameter fit. The cross section for the two-photon production of $\omega\rho^0$ is obtained as a sum of all spin-parity contributions. The results of spin-parity analysis show a dominance of the $(J^P, J_z) = (2^+, 2)$ wave. The only exception is the dominance of $(J^P, J_z) = (0^+, 0)$ in the first bin with $W_{\gamma\gamma}$ between 1.3 and 1.5 GeV. Even in this bin, however, the dominance of $(2^+, 2)$ cannot be excluded, as discussed in section 6.4. The helicity 0 component of $J^P = 2^+$ is suppressed over helicity 2 component. The contribution of negative parities is small.

The statistical and systematical errors are calculated in the same way as in the four

$W_{\gamma\gamma}$ (GeV)	$(0^+,0)$	$(0^-,0)$	$(2^+,2)$
1.3 - 1.5	$14.6 \pm 1.6 \pm 1.6$	$2.3 \pm 0.9 \pm 0.2$	$4.9 \pm 2.5 \pm 0.5$
1.5 - 1.7	$0.4 \pm 1.6 \pm 0.05$	$0.9 \pm 1.7 \pm 0.1$	$15.9 \pm 2.8 \pm 1.7$
1.7 - 1.9	$-2.4 \pm 2.2 \pm 0.3$	$3.6 \pm 2.9 \pm 0.4$	$13.9 \pm 4.1 \pm 1.5$
1.9 - 2.1	$-3.2 \pm 1.5 \pm 0.3$	$-4.8 \pm 1.5 \pm 0.5$	$11.1 \pm 2.3 \pm 1.2$
2.1 - 2.3	$-4.7 \pm 1.3 \pm 0.5$	$-4.0 \pm 1.8 \pm 0.4$	$5.0 \pm 2.5 \pm 0.5$
2.3 - 2.5	$-2.5 \pm 1.6 \pm 0.3$	$0.1 \pm 0.1 \pm 0.01$	$1.6 \pm 2.5 \pm 0.2$

$W_{\gamma\gamma}$ (GeV)	$(2^+,0)$	$(2^-,0,S=1)$	$(2^-,0,S=2)$
1.3 - 1.5	$-6.6 \pm 0.9 \pm 0.7$	$5.7 \pm 1.4 \pm 0.6$	$-2.4 \pm 0.6 \pm 0.3$
1.5 - 1.7	$-0.2 \pm 1.8 \pm 0.02$	$4.0 \pm 1.9 \pm 0.4$	$1.6 \pm 1.4 \pm 0.2$
1.7 - 1.9	$1.0 \pm 2.2 \pm 0.1$	$-0.6 \pm 2.2 \pm 0.1$	$3.2 \pm 2.2 \pm 0.3$
1.9 - 2.1	$4.2 \pm 1.8 \pm 0.5$	$0.0 \pm 1.4 \pm 0.0$	$6.2 \pm 1.6 \pm 0.7$
2.1 - 2.3	$2.8 \pm 1.4 \pm 0.3$	$0.9 \pm 1.5 \pm 0.1$	$4.4 \pm 1.5 \pm 0.5$
2.3 - 2.5	$2.7 \pm 2.0 \pm 0.3$	$0.7 \pm 1.5 \pm 0.1$	$0.0 \pm 1.1 \pm 0.0$

$W_{\gamma\gamma}$ (GeV)	$\omega\pi^+\pi^-$	$\rho^0\pi^+\pi^0\pi^-$	$\pi^+\pi^+\pi^0\pi^-\pi^-$
1.3 - 1.5	$0.2 \pm 1.5 \pm 0.6$	$-1.4 \pm 1.0 \pm 0.6$	$0.5 \pm 1.6 \pm 1.8$
1.5 - 1.7	$-1.6 \pm 2.4 \pm 0.2$	$-0.9 \pm 3.2 \pm 0.4$	$3.0 \pm 4.3 \pm 2.2$
1.7 - 1.9	$5.3 \pm 3.1 \pm 1.7$	$7.9 \pm 3.4 \pm 0.8$	$1.4 \pm 4.0 \pm 1.8$
1.9 - 2.1	$14.0 \pm 2.7 \pm 1.9$	$11.4 \pm 2.1 \pm 1.1$	$1.0 \pm 2.0 \pm 0.5$
2.1 - 2.3	$9.2 \pm 3.3 \pm 2.3$	$14.6 \pm 2.4 \pm 1.5$	$-0.3 \pm 2.1 \pm 0.1$
2.3 - 2.5	$11.9 \pm 4.1 \pm 2.2$	$14.2 \pm 4.1 \pm 1.6$	$-3.7 \pm 3.3 \pm 0.7$

Table 6.2: Cross sections (in nanobarns) of reactions $\gamma\gamma \to \omega\rho^0$, $\gamma\gamma \to \omega\pi^+\pi^-$, $\gamma\gamma \to \rho^0\pi^+\pi^0\pi^-$, and $\gamma\gamma \to \pi^+\pi^+\pi^0\pi^-\pi^-$ obtained by a four parameter fit. The presented errors are statistical and sistematical.

parameter fit. The only exceptions appear in $\omega\rho^0$ production. For this reaction, there is no systematic error in the acceptance calculation due to unknown spin parity structure. Unknown angular distributions of some background interactions unable us to determine background contribution to each $\omega\rho^0$ partial wave. Therefore, for all partial waves a ratio of background events to the total number of $\omega\rho^0$ events is taken as a systematic error due to background reactions. Using the result of background determination by four parameter

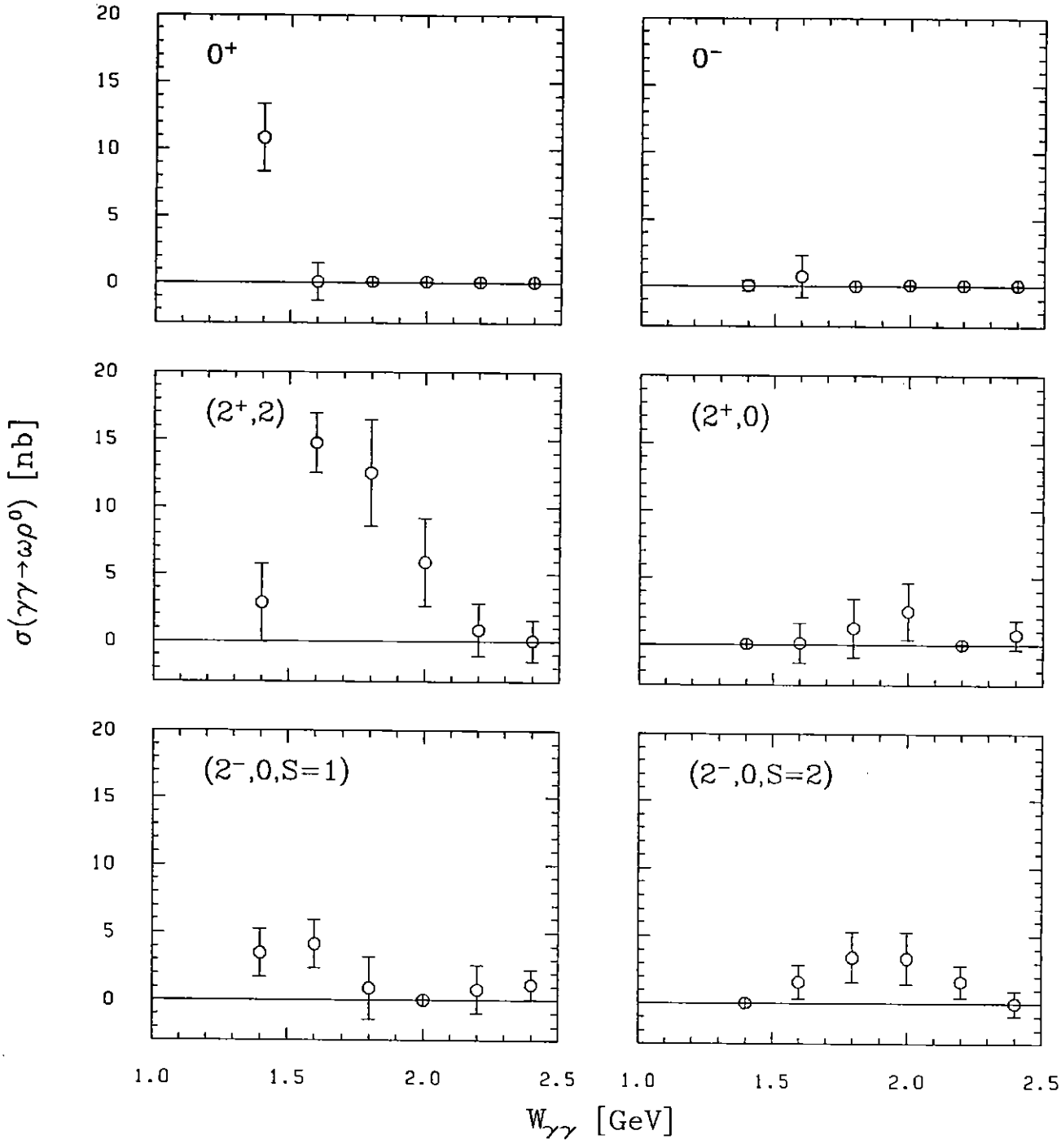

Figure 6.8: Cross sections for different J^P states of $\omega\rho^0$ obtained by a 9 parameter fit. All cross sections were required to be positive. Plotted errors are statistical only.

fit (6.1) we obtain the systematic error to be 7%.

Some cross sections in the present partial-wave analysis obtain negative values because no constraint was imposed on relative contributions λ_k^2. For comparison we calculate also cross sections with constraint that all of them have to be positive. The result of this analysis is collected in fig. 6.8.

6.3 Angular and Invariant Mass Distributions

One-dimensional distributions can provide a simple check of partial-wave analysis. In what follows, some measured distributions are compared with results of the 9 parameter fit. In fig. 6.9 mass spectra of two pions recoiling against the ω meson are shown for all $W_{\gamma\gamma}$ intervals used in the fit procedure. As ω mesons we take three pion combinations with invariant mass differing for less than 25 MeV/c^2 from ω mass. It turns out that mass spectra are in all $W_{\gamma\gamma}$ intervals correctly described by results of the fit.

Some angular distributions are shown for $W_{\gamma\gamma}$ interval between 1.3 and 2.1 GeV in figs. 6.10 and 6.11. All measured distributions are compared with results of the fit and simulated distributions of $\omega\rho^0$ production for all spin-parities. For $\omega\rho^0$ events the invariant mass of two pions recoiling against the ω meson is required to be less than 870 MeV/c^2. Due to the vicinity of the threshold for $\omega\rho^0$ production, there is no lower limit on two-pion invariant mass. Fig. 6.10 shows the distributions of $cos\theta_n$ and $cos\theta_\rho$ where polar angles θ_n and θ_ρ have already been defined in section 1.3. In fig. 6.11 distributions of two angles are shown, which are only weakly affected by the acceptance. The first distribution shows the angle $\theta_{n\pi}$ between pion momenta measured in the ρ^0 rest frame and normal vector $\vec{n}$ (section 1.3) defined in the ω rest frame. Coordinate axes are chosen to be parallel in both frames. The second angle χ is defined in the ω rest frame. The momentum of ρ^0 meson and the momentum of one of its pions define the ρ^0 decay plane. The normal vector $\vec{n}$ together with the ρ^0 momentum defines another plane. The angle between these two planes is χ.

6.4 Test of the Likelihood Method

The likelihood method is checked using the Monte Carlo simulated data sample. From samples generated according to studied reactions $\gamma\gamma \to \omega\rho^0$, $\gamma\gamma \to \omega\pi^+\pi^-$, $\gamma\gamma \to \rho^0\pi^+\pi^0\pi^-$, and $\gamma\gamma \to \pi^+\pi^+\pi^0\pi^-\pi^-$, we combine a sample with the same composition and number of events as expected from results of the 4 parameter fit on the real data. All four reactions have been generated isotropically. Using such a data sample, we perform a

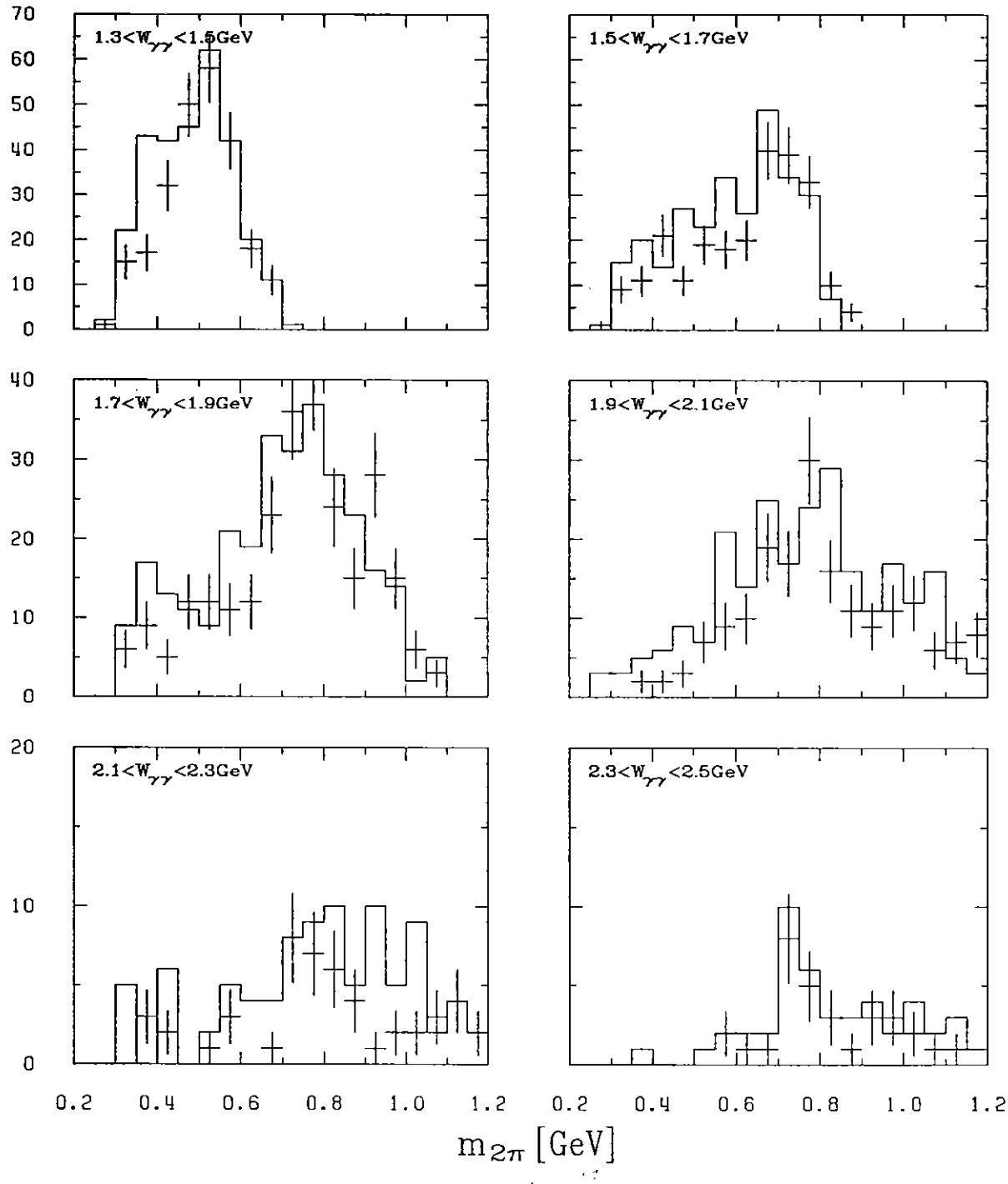

Figure 6.9: Comparison between measured mass spectra of the two pions recoiling against the ω meson (crosses) and results of the 9 parameter fit (histogram). The comparison is shown for all $W_{\gamma\gamma}$ intervals used in the fit.

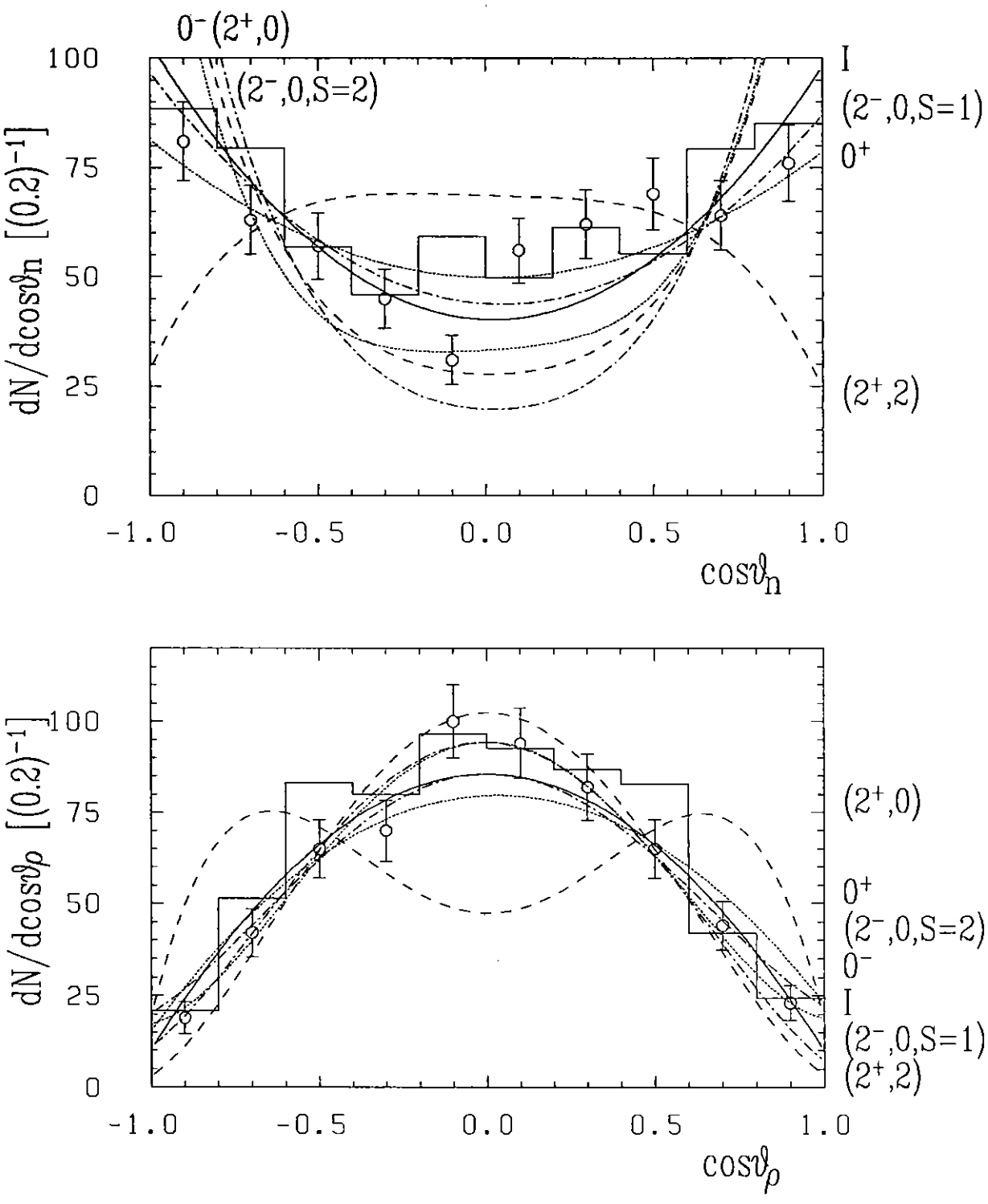

Figure 6.10: Angular distributions of measured events (circles with error bars) and results of the 9 parameter fit (histogram). The definition of the angles is given in the text. In pictures are also shown the simulated distributions of all $\omega\rho^0$ spin-parities included in the fit procedure: $J^P = 0^\pm$ (dotted line), $J^P = 2^+$ (dashed line), $J^P = 2^-$ (dash-dotted line) and isotropic production (solid line). All distributions are shown for $W_{\gamma\gamma}$ between 1.3 and 2.1 GeV.

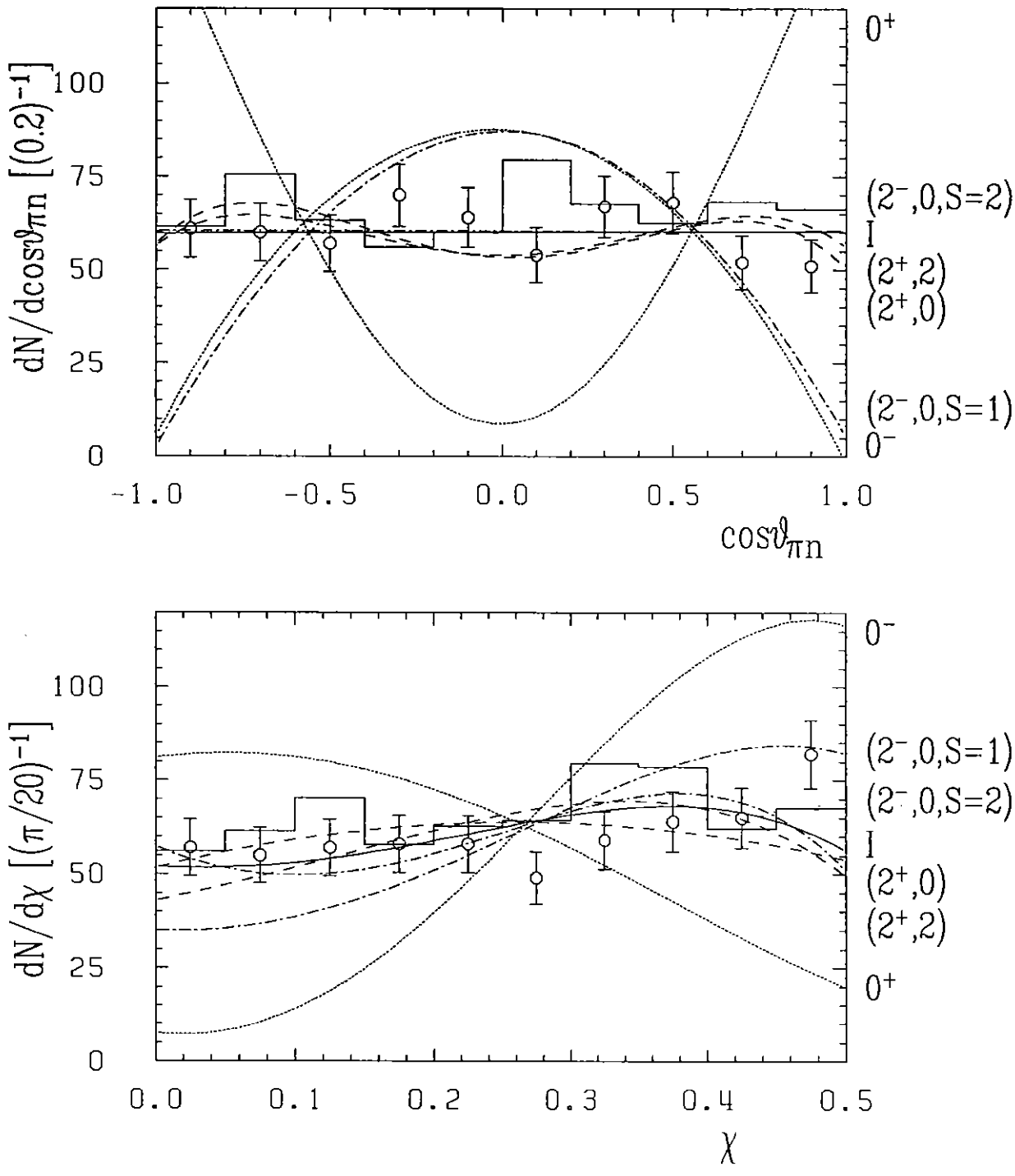

Figure 6.11: Two angular distributions of measured events, fit results, and the simulated distributions of $\omega\rho^0$ spin-parities. The notations coinside with the notation in the previous figure.

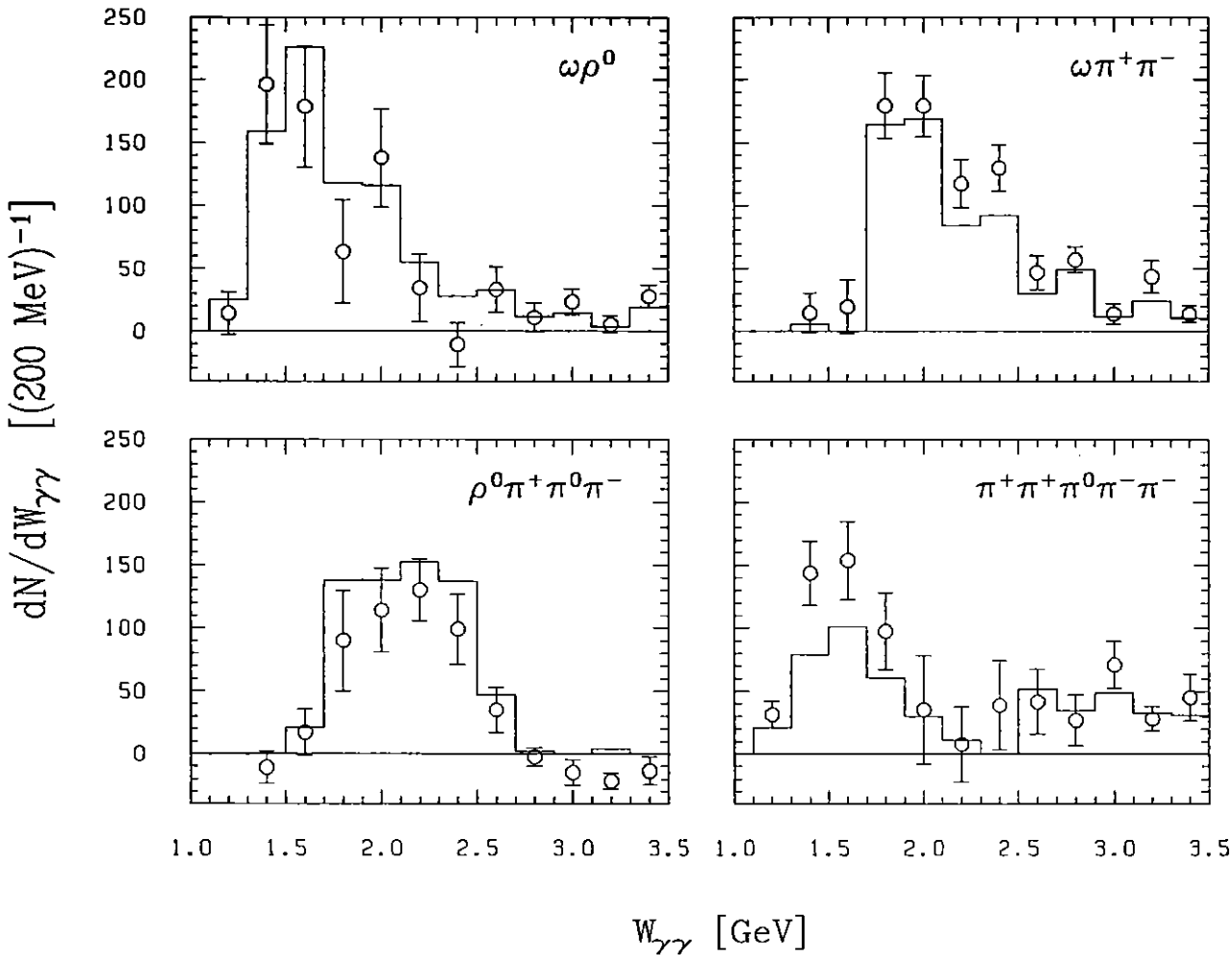

Figure 6.12: Fit results (circles) are compared with the input Monte Carlo data (histogram). The events are generated for reactions $\gamma\gamma \to \omega\rho^0$, $\gamma\gamma \to \omega\pi^+\pi^-$, $\gamma\gamma \to \rho^0\pi^+\pi^0\pi^-$, and $\gamma\gamma \to \pi^+\pi^+\pi^0\pi^-\pi^-$. Five pions are isotropically distributed in two-photon rest frame. Number of the simulated events used in above study coincides with the number of events in the measured data sample.

4 parameter fit. The results of the fit are compared with the input data composition in fig. 6.12. In all cases the input data are correctly reproduced.

In the case of 9 parameter fit, the likelihood method is tested by Monte Carlo data sample where reaction $\gamma\gamma \to \omega\rho^0$ has the same spin-parity composition as it is determined from the real data by the constrained fit (fig. 6.8). Reactions $\gamma\gamma \to \omega\pi^+\pi^-$, $\gamma\gamma \to \rho^0\pi^+\pi^0\pi^-$, and $\gamma\gamma \to \pi^+\pi^+\pi^0\pi^-\pi^-$ are also in this data sample simulated isotropically in two-photon center-of-mass system. Results of 9 parameter fit, performed on this data

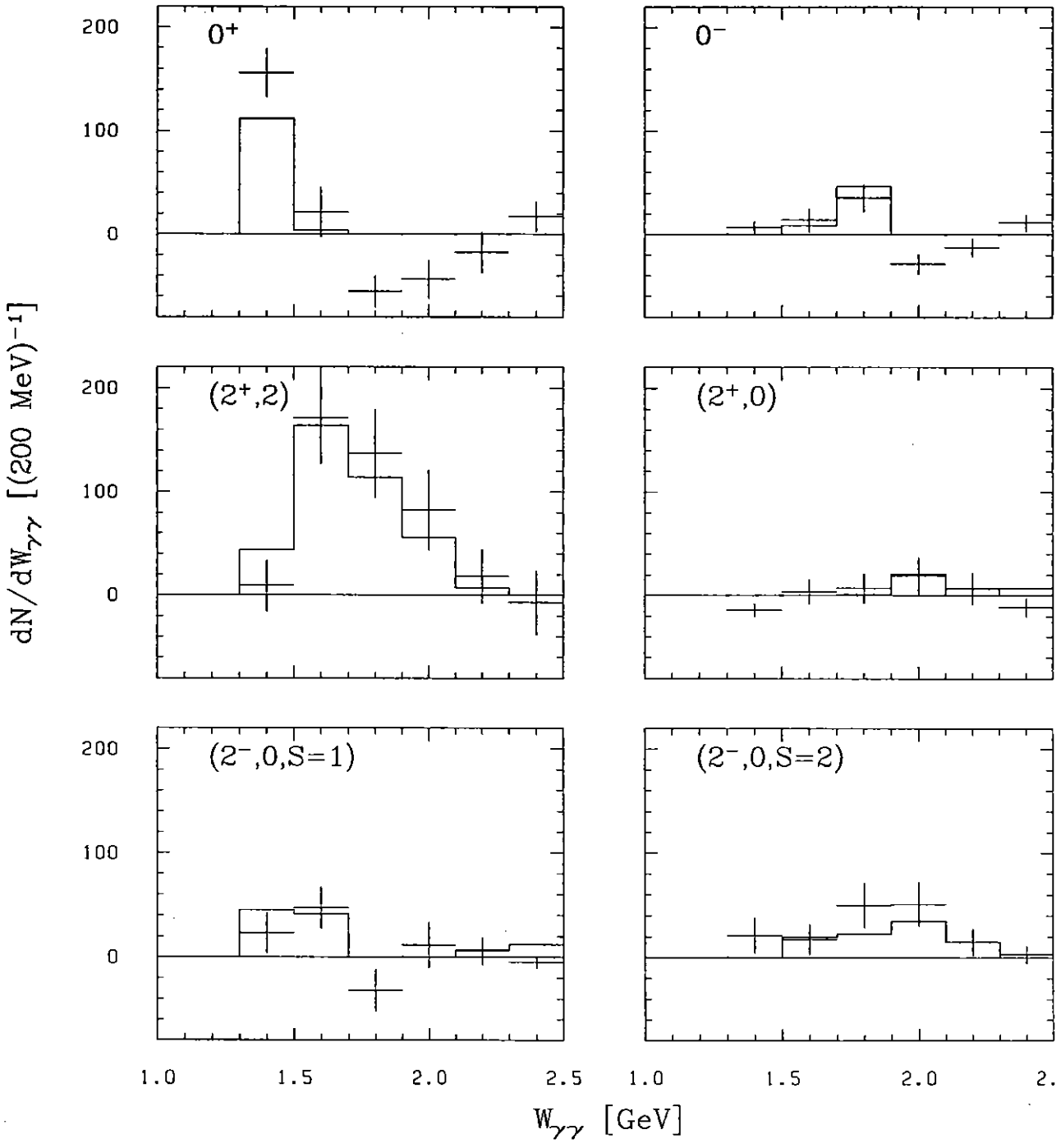

Figure 6.13: Fit results (crosses) are compared with the input Monte Carlo data (histogram) which contains a mixture of various spin-parity states of $\omega\rho^0$ and isotropically distributed $\omega\pi^+\pi^-$, $\rho^0\pi^+\pi^0\pi^-$, and $\pi^+\pi^+\pi^0\pi^-\pi^-$. The sample is a mixture as expected in the measured data.

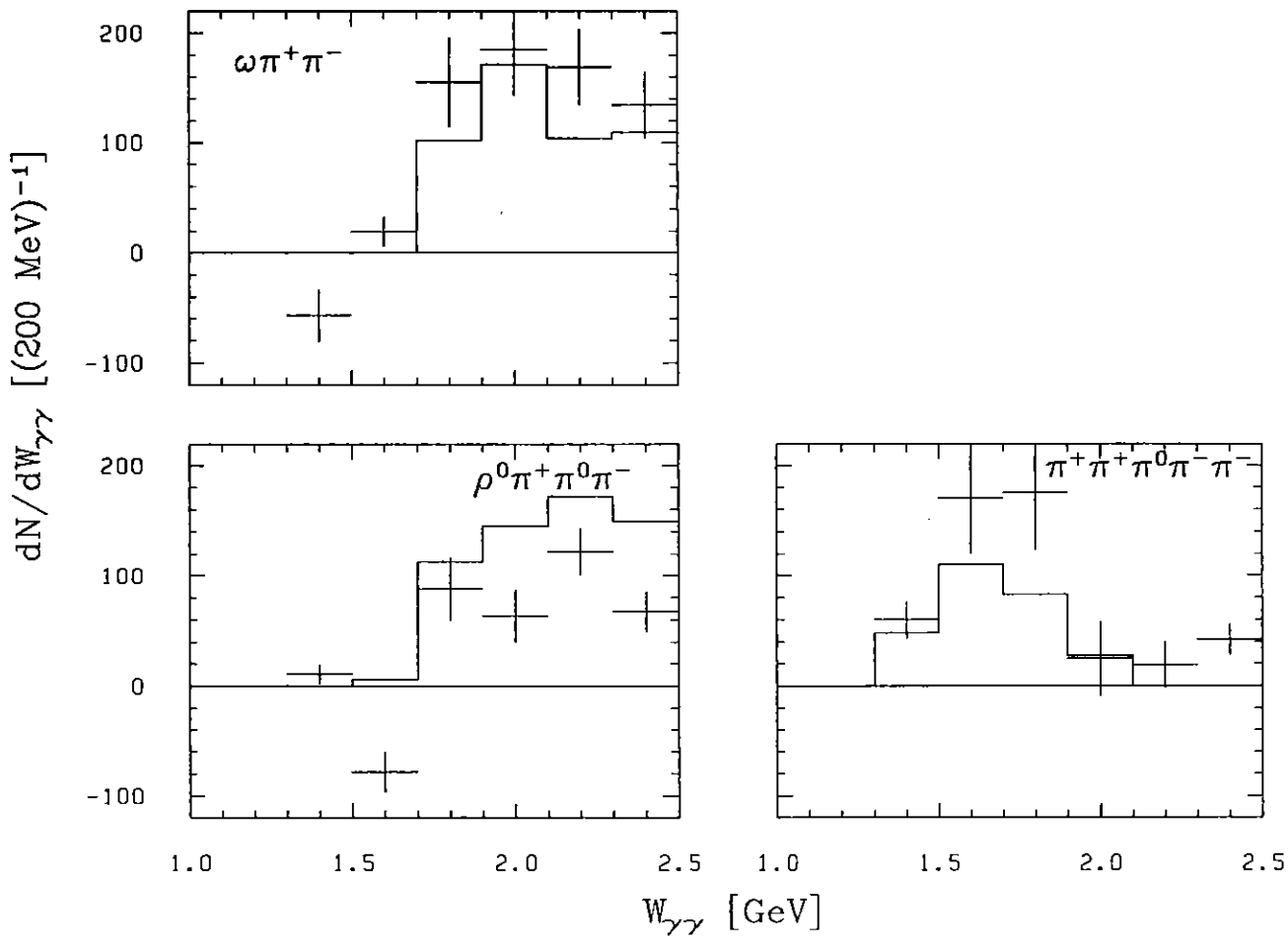

Figure 6.14: Continuation of fig. 6.13

sample, reproduce the composition of the sample correctly (figs. 6.13 and 6.14).

To test a possible origin of 0^+ over $(2^+,2)$ dominance as observed in the $W_{\gamma\gamma}$ interval of 1.3 to 1.5 GeV (fig. 6.6) the 9 parameter fit was performed on Monte Carlo data where production of $\omega\rho^0$ is pure $(J^P,J_z) = (2^+,2)$. The number of $\omega\rho^0$ events in the sample correspond to the total number of $\omega\rho^0$ events obtained by the 9 parameter fit on measured data. Also number of events for reactions $\gamma\gamma \to \omega\pi^+\pi^-$, $\gamma\gamma \to \rho^0\pi^+\pi^0\pi^-$, and $\gamma\gamma \to \pi^+\pi^+\pi^0\pi^-\pi^-$ are determined by the same fit procedure. In fig. 6.15 fit results are compared with the composition of the Monte Carlo sample for all $\omega\rho^0$ spin-parities. Results of the fit are similar to the one determined on measured data. The large migration of the $(2^+,2)$ contribution into the 0^+ contribution could only be observed in the first

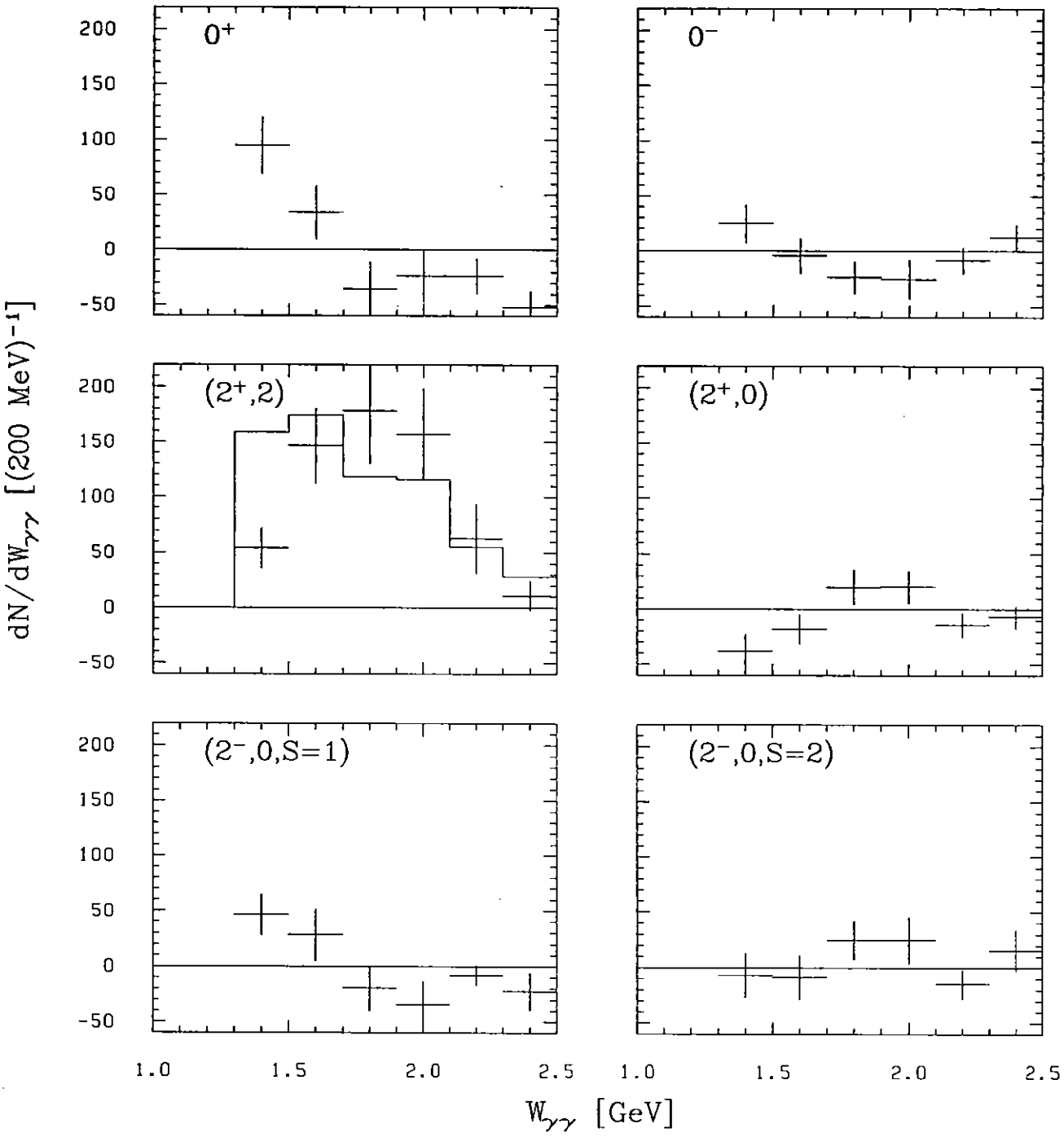

Figure 6.15: Comparison between simulated number of events (histogram) and results of the fit (crosses) for all $\omega\rho^0$ spin-parities. Production of $\omega\rho^0$ is simulated purely $2^+, 2$ while reactions $\gamma\gamma \to \omega\pi^+\pi^-$, $\gamma\gamma \to \rho^0\pi^+\pi^0\pi^-$, and $\gamma\gamma \to \pi^+\pi^+\pi^0\pi^-\pi^-$ are simulated isotropically. The simulated number of events for all reactions correspond to the numbers obtained by the 9 parameter fit on measured data. Number of $2^+, 2$ events equals to the total number of $\omega\rho^0$ events determined in measured data.

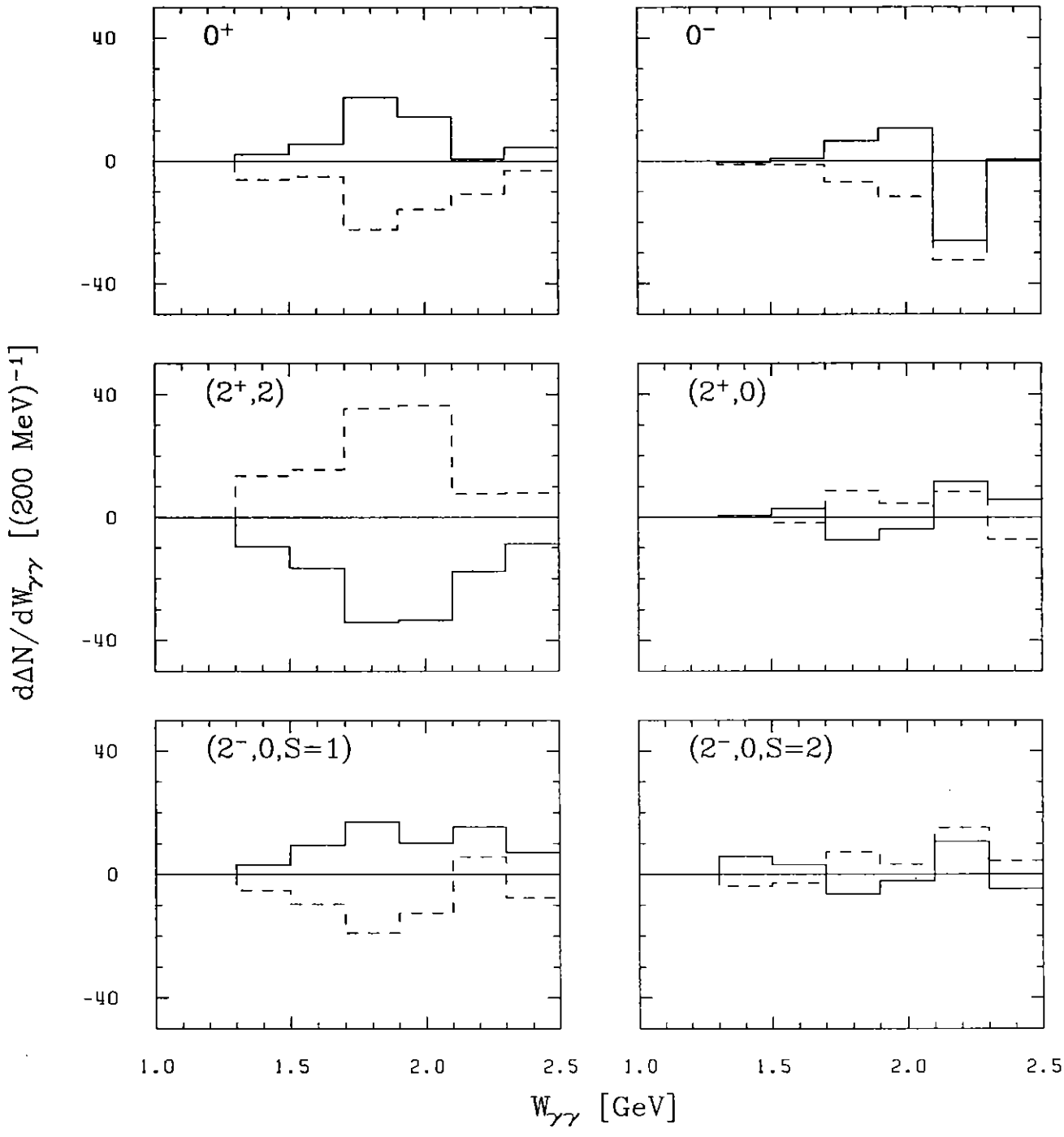

Figure 6.16: Shifts of fitted number of events due to variation of acceptance for $2^+, 2\ \omega\rho^0$ wave. The acceptance is changed for +5% (full line) and −5% (dashed line). The 9 parameter fit is performed on Monte Carlo data where production of $\omega\rho^0$ is pure $2^+, 2$ wave (fig. 6.15).

$W_{\gamma\gamma}$ interval (1.3-1.5 GeV). A possible explanation for such a behaviour is that the $\omega\rho^0$ system is below the nominal threshold where the uncertainties in matrix elements and acceptances become very important. We therefore conclude that the data are consistent with a dominance of the $(2^+, 2)$ wave over the whole invariant mass range.

The same Monte Carlo sample was also used to find the influence of acceptance accuracy on fit results. The acceptance of $2^+, 2$ wave was changed for $\pm 5\%$. In fig. 6.16 a shift of fitted number of events due to changed acceptance, is shown for all $\omega\rho^0$ waves.

Since we have assumed isotropic production of $\omega\pi^+\pi^-$, $\rho^0\pi^+\pi^0\pi^-$, and $\pi^+\pi^+\pi^0\pi^-\pi^-$ in our analysis, it is necessary to check the migration of possible non-isotropic angular distribution of these channels to $\omega\rho^0$ waves. For this reason we use a Monte Carlo data sample where reactions $\gamma\gamma \to \omega\pi^+\pi^-$, $\gamma\gamma \to \rho^0\pi^+\pi^0\pi^-$, and $\gamma\gamma \to \pi^+\pi^+\pi^0\pi^-\pi^-$ have a definite spin parity. The simulation of $\omega\rho^0$ production remains the same as in the sample used for the test of 9 parameter fit. A difference between fit results obtained by data where production of $\omega\pi^+\pi^-$, $\rho^0\pi^+\pi^0\pi^-$, and $\pi^+\pi^+\pi^0\pi^-\pi^-$ is pure $(J^P, J_z) = (2^+, 2)$ and data with isotropic production of these three final states is shown in figure 6.17. Most of migration to the $\omega\rho^0$ partial-wave with spin-parity $(J^P, J_z) = (2^+, 2)$ comes from $\omega\pi^+\pi^-$ channel. It seems that the Breit-Wigner form of the invariant masses is more restrictive than the angular distributions. This leads to conclusion that the contribution of $\omega\pi^+\pi^-$, $\rho^0\pi^+\pi^0\pi^-$, and $\pi^+\pi^+\pi^0\pi^-\pi^-$ can be reliably estimated using an isotropic angular distribution in the fit.

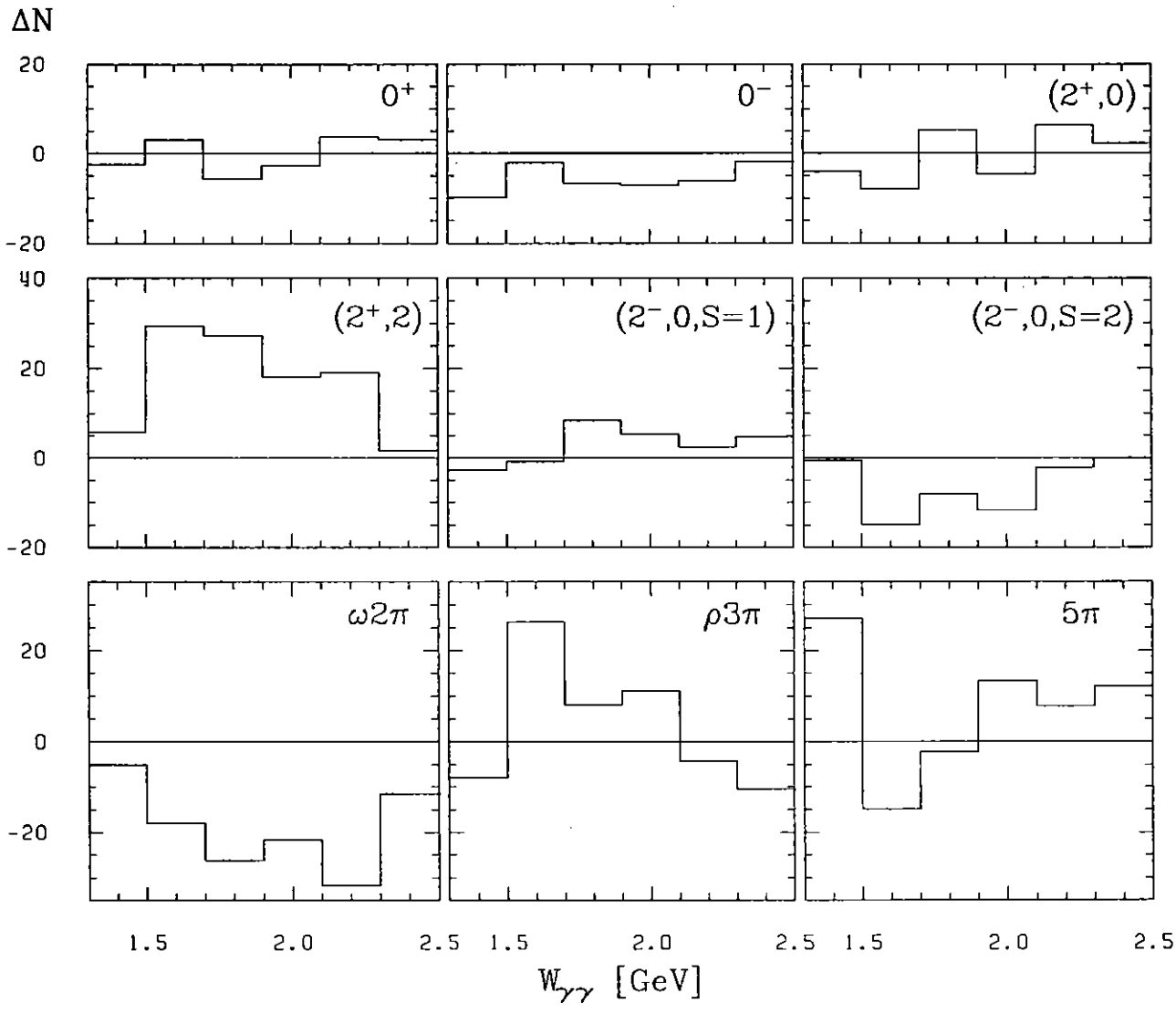

Figure 6.17: A difference between number of events obtained by 9 parameter fit on Monte Carlo data sample with production of $\omega\pi^+\pi^-$, $\rho^0\pi^+\pi^0\pi^-$, and $\pi^+\pi^+\pi^0\pi^-\pi^-$ according to pure $(J^P, J_z) = (2^+, 2)$ and data with isotropic production of these three final states.

Chapter 7

Analysis of the reaction $\gamma\gamma \to \rho^0\phi \to \pi^+\pi^-K^+K^-$

The two-photon production of the vector meson pair $\rho^0\phi$ is analyzed on the data sample corresponding to an integrated luminosity of 472.7 pb^{-1}. Both vector mesons ρ^0 and ϕ are reconstructed by their dominant decay channels $\pi^+\pi^-$ and K^+K^-, respectively, so four charged particles $\pi^+\pi^-K^+K^-$ are required in the final state. The event selection includes similar criteria as we have used in section 4.1:

- Four charged particles with zero net charge have to fit to a common vertex at the interaction point. Two of them with opposite charge have to be identified as pions with $\lambda_\pi > 1\%$, and the other two as kaons $\lambda_K > 1\%$. For these particles the probabilities for being electron P_e and muon P_μ should not exceed 10%.
- No other charged particle is allowed to point to the common vertex at the interaction point.
- Events with neutral particles recognized by secondary vertex, as K^0_s, Λ or converted photon, are rejected.
- Unconnected showers are not allowed in the calorimeter unless they are recognized as:
  - calorimeter noise,
  - fake photons due to shower splitting,
  - photons produced by back scattered neutral pions which come from hadron interactions in the calorimeter, and
  - back scattered neutrons.

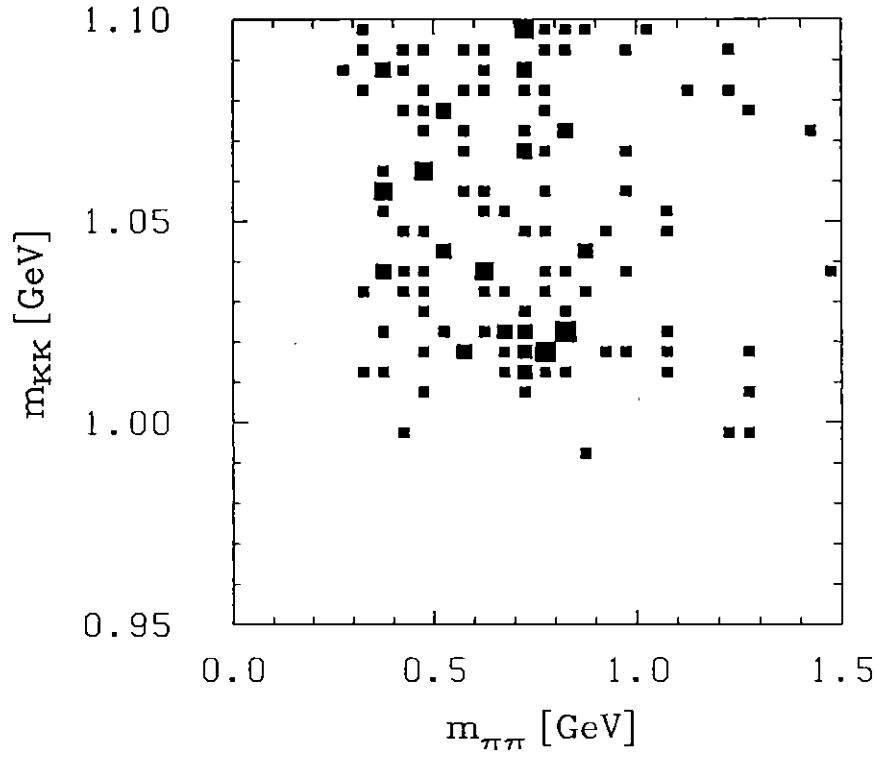

Figure 7.1: Scatter plot of the $\pi^+\pi^-$ invariant mass versus the invariant mass of K^+K^- pairs for selected $\pi^+\pi^-K^+K^-$ combinations with invariant mass between 1.5 and 3.5 GeV/c^2.

Due to similar behaviour of kaons and pions in the calorimeter, the same criteria are used for fake photons of both particles.

- The total transverse momentum of selected particles $\pi^+\pi^-K^+K^-$ is smaller than 200 MeV/c.

- The momentum conservation has to be fulfilled for all particles involved in the reaction, including undetected electron and positron.

After applying these criteria we obtain a scatter plot of the $\pi^+\pi^-$ versus K^+K^- invariant masses where an enhancement is seen in the $\rho^0\phi$ region (fig. 7.1).

The ϕ mesons are identified by the two-kaon invariant mass m_{KK}, which should not differ from the ϕ nominal mass for more than 12 MeV/c^2. Since the resolution $\sigma_{m_{KK}}$ is 4 MeV, such a criterion rejects a negligible amount of ϕ mesons. In fig. 7.2 the invariant mass distribution of K^+K^- pairs is shown. A clear peak is seen that corresponds to the mass of the ϕ meson. Figure 7.3 shows the distribution of two-pion invariant masses for all

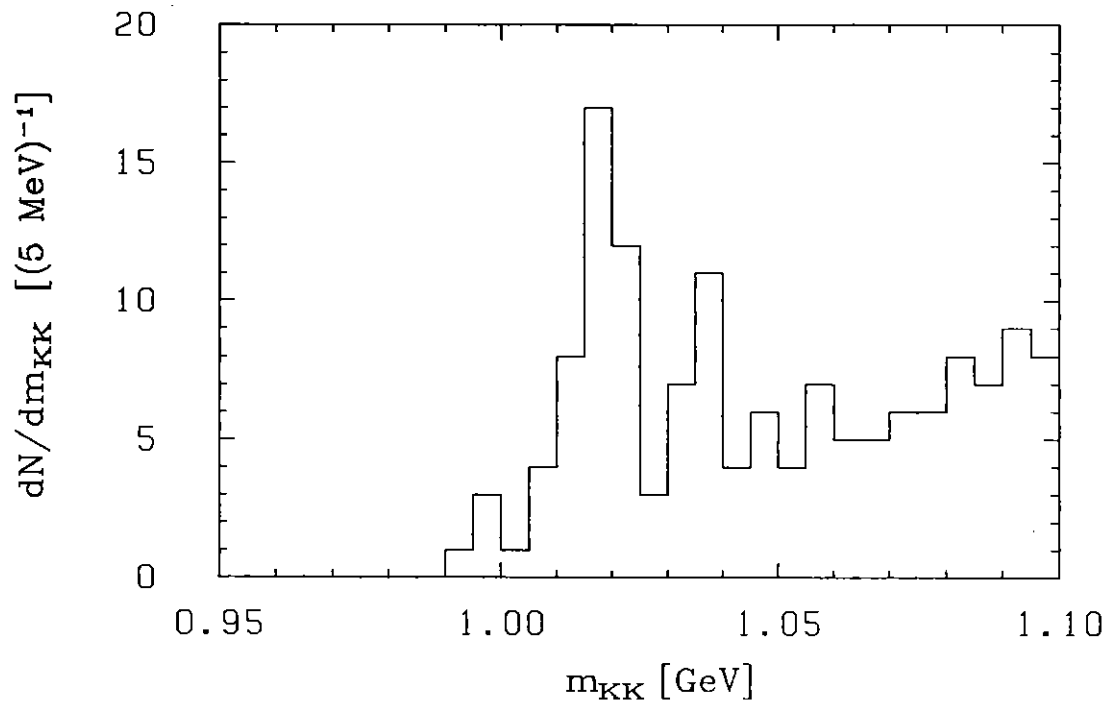

Figure 7.2: Two-kaon invariant mass distribution for selected $\pi^+\pi^-K^+K^-$ events with $W_{\gamma\gamma} < 3.5$ GeV/c^2

$\pi^+\pi^-K^+K^-$ events where ϕ mesons were recognized. Since ρ^0 is a broad resonance, the distribution of the $\pi^+\pi^-$ invariant mass depends on the two-photon energy $W_{\gamma\gamma}$. This is particularly noticeable at the $\rho^0\phi$ threshold where, due to lack of energy, the $\pi^+\pi^-$ invariant mass shifts to the values below the ρ^0 nominal mass. Therefore, a cut on $\pi^+\pi^-$ has to depend on the $W_{\gamma\gamma}$ invariant mass. To determine the criterion on the $\pi^+\pi^-$ mass we use the simulation of the reaction $\gamma\gamma \to \rho^0\phi$. The simulation is done in a similar way as the one for the reaction $\gamma\gamma \to \omega\rho^0$ (chapter 3). The only difference between both simulations is in the decay of two-photon intermediate state. Final state particles $\pi^+\pi^-K^+K^-$ are generated according to their phase space in two-photon center-of-mass system weighted by the square of the decay matrix element $D_{\rho\phi}$ from eq. 1.60. The event generation is followed by the detector and trigger simulation and finally by the event reconstruction. This Monte Carlo sample is used for the determination of the invariant masses of pion pairs that correspond to the ρ^0 meson. The cut is defined in the following way: at each $W_{\gamma\gamma}$ energy only 10% of the simulated events are allowed to lie outside the $\pi^+\pi^-$ interval, i.e. 5% on each side of the area. The obtained area is marked in a double plot (fig. 7.3) showing the distribution of measured $\pi^+\pi^-K^+K^-$ events with recognized ϕ mesons. Events within this area are treated as $\rho^0\phi$ events. Their dependence on $W_{\gamma\gamma}$ is shown in histogram (fig. 7.4). We tried to determine the background contribution using a Monte

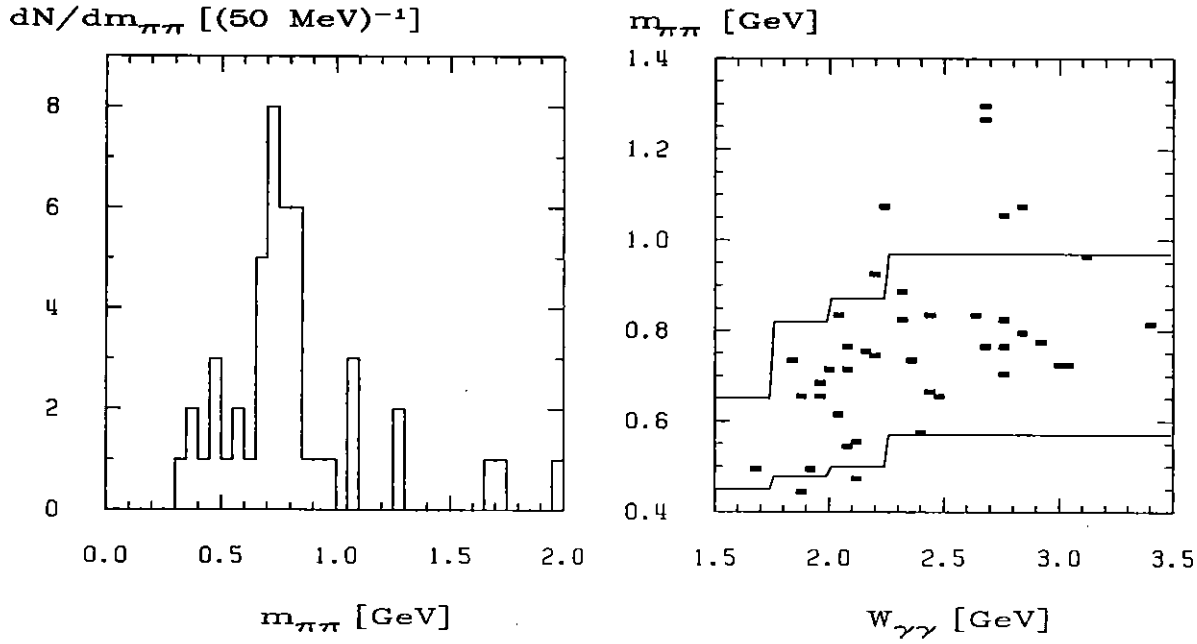

Figure 7.3: Two-pion invariant mass $m_{\pi\pi}$ distribution for the selected $\pi^+\pi^-K^+K^-$ events with ϕ candidates ($|m_{KK}-m_\phi| < 12MeV/c^2$) (left), and the distribution of these events in the $m_{\pi\pi}$, $W_{\gamma\gamma}$ plane (right). $\pi^+\pi^-$ pairs are recognized as ρ^0 decay products if they lie between both curves in the scatter plot. The cut was derived from Monte Carlo simulation.

Carlo simulation of other two-photon interactions, tau pair production $e^+e^- \to \tau\tau$ and reactions $e^+e^- \to$ hadrons (section 4.2). The number of simulated events corresponding to a particular background process depends on its cross section and the integrated luminosity of measured data sample. For reactions $\gamma\gamma \to \omega\rho$, $\gamma\gamma \to \omega\pi^+\pi^-$, $\gamma\gamma \to \rho\pi^+\pi^-\pi^0$, and $\gamma\gamma \to \pi^+\pi^-\pi^0\pi^+\pi^-$ we use the cross sections determined in chapter 6 while for other reactions the cross sections from already published measurements are taken. Due to severe requirements on $\pi^+\pi^-$ and K^+K^- invariant masses, a large sample of Monte Carlo data is needed to determine the background contribution to the studied reaction $\gamma\gamma \to \rho\phi$ with sufficient precision. Since simulation of all background processes is computer time consuming, it is used to determine only the composition of background in the region shown in fig. 7.1. 40% of all background events are produced in $\gamma\gamma \to \pi^+\pi^-K^+K^-$ reactions with final state particles generated according to phase space. Other important contributions come from reactions $\gamma\gamma \to K^{*0}K^\pm\pi^\mp$ and $\gamma\gamma \to K^{*0}\bar{K}^{*0}$ with 30% and 23%, respectively. Such a composition of the background suggests a determination of the background contribution to the selected $\rho^0\phi$ events by using the simulation of the reaction $\gamma\gamma \to \pi^+\pi^-K^+K^-$. The number of simulated events is normalized to the number of measured events within the region shown in fig. 7.1. Of course, the area around the $\rho\phi$ region

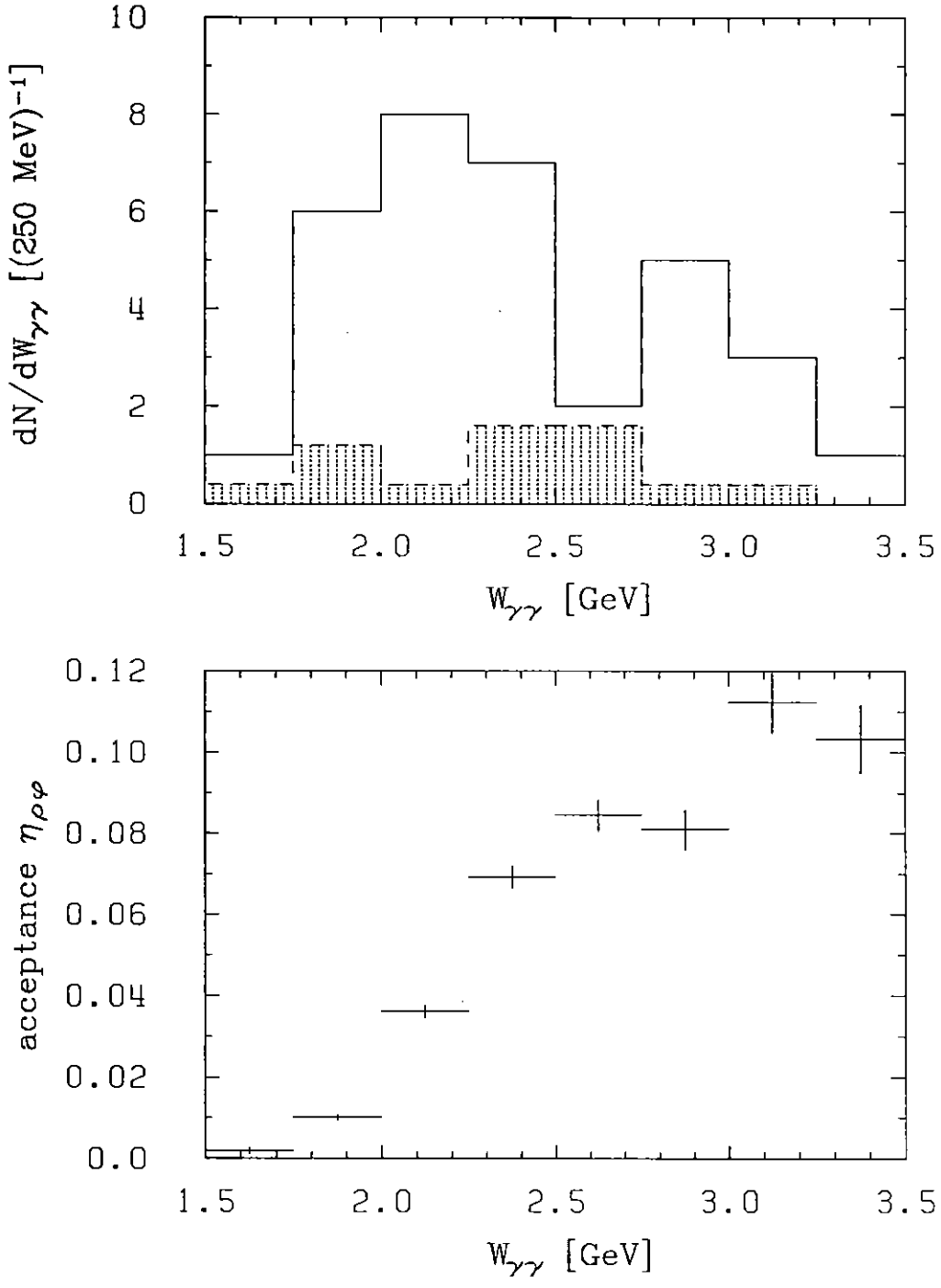

Figure 7.4: a.) Distribution of $\pi^+\pi^-K^+K^-$ invariant mass for all events that fulfill the selection criteria for reaction $\gamma\gamma \to \rho^0\phi$. The dotted histogram shows the expected background predicted by simulation.
b.) The acceptance for this reaction obtained by simulation.

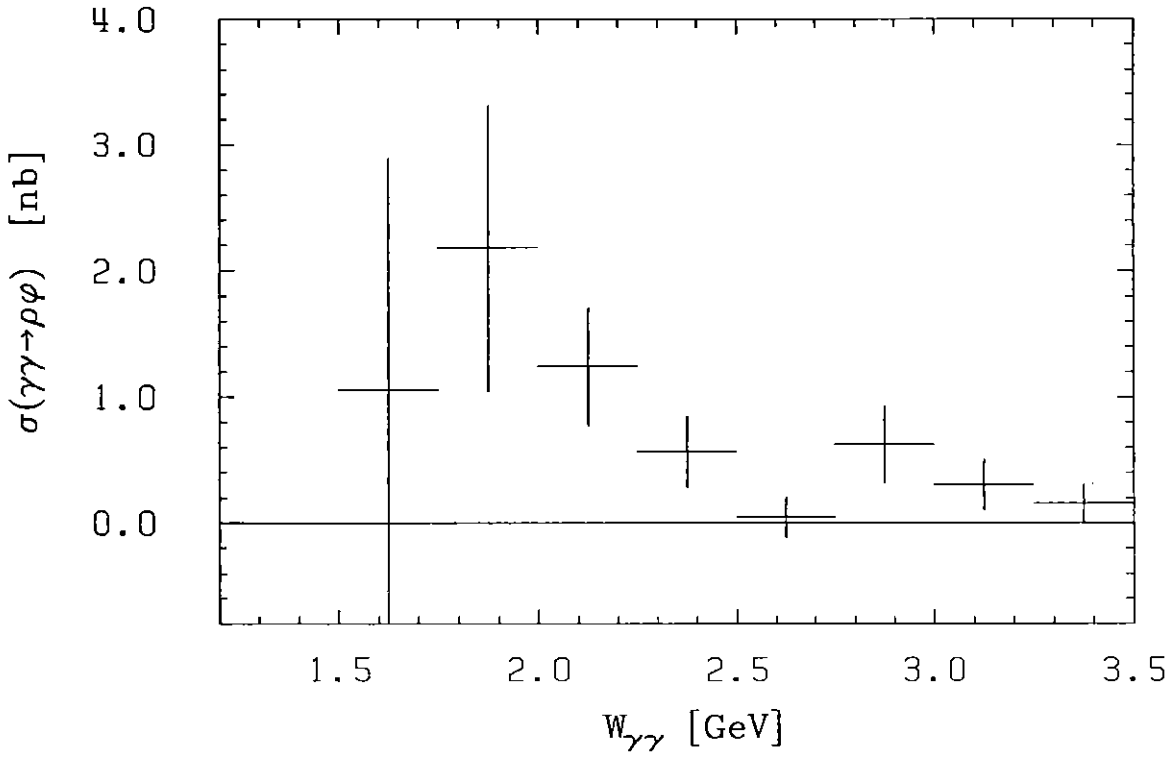

Figure 7.5: Cross section of the reaction $\gamma\gamma \to \rho^0\phi$.

($1.008 < m_{KK} < 1.032,\ 0.45 < m_{\pi\pi} < 0.97$) was excluded from the normalization. We determine the background contribution to the selected $\rho^0\phi$ events (fig. 7.4) by counting the properly scaled simulated $\pi^+\pi^- K^+K^-$ events passing the selection criteria.

The acceptance for the reaction $\gamma\gamma \to \rho\phi$ is calculated from the same sample of simulated data that was used for the determination of the limits imposed to the ρ region of the two-pion invariant mass distribution. The calculation is similar to the one described in section 5.2. The acceptance dependence on $W_{\gamma\gamma}$ is shown in fig. 7.4. Using the relation

$$\sigma_{\gamma\gamma\to\rho^0\phi} = \frac{N_i - N_i^b}{\eta_i L_{ee} L^i_{\gamma\gamma} \mathrm{Br}(\rho \to 2\pi)\mathrm{Br}(\phi \to 2K)} \ , \tag{7.1}$$

we obtain the cross section for two-photon reaction $\gamma\gamma \to \rho^0\phi$ shown in fig. 7.5. In the above relation, N_i, N_i^b, and η_i are number of selected events, expected background, and selection acceptance, respectively. All quantities are related to a specific $W_{\gamma\gamma}$ interval i. The $L^i_{\gamma\gamma}$ denotes the average luminosity function. Decay fractions $\mathrm{Br}(\rho \to 2\pi)$ and $\mathrm{Br}(\phi \to 2K)$ for $\rho^0 \to \pi^+\pi^-$ and $\phi \to K^+K^-$ decays respectively, are taken from [19].

The errors in fig. 7.5 are statistical only. The complete results are listed in table 7.1 where also systematical errors are presented. The main contributions to the systematic

$W_{\gamma\gamma}$ (GeV)	$\sigma_{\gamma\gamma\to\rho^0\phi}$ [nb]
1.50 - 1.75	$1.1 \pm 1.8 \pm 0.1$
1.75 - 2.00	$2.2 \pm 1.1 \pm 0.3$
2.00 - 2.25	$1.2 \pm 0.4 \pm 0.1$
2.25 - 2.50	$0.57 \pm 0.28 \pm 0.07$
2.50 - 2.75	$0.04 \pm 0.16 \pm 0.01$
2.75 - 3.00	$0.63 \pm 0.31 \pm 0.08$
3.00 - 3.25	$0.30 \pm 0.21 \pm 0.04$
3.25 - 3.50	$0.16 \pm 0.16 \pm 0.02$

Table 7.1: Cross section of reaction $\gamma\gamma \to \rho^0\phi$. The presented errors are statistical and systematical.

uncertainty come from

- incomplete description of the two-photon reaction, hidden in the form factors (1.5%)
- detector simulation (6%)
- trigger simulation (5%)
- determination of ARGUS integrated luminosity (1.8%)
- branching ratio Br($\phi \to 2K$) (1.6%) and
- unknown spin-parity structure of $\rho^0\phi$ production (around 9%, see below).

All contributions to the systematic error are calculated similarly as in chapter 6. The systematic error due to unknown spin-parity of $\rho^0\phi$, is calculated for each $W_{\gamma\gamma}$ bin separately. Using the Monte Carlo sample for the isotropic production of $\rho^0\phi$ at two-photon interaction, we determine the acceptance for various spin-parity k with relation

$$\eta_k = \frac{\sum_A |\Psi_k(x_A)|^2}{\sum_G |\Psi_k(x_G)|^2} \,. \tag{7.2}$$

Index A runs over all accepted events in a given $W_{\gamma\gamma}$ bin passing the $\rho^0\phi$ selection criteria while index G runs over all generated events in the same $W_{\gamma\gamma}$ bin. The angular distributions $\Psi_k(x)$ coincide with the distributions calculated for the $\omega\rho^0$ waves (Appendix A). Only the definition of polar angles x related to the ω meson changes. The angles θ_n

and ϕ_n define the direction of K^+ in the ϕ meson rest frame. Similarly as in chapter 6 the systematic error is then calculated as a standard deviation of a uniform distribution between two extreme acceptances η_k in each bin. The average over all $W_{\gamma\gamma}$ bins is 9%.

Chapter 8

Analysis of the reaction $\gamma\gamma \to \omega\phi \to \pi^+\pi^-\pi^0 K^+ K^-$

As previous two analyses also this one is based on a collected data sample of an integrated luminosity of 472.7 pb^{-1}. The $\omega\phi$ production is studied in the channel $\pi^+\pi^-\pi^0 K^+ K^-$ using the dominant decays of both vector mesons. Candidate events for the reaction $\gamma\gamma \to \pi^+\pi^-\pi^0 K^+ K^-$ are selected with almost the same criteria as in section 4.1.

- Two oppositly charged particles pointing to a common vertex have to be identified as pions $\lambda_\pi > 1\%$, and two as kaons $\lambda_K > 1\%$. Their probabilities for being electron P_e and muon P_μ have to be less than 10%. No other charged particle is allowed to originate from the common vertex.

- Neutral pion is identified as a photon pair with the invariant mass $m_{\gamma\gamma}$ lying at the pion nominal mass m_{π^0}. The allowed mass difference $|m_{\gamma\gamma} - m_{\pi^0}|$ is 75 MeV/c^2 for pairs with both photons identified by calorimeter showers, 50 MeV/c^2 for pairs with one converted photon, and 40 MeV/c^2 for pairs of converted photons.

- Beside photons from the π^0, unconnected showers are not allowed in the calorimeter unless they are recognized as noise or fake photons due to hadron interactions in the calorimeter.

- The total transverse momentum of selected particles $\pi^+\pi^-\pi^0 K^+ K^-$ has to be less than 100 MeV/c, while charged particles have to have the total transverse momentum of more than 20 MeV/c.

- The momentum conservation has to be fulfilled for all particles involved in the reaction, including undetected electron and positron (section 4.1).

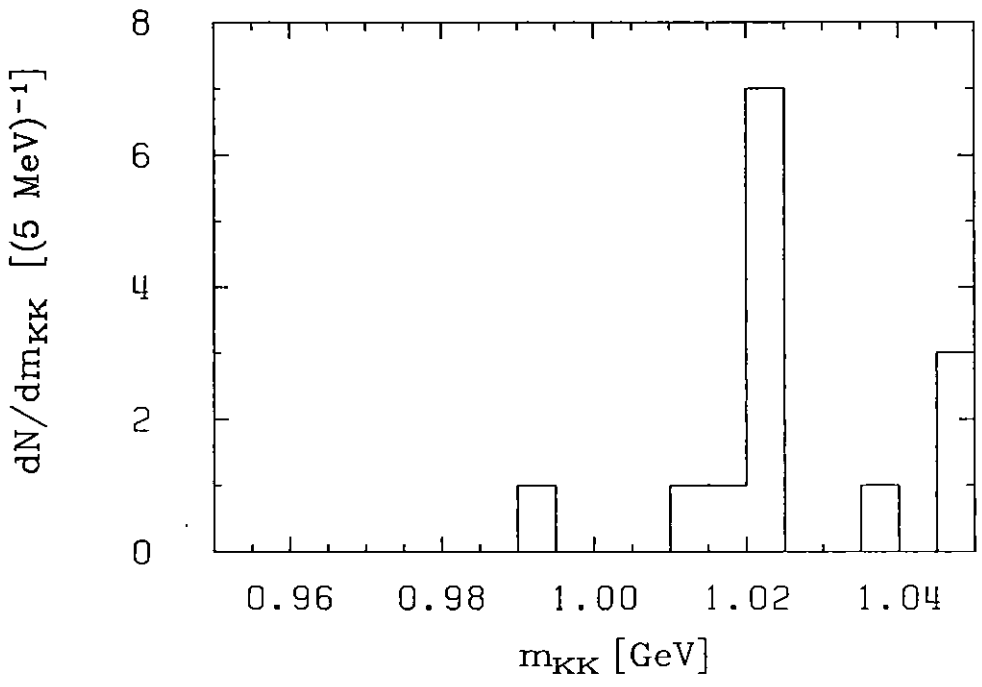

Figure 8.1: Invariant mass of K^+K^- pairs for selected $\pi^+\pi^-\pi^0 K^+K^-$ events.

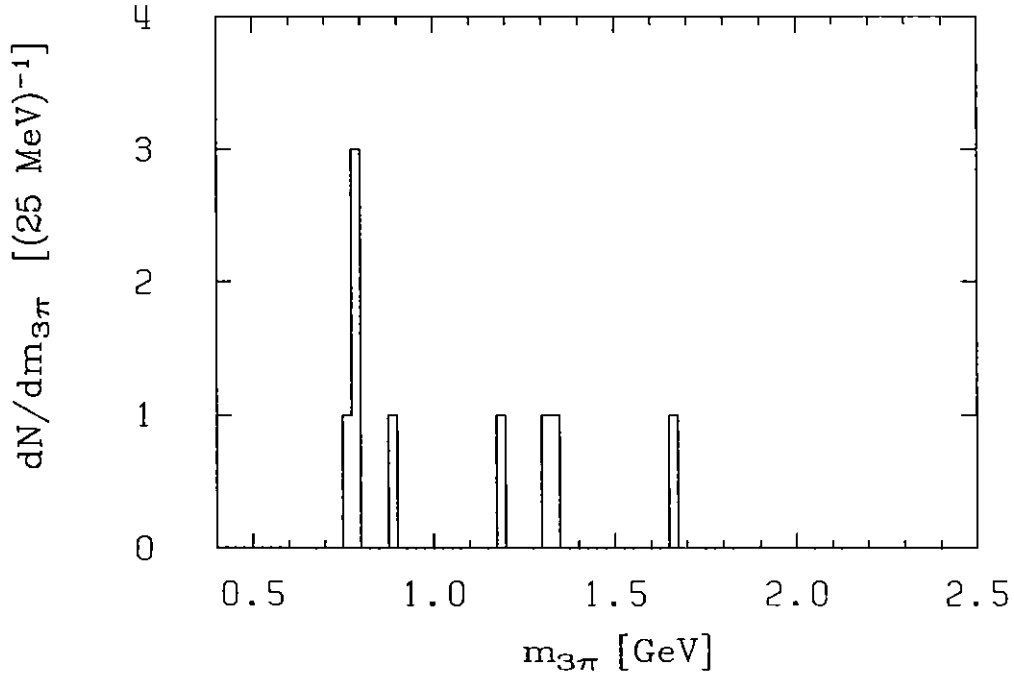

Figure 8.2: $\pi^+\pi^-\pi^0$ invariant mass for selected $\pi^+\pi^-\pi^0 K^+K^-$ events of which K^+K^- invariant mass differs for less than 12 MeV/c^2 from ϕ mass.

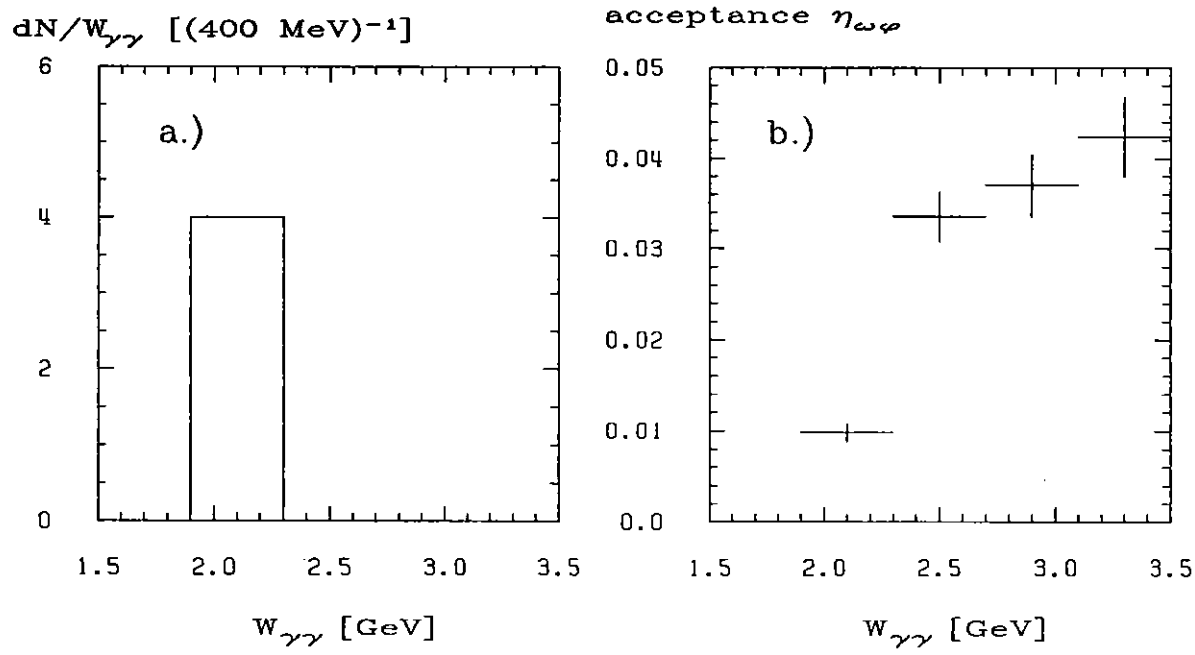

Figure 8.3: a.) Invariant mass of $\pi^+\pi^-\pi^0K^+K^-$ for all events that fulfil the $\omega\phi$ selection.
b.) The acceptance for this reaction obtained by simulation.

The distribution of K^+K^- invariant masses m_{KK} is plotted for the selected $\pi^+\pi^-\pi^0K^+K^-$ events in (fig. 8.1). At the mass of the vector meson ϕ an enhancement is seen. Keeping only the events whose K^+K^- invariant mass does not differ more than 12 MeV/c^2 from the mass of the ϕ meson, we obtain the spectrum of $\pi^+\pi^-\pi^0$ invariant masses shown in fig. 8.2. Of total 9 events 4 events lie in the mass region of ω, i.e. the difference between their $\pi^+\pi^-\pi^0$ invariant mass and ω nominal mass is less than 50 MeV/c^2, twice the detector resolution $\sigma(m_{3\pi})$ on three-pion invariant mass.

The resolution $\sigma(m_{3\pi})$ is obtained by making use of the simulated data sample of the reaction $\gamma\gamma \to \omega\phi \to \pi^+\pi^-\pi^0K^+K^-$. The scattering of the electron and positron is described in the simulation by the luminosity function (eq. 3.1) while the phase-space final state particles $\pi^+\pi^-\pi^0K^+K^-$ are weighted by the square of the decay matrix element $D_{\omega\phi}$ (eq. 1.61). The generation of the reaction $\gamma\gamma \to \omega\phi$ is followed by a detector and trigger simulation as described in chapter 3. The simulation is used also to calculate the acceptance for the reaction $\gamma\gamma \to \omega\phi$. Cuts on masses m_{KK} and $m_{3\pi}$ are also included in the acceptance calculation. The acceptance dependence on the two-photon invariant mass $W_{\gamma\gamma}$ is shown in fig. 8.3. It is averaged over bins of 250 MeV/c^2. Although the detector resolution on $\pi^+\pi^-\pi^0K^+K^-$ invariant mass is only 45 MeV/c^2, we chose this binning

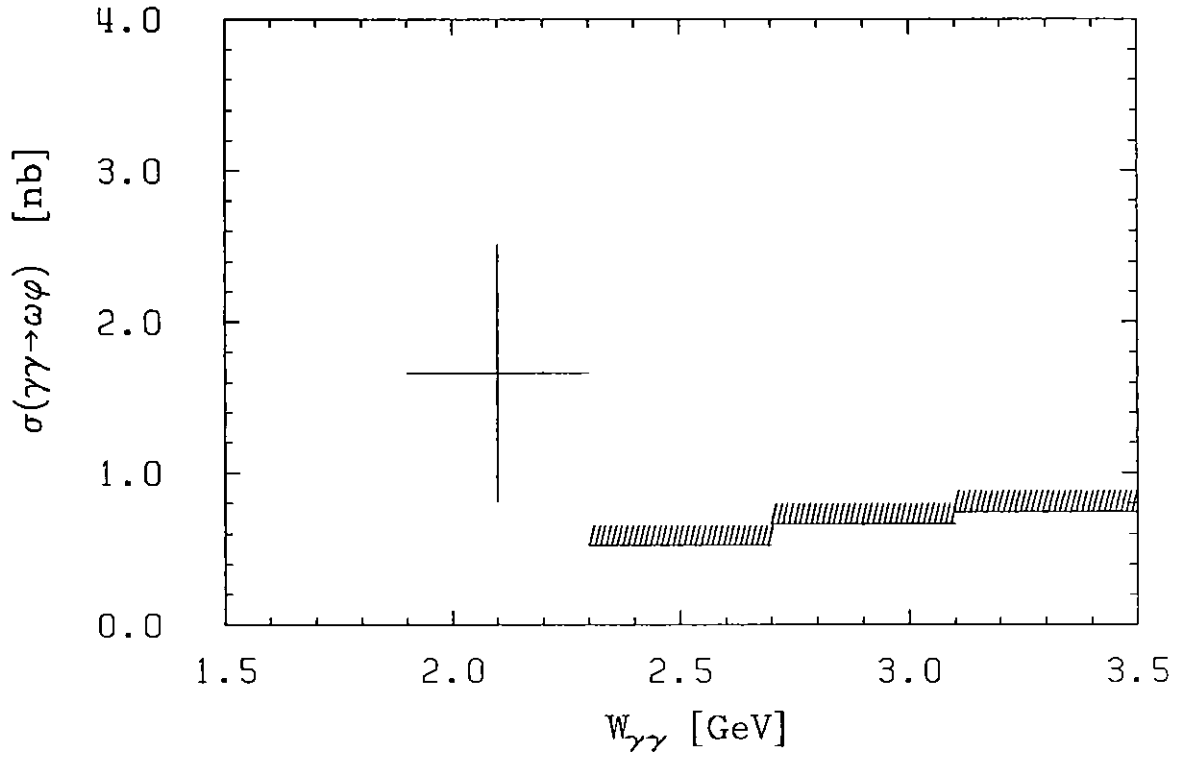

Figure 8.4: Cross section and upper limits at 95 % confidence level for the reaction $\gamma\gamma \to \omega\phi$.

due to the small number of $\omega\phi$ events (fig. 8.3). The contribution of background to the selected events is estimated by Monte Carlo simulation. Due to very severe cuts on the two-kaon and two-pion masses, the selection criteria reject all events from the simulated data sample of two-photon interactions, tau pair production $e^+e^- \to \tau\tau$ and reactions $e^+e^- \to$ hadrons (section 4.2). The number of events in this sample corresponds to the integrated luminosity of the measured data. Using fewer restrictive cuts on $\pi^+\pi^0\pi^-$ and K^+K^- masses, the reaction $\gamma\gamma \to \pi^+\pi^0\pi^- K^+K^-$ is found to have a dominant contribution to selected events. Therefore, we generate a large Monte Carlo sample of this reaction. Although the generated sample corresponds to five times the integrated luminosity of the measured data, no event has fulfiled the $\omega\phi$ selection criteria. So, an upper limit on background contribution is obtained to be 0.6 (95% confidence level). For

the $W_{\gamma\gamma}$ bin with all four events we calculate the cross section using the relation

$$\sigma_{\gamma\gamma\to\omega\phi} = \frac{N_i}{\eta_i L_{ee} L^i_{\gamma\gamma} \mathrm{Br}(\omega \to 3\pi) \cdot \mathrm{Br}(\phi \to 2K)} \quad , \tag{8.1}$$

N_i - number of selected events $\mathrm{Br}(\omega \to 3\pi)$ - decay fraction for decay $\omega \to \pi^+\pi^-\pi^0$
η_i - acceptance $\mathrm{Br}(\phi \to 2K)$ - decay fraction for decay $\phi \to K^+K^-$
$L^i_{\gamma\gamma}$ - average luminosity function in i-th $W_{\gamma\gamma}$ interval

The values used for decay fractions $\mathrm{Br}(\omega \to 3\pi)$ and $\mathrm{Br}(\phi \to 2K)$ can be found in [19]. The calculated cross section is plotted in fig. 8.4. Upper limits for the reaction $\gamma\gamma \to \omega\phi$ at 95 % confidence level are also shown.

Chapter 9

Summary

The five pion production in two-photon interactions was studied using the ARGUS experimental data. The analysis of this production includes contributions of reactions $\gamma\gamma \to \omega\rho^0$, $\gamma\gamma \to \omega\pi^+\pi^-$, $\gamma\gamma \to \rho^0\pi^+\pi^0\pi^-$, and $\gamma\gamma \to \pi^+\pi^+\pi^0\pi^-\pi^-$. The data analysis of these reactions was performed in the range of $W_{\gamma\gamma}$ energies between 1.1 GeV and 3.5 GeV. The cross sections were determined by using the maximum likelihood method. A sum of cross sections for both reactions with ω meson in the final state is compared with results of previous experiments (fig. 9.1). The obtained cross section is in agreement with previ-

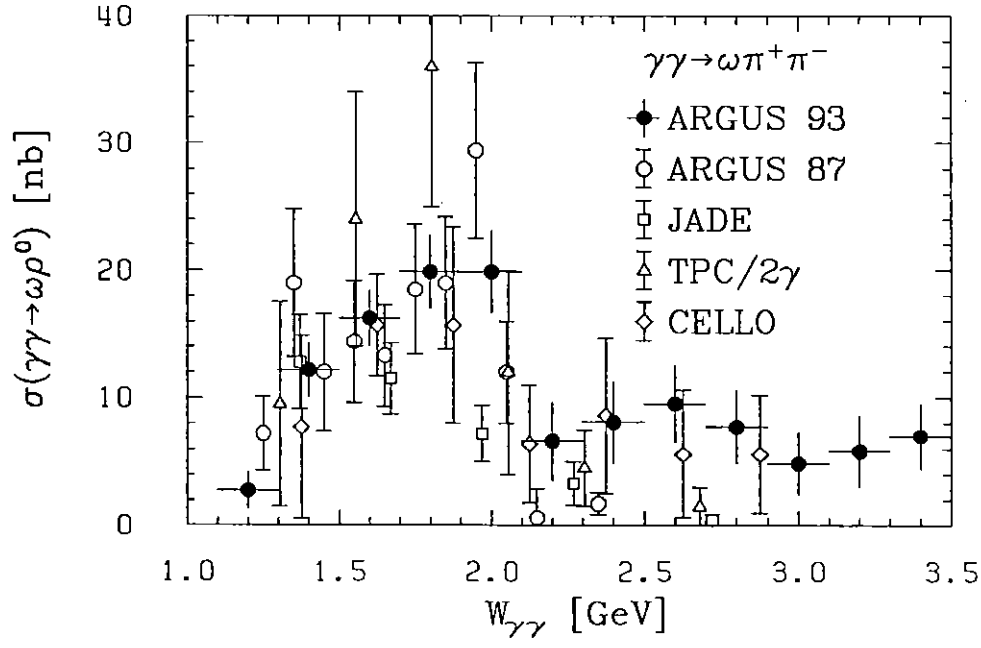

Figure 9.1: Comparison of the cross section for the reaction $\gamma\gamma \to \omega\pi^+\pi^-$ with results of previous experiments. Production of $\omega\pi^+\pi^-$ includes resonant and non resonant production of $\pi^+\pi^-$ pairs.

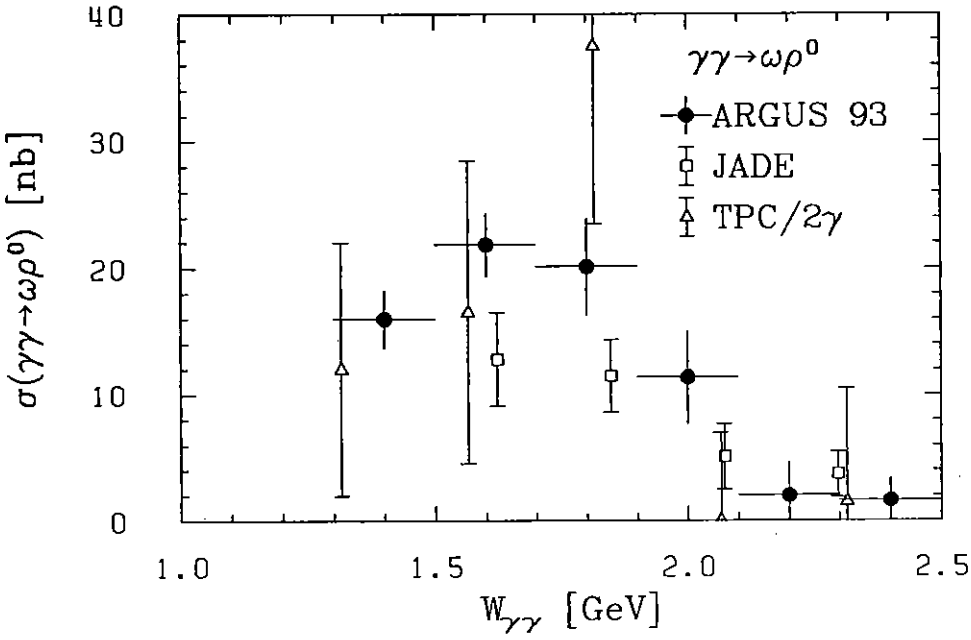

Figure 9.2: Cross sections for the reaction $\gamma\gamma \to \omega\rho^0$. The result of the 9 parameter fit is compared with cross sections of other experiments.

ous measurements of ARGUS [4] and CELLO results [48]. The cross section for reaction $\gamma\gamma \to \omega\rho^0$ is compatible with results of JADE [49] and TPC/2γ [50] (fig. 9.2). Also a spin-parity analysis of the $\omega\rho^0$ system was performed. Using the partial-wave method a dominance of the $(J^P, J_z) = (2^+, 2)$ wave is found in the region of $W_{\gamma\gamma}$ between 1.5 and 2.3 GeV.

Two-photon production of vector meson pair $\rho^0\phi$ has been studied in the reaction $\gamma\gamma \to \pi^+\pi^- K^+ K^-$ where both vector mesons are reconstructed by their dominant decays. The cross section for the reaction $\gamma\gamma \to \rho^0\phi$ has been measured for the first time. The measured cross section is consistent with ARGUS previous limit [5].

Two-photon production of $\omega\phi$ has also been found for the first time. A cross section of 1.65 ± 0.86 nb obtained for the $W_{\gamma\gamma}$ energy range between 1.9 and 2.3 GeV is consistent with the previous upper limit for this reaction [6]. For the region above 2.3 GeV an upper limit of 0.7 nb is obtained thus improving the upper limit set by ARGUS with the smaller data sample [6].

Appendix A

The Angular Wave Functions for $\omega\rho^0$

Using the relation (1.41)

$$\Psi^{L\ j}_{J^P\ J_z} = \sum_{m+M=J_z} \sum_{m_\omega+m_\rho=m} C^{J\ J_z}_{j\ m,\ L\ M}\ C^{j\ m}_{j_\omega\ m_\omega,\ j_\rho\ m_\rho}\ Y^M_L(\theta,\phi)\cdot|j_\omega,m_\omega\rangle\cdot|j_\rho,m_\rho\rangle$$

and expresions for $|j_\omega,m_\omega\rangle$ and $|j_\rho,m_\rho\rangle$ (equations (1.42), (1.45)), wave functions $\Psi^{L\ j}_{J^P\ J_z}$, describing the rotational properties of decay into vector mesons ω and ρ^0 are evaluated for all spin parity states with spin $J \leq 2$, that can be produced by interaction of two real photons:

$$\begin{aligned}\Psi_{0^+\ 0} &= Y^0_0(\theta,\phi)\cdot\left[\frac{1}{\sqrt{3}}|1,1\rangle\cdot|1,-1\rangle - \frac{1}{\sqrt{3}}|1,0\rangle\cdot|1,0\rangle + \frac{1}{\sqrt{3}}|1,-1\rangle\cdot|1,1\rangle\right] \\ &\propto \left[\cos\theta_n\cos\theta_\rho + \sin\theta_n\sin\theta_\rho\cos(\phi_n-\phi_\rho)\right] \qquad \text{(A.1)}\end{aligned}$$

$$\begin{aligned}\Psi_{0^-\ 0} &= \frac{1}{\sqrt{3}}Y^1_1(\theta,\phi)\cdot\left[\frac{1}{\sqrt{2}}|1,0\rangle\cdot|1,-1\rangle - \frac{1}{\sqrt{2}}|1,-1\rangle\cdot|1,0\rangle\right] \\ &\quad -\frac{1}{\sqrt{3}}Y^0_1(\theta,\phi)\cdot\left[\frac{1}{\sqrt{2}}|1,1\rangle\cdot|1,-1\rangle - \frac{1}{\sqrt{2}}|1,-1\rangle\cdot|1,1\rangle\right] \\ &\quad +\frac{1}{\sqrt{3}}Y^{-1}_1(\theta,\phi)\cdot\left[\frac{1}{\sqrt{2}}|1,1\rangle\cdot|1,0\rangle - \frac{1}{\sqrt{2}}|1,0\rangle\cdot|1,1\rangle\right] \\ &\propto \Big[\cos\theta\sin\theta_n\sin\theta_\rho\sin(\phi_n-\phi_\rho) + \sin\theta\sin\theta_n\cos\theta_\rho\sin(\phi-\phi_n) \\ &\qquad + \sin\theta\cos\theta_n\sin\theta_\rho\sin(\phi_\rho-\phi)\Big] \qquad \text{(A.2)}\end{aligned}$$

$$\begin{aligned}\Psi_{2^+\ \pm2} &= Y^0_0(\theta,\phi)\cdot|1,1\rangle\cdot|1,1\rangle \\ &\propto \sin\theta_n\sin\theta_\rho\cdot e^{\pm i(\phi_n+\phi_\rho))} \qquad \text{(A.3)}\end{aligned}$$

$$\begin{aligned}\Psi_{2+\ 0} &= Y_0^0(\theta,\phi)\cdot\left[\frac{1}{\sqrt{6}}|1,1\rangle\cdot|1,-1\rangle+\frac{\sqrt{2}}{\sqrt{3}}|1,0\rangle\cdot|1,0\rangle+\frac{1}{\sqrt{6}}|1,-1\rangle\cdot|1,1\rangle\right]\\ &\propto \left[2\cos\theta_n\cos\theta_\rho-\sin\theta_n\sin\theta_\rho\cos(\phi_n-\phi_\rho)\right] \qquad (A.4)\end{aligned}$$

$$\begin{aligned}\Psi_{2-\ 0}^{(S=1)} &= \frac{1}{\sqrt{6}}Y_1^1(\theta,\phi)\cdot\left[\frac{1}{\sqrt{2}}|1,0\rangle\cdot|1,-1\rangle-\frac{1}{\sqrt{2}}|1,-1\rangle\cdot|1,0\rangle\right]\\ &\quad+\frac{\sqrt{2}}{\sqrt{3}}Y_1^0(\theta,\phi)\cdot\left[\frac{1}{\sqrt{2}}|1,1\rangle\cdot|1,-1\rangle-\frac{1}{\sqrt{2}}|1,-1\rangle\cdot|1,1\rangle\right]\\ &\quad+\frac{1}{\sqrt{6}}Y_1^{-1}(\theta,\phi)\cdot\left[\frac{1}{\sqrt{2}}|1,1\rangle\cdot|1,0\rangle-\frac{1}{\sqrt{2}}|1,0\rangle\cdot|1,1\rangle\right]\\ &\propto \Big[2\cos\theta\sin\theta_n\sin\theta_\rho\sin(\phi_n-\phi_\rho)-\sin\theta\sin\theta_n\cos\theta_\rho\sin(\phi-\phi_n)\\ &\qquad+\sin\theta\cos\theta_n\sin\theta_\rho\sin(\phi-\phi_\rho)\Big] \qquad (A.5)\end{aligned}$$

$$\begin{aligned}\Psi_{2-\ 0}^{(S=2)} &= \frac{-1}{\sqrt{2}}Y_1^1(\theta,\phi)\cdot\left[\frac{1}{\sqrt{2}}|1,0\rangle\cdot|1,-1\rangle+\frac{1}{\sqrt{2}}|1,-1\rangle\cdot|1,0\rangle\right]\\ &\quad+\frac{1}{\sqrt{2}}Y_1^{-1}(\theta,\phi)\cdot\left[\frac{1}{\sqrt{2}}|1,1\rangle\cdot|1,0\rangle+\frac{1}{\sqrt{2}}|1,0\rangle\cdot|1,1\rangle\right]\\ &\propto \sin\theta\Big[\cos\theta_n\sin\theta_\rho\sin(\phi-\phi_\rho)+\sin\theta_n\cos\theta_\rho\sin(\phi-\phi_n)\Big] \qquad (A.6)\end{aligned}$$

The wave functions are calculated only for lowest orbital angular momentum $L = 0$ and $L = 1$, assuming that contribution of others can be neglected close to $\omega\rho^0$ threshold. A variable S in equations (A.5) and (A.6) marks vector sum of ω and ρ spins.

Bibliography

[1] TASSO Coll., R. Brandelik et al., *Phys. Lett.* **97B** (1980) 448.

[2] ARGUS Coll., H. Albrecht et al., *Z. Phys.* **C50** (1991) 1.

[3] N. N. Achasov et al., *Phys. Lett.* **108B** (1982) 134; *Z. Phys.* **C27** (1985) 99; *Phys. Lett.* **203B** (1988) 309.

[4] ARGUS Coll., H. Albrecht et al., *Phys. Lett.* **196B** (1987) 101.

[5] ARGUS Coll., H. Albrecht et al., *Phys. Lett.* **198B** (1987) 255.

[6] ARGUS Coll., H. Albrecht et al., *Phys. Lett.* **210B** (1988) 273.

[7] V. M. Budnev, I. F. Ginzburg, G. V. Meledin, V. G. Serbo, *Phys. Rep.* **15C** (1975) 181.

[8] C. N. Yang, *Phys. Rev.* **77** (1950) 242.

[9] G. Koepp, P. Zerwas and T. Walsh, *Nucl. Phys.* **B70** (1974) 461.

[10] M. Poppe, *Int. Jour. of Mod. Phys.* **A1** (1986) 545.

[11] J. J. Sakurai, *Ann. Phys.* **11** (1960) 1;
J. J. Sakurai and D. Schilknecht, *Phys. Lett.* **41B** (1972) 489.

[12] S. J. Brodsky and G. P. Lepage, *Phys. Rev.* **881** (1952) 1163.

[13] J. M. Blatt and V. Weiskopf, *'Theoretical Nuclear Physics'*, J. Wiley, New York, 1952.

[14] J.R. Taylor, *'Scattering Theory: The Quantum Theory on Nonrelativistic Collisions'*, J. Wiley, New York, 1972.

[15] M. Jacob, G. Wick, *Ann. Phys.* **7** (1959) 404.

[16] E.P. Wigner, *'Gruppentheorie und ihre Anwendung auf die Quantenmechanik der Atomspektren'*, Chapter XII, Edwards Bros., Ann Arbor, Michigan, 1954.

[17] B. de Wit, J. Smith, *'Field Theory in Particle Physics'*, North-Holland Physics Publishing, Amsterdam, 1986.

[18] H.M. Pilkuhn, *'Relativistic Particle Physics'*, Springer-Verlag, New York, 1979.

[19] Review of Particle Properties, Particle Data Group, *Phys. Lett.* **239 B** (1990) 1-516.

[20] Gourdin and Breach, *Phys. Rep.* **11C** (1974) 30.

[21] S. M. Flatte et al., *Phys. Rev.* **145** (1966) 1050.

[22] ARGUS Coll., H. Albrecht et al., *Nucl. Instr. and Meth.* **A275** (1989) 1.

[23] H.Nesemann et al., *DESY* **M-80-09** (1980);
K.Wille, *DESY* **M-81-047** (1981);
H.Nesemann and K.Wille, *IEEE Trans. Nucl. Sci.* **30** (1983) 1998.

[24] R.L.Childers and Y.Oku, *DESY* **F15-83-01** (1983);

[25] K.W.Edwards et al., *Nucl. Instr. and Meth.* **A252** (1986) 384.

[26] M.Danilov et al., *Nucl. Instr. and Meth.* **217** (1983) 153.

[27] R. Heller et al., *Nucl. Instr. and Meth.* **A235** (1985) 26.

[28] W. Hofmann et al., *Nucl. Instr. and Meth.* **163** (1979) 77;
W. Hofmann et al., *Nucl. Instr. and Meth.* **195** (1982) 475;
A. Drescher et al., *Nucl. Instr. and Meth.* **216** (1983) 35;
A. Drescher et al., *Nucl. Instr. and Meth.* **A249** (1986) 277.

[29] A. Drescher et al., *Nucl. Instr. and Meth.* **A237** (1985) 464.

[30] A. Arefiev et al., *Instr. Exp. Tech.* **29** (1986) 333.

[31] H. D. Schulz and H. J. Stuckenberg, Proc. Topical Conf. on the Application of Microprocessors in High Energy Physics Experiments, CERN, Geneva (1981) **CERN 81-07**, p.194.

[32] S. Weseler, Dissertation, Heidelberg University **IHEP-HD/86-2** (1986).

[33] V. Matveev, Argus Muon Analysis Program, Argus software note (1986);
B. Fominykh and V. Matveev, Argus Muon Program, Argus software note (1987);
B. Fominykh, Argus Muon Registration Efficiency, Argus software note (1988).

[34] H. Gennow, *DESY Internal Report* **F15-85-02** (August 1985).

[35] R. Brun et al., *CERN-DD/78/2* (1978).

[36] B. Rossi, *'High Energy Particles'*, Prentice-Hall, New York, 1952.

[37] R.L. Ford and W.R. Nelson, *'The EGS Code System'*, Version 3, *SLAC-210,* **UC-32** (1978).

[38] H. Fesefeldt, *RWTH Aachen Report PITHA 85/02,* (1985).

[39] K.W. McLean, *'$\pi^+\pi^-\gamma$ and K^+K^- Production in Two Photon Collisions at ARGUS'*, Ph.D. thesis, Mc Gill University, Montreal, Canada (1990).

[40] B. Hahn, Diplomarbeit, Dortmund University (1984).

[41] M. Pleško, M. Sc. Thesis, Ljubljana University (1985).

[42] S. Jadach and Z. Was, "KORALB version 2.1 - An upgrade with TAUOLA library of τ decays" *CERN-TH-5855/90* (1990).

[43] W.T. Eadie et al., *'Statistical Methods in Experimental Physics'*, North-Holland Physics Publishing, Amsterdam, 1971.

[44] CERN Program Library, Genlib *'Function Minimization and Error Analysis* - **MINUIT'**.

[45] TASSO Coll., M. Althoff et al., *Z. Phys.* **C16** (1982) 13.

[46] B. Boštjanšič, *'Production of four pions in photon-photon reactions '*, Doctor thesis, University of Ljubljana , Ljubljana, Slovenia, (1990).

[47] ARGUS Coll., H. Albrecht et al., *Phys. Lett.* **198B** (1987) 577.

[48] CELLO Coll., H. J. Behrend et al., *Phys. Lett.* **257B** (1991) 505.

[49] JADE Coll., A. Wegner et al., *Z. Phys.* **C48** (1990) 393.

[50] K. A. Derby, PhD. Thesis, preprint LBL-23548.